ABSTRACT

Title of dissertation: SEARCH FOR FIRST GENERATION SCALAR LEPTOQUARKS WITH THE CMS EXPERIMENT AT THE LARGE HADRON COLLIDER

Elizabeth Twedt, Doctor of Philosophy, 2011

Dissertation directed by: Professor Andrew Baden
Department of Physics

Leptoquarks are particles predicated to exist by many models beyond the standard model. A search is presented for the production of first generation scalar leptoquarks with a branching ratio into charged leptons of $\beta = 1$ with the Compact Muon Solenoid detector at the Large Hadron Collider at CERN, at a center of mass energy of $\sqrt{s} = 7$ TeV.

SEARCH FOR FIRST GENERATION SCALAR LEPTOQUARKS WITH THE CMS EXPERIMENT AT THE LARGE HADRON COLLIDER

by

Elizabeth Twedt

Dissertation submitted to the Faculty of the Graduate School of the
University of Maryland, College Park in partial fulfillment
of the requirements for the degree of
Doctor of Philosophy
2011

Advisory Committee:
Professor Andrew Baden
Professor Zackaria Chacko
Professor Sarah Eno
Professor. Carter Hall
Professor Alice Mignerey

Acknowledgments

This analysis has been performed in conjunction with Dr. Paolo Rumerio, Dr. Francesco Santanastasio and Mr. Dinko Ferencek. All three never fail to astound me with their intelligence, immense dedication and hard work, and their tireless curiosity. Sarah Eno directed us in this analysis. Her wealth of experience and perspective helped us maintain our focus and overcome multiple challenges.

My advisor, Drew Baden, has been my tireless supporter and shown great patients and guidance over the past several years as he has attempted to mold me into a particle physicist. I especially appreciate his encouragement and effort to make this document the best it could be.

The time I spent at CERN challenged me in ways I would never have anticipated. I am grateful to all those in Meyrin, Prevessin and Cessy who helped me grow, both professionally and personally. I owe a large part of my education during that time to Dr. Richard Kellogg. He is generously dedicated to the formation of the new generation of physicists, and to making CMS a success.

I consider myself exceptionally lucky to be surrounded by a research group that is stimulating and committed to the work we do. I am especially grateful to Dr. Jeff Temple for his extensive revisions of this document.

The support I have received from close friends and family has sustained me over the last five years. Naturally, I owe a debt of gratitude to my parents, Donna and Tom Lockner, for their encouragement, and to my husband, Kevin, for his support and ever-present smile.

Table of Contents

List of Tables

List of Figures

List of Abbreviations

SM	standard model
σ	cross section
LQ	leptoquark
λ	Yukawa coupling
β	branching fraction
LHC	Large Hadron Collider
CERN	European Center for Nuclear Research
c	speed of light (3×10^8 m/s)
PSB	Proton Synchrotron Booster
PS	Proton Synchrotron
SPS	Super Proton Synchrotron
RF	Radio Frequency
CMS	Compact Muon Solenoid
BSC	Beam Scintillator Counters
BPTX	Button Beam Pickup
ECAL	Electromagnetic Calorimeter
HCAL	Hadronic Calorimeter
DT	Drift Tube
CSC	Cathode Strip Chamber
RPC	Resistive Plate Chamber
ZDC	Zero Degree Calorimeter
CASTOR	Centauro And Strange Object Research
L1	Level 1 Trigger
HLT	High Level Trigger
DAQ	Data Acquisition System
ISR	Initial State Radiation
FSR	Final State Radiation
ΔR	$\sqrt{\Delta\phi^2 + \Delta\eta^2}$
EMF	Electromagnetic Fraction
E_T	Transverse Energy
p_T	Transverse Momentum
PD	Primary Data set
IRC	Infrared and colinear

Chapter 1

Introduction and Theory

Theories predicting the existence of new particles have often been proposed as solutions to fundamental mysteries concerning our understanding of the structure of Nature. With the idea of antimatter, for example, Dirac predicted the existence of the positron before it was discovered in 1932 in order to explain the negative energy solutions to the relativistic wave equation [1]. Similarly, the theory of Supersymmetry proposes an additional partner particle for each particle we currently observe in nature in order for the large mass predictions of the hypothesized Higgs Boson to be most natural [2].

Another example of historical note was the problem of the apparent non-conservation of energy and momentum in nuclear beta decay. In 1914 Chadwick observed that decaying nuclei emit high energy electrons with a continuous spectrum of energies. If one assumes a two body final state ($n \rightarrow p + e^-$) this leads to the conclusion that neither energy nor linear momentum is conserved [3]. To rescue the laws of mechanics Pauli proposed a neutral particle with negligible rest mass, the"neutrino", that is emitted simultaneously but not detected due to its small probability to interact with matter.

This proposal spurred Fermi to formulate his theory of beta decay, which in turn helped pave the path for the development of a framework unifying the

electromagnetic and weak interactions. Eventually this framework was extended to include the strong force, and by the late 1970s the complete theory came to be known as the Standard Model (SM).

Astoundingly complete in its modern form, there are still many unanswered questions that plague the SM. There are countless theories of extensions and additions that go beyond the SM, each with merits and complications. A modern mystery of particle physics that lends itself to a similar resolution as that proposed by Pauli's neutrino is the equality in number of fundamental particles that feel only the electroweak force (leptons) and those that also feel the strong force (quarks). New particles possessing qualities of both would provide an elegant motivation for this symmetry, and are not prohibited by the current formulation of the SM. The proposed particles, "leptoquarks", may have escaped detection thus far due to a large rest mass and thus a small (potentially zero) probability to be produced in collisions at modern particle colliders.

The arrival of the data era at the Large Hadron Collider in Geneva, Switzerland offers an opportunity to dispel or confirm a number of these proposed theories by shining a light brighter than any before it on some of Nature's secrets.

1.1 Overview of the Standard Model

1.1.1 Historical Overview

The SM is a mathematical model that attempts to describe the interaction of all known fundamental particles and forces. The theory of what today is referred

to as the SM began in the early 1960s when physicists first successfully unified the electromagnetic and weak interactions into one mathematical framework.

A generalization of a gauge invariant field theory for multiple fields was first proposed in 1954 by Yang and Mills [4]. Their motivation was to find a model for the proton and neutron, but their model proved ill suited for this. With the discovery of the neutrino as an addition to the electron in the electroweak sector their model was revived.

In 1961 Glashow first proposed a structure of the weak force involving both neutral and charged currents. Over the following two decades physicists such as Weinberg, Salam and 't Hooft, among others, reformulated and adapted the model to achieve a framework that is mathematically viable and an accurate description of the interaction of particles through the electroweak force.

The quark model was proposed in 1964 by Gell-Mann and Zweig independently. Prior to 1964 a number of strongly interacting particles had been observed and placed into patterns based on quantum numbers such as charge, flavor and spin. The quark model proposed that these strongly interacting particles, hadrons, are composed of yet smaller particles, quarks, that exist in three color states [5]. The experimental evidence validating this theory came from deep inelastic scattering experiments conducted at the Stanford Linear Accelerator Complex in conjunction with the Massachusetts Institute of Technology [6], the results of which led to the award of the 1990 Nobel Prize in Physics to Friedman, Kendall and Taylor [7]. High energy electrons were scattered off protons and neutrons, revealing an inner structure of quarks held together by gluons. Ultimately the model of quarks was expanded

to the theory of Quantum Chromodynamics and combined with the electroweak theory to produce a model encompassing the three forces primarily responsible for the interaction of subatomic particles.

1.1.2 Particle Classification

The particles of the SM can be classified into two groups based on their spin quantum number. Particles with integer spin, bosons, are the force carriers, responsible for the interaction of the particles through the fundamental forces. Particles with half integer spin, fermions, constitute the vast majority of stable matter. All SM fermions fall into two categories: quarks, which feel both the electroweak and strong force, and leptons, which feel only the electroweak force. The observed particles of the SM are shown in Table 1.1. Stable matter in Nature is composed mostly of particles found in the first generation of quarks and leptons.

Interactions between fermions are mediated by the vector (spin 1) bosons, which are the quanta of the fields of the fundamental forces. No fundamental scalar (spin 0) or spin 2 particles have been observed in Nature at this time. The addition to the SM of the theoretical Higgs field results in one scalar boson, the Higgs boson, which has yet to be observed experimentally. The Higgs field would help elucidate the origin of mass and is commonly accepted as a component of the SM.

Quarks carry both electric charge and color (the charge for the strong force), and are organized into three generations of increasing mass, each generation a doublet of quarks. All stable observed combinations of quarks are color neutral, com-

posed of either a quark and antiquark (meson) with the same color and anticolor, or one red quark, one green quark and one blue quark (baryon) that add chromatically to neutral.

The force mediators of the strong force, the gluons, themselves have color and interact with each other, contributing more energy to the field as the distance of interaction increases. As the distance between the quarks approaches zero the field energy decreases and the quarks become asymptotically free. The proposal of this property of asymptotic freedom resulted in the 2004 Nobel Prize, awarded to Gross, Politzer and Wilczek [8]. Asymptotic freedom explains the confinement of quarks, the fact that isolated quarks have not been observed. It is energetically advantageous to create a quark and antiquark pair from the vacuum rather than to have isolated quarks interact over long distances.

The six leptons are again arranged into three generations of doublets, each doublet with its own flavor quantum number. Each doublet contains a charged lepton and a neutral lepton (neutrino) of the same flavor. The charged leptons exist in states such that their spin may be aligned or anti-aligned with their momentum, left or right-handed helicity. Neutrinos, however, have been observed only in states with their spin anti-aligned to their momentum, states of left-handed helicity respectively. The discovery that neutrinos have mass [9] implies that the SM neutrino is a mixture of left and right-handed states. The mixing amplitude between the two states is on the order of m_ν/E, where m_ν is the mass of the neutrino, and E is the energy of the particle. Nearly all neutrinos detected in experiments are ultra-relativistic, leading to undetectably small mixing from the right handed helicity states.

1.1.3 Cross Section and Event Rate

The quantum nature of particle interactions implies each process has a quantum mechanical amplitude related to the probability that it will occur. This depends on the strength of the forces involved in the interaction, the momenta and masses of the particles involved, and the quantum numbers of the initial and final state particles. The mean number of interactions of a specific type is related to the current density of the incident beam through the cross section, σ, measured in units of barns (1 barn = 10^{-24} cm^2).

Cross section is defined as the ratio of R, the rate at which a particular process occurs, to the instantaneous luminosity $\mathcal{L}$, the number of protons per unit cross sectional area of the beam per second, as shown in Eq. 1.1.

$$\sigma = \frac{R}{\mathcal{L}} \tag{1.1}$$

Rearranging Eq. 1.1 and integrating both sides over time gives the total number of events from a particular process, N, as a function of the integrated luminosity, L_{int}, and the cross section for that process, as shown in Eq. 1.2.

$$N = L_{int} \times \sigma \tag{1.2}$$

The cross sections for various SM interactions differ greatly from one another. Figure 1.1 shows the theoretical cross section for various processes (SM and beyond) for proton-proton collisions at a center of mass energy of 14 TeV. Note that the Large Hadron Collider will produce collisions at a center of mass energy of 7 TeV.

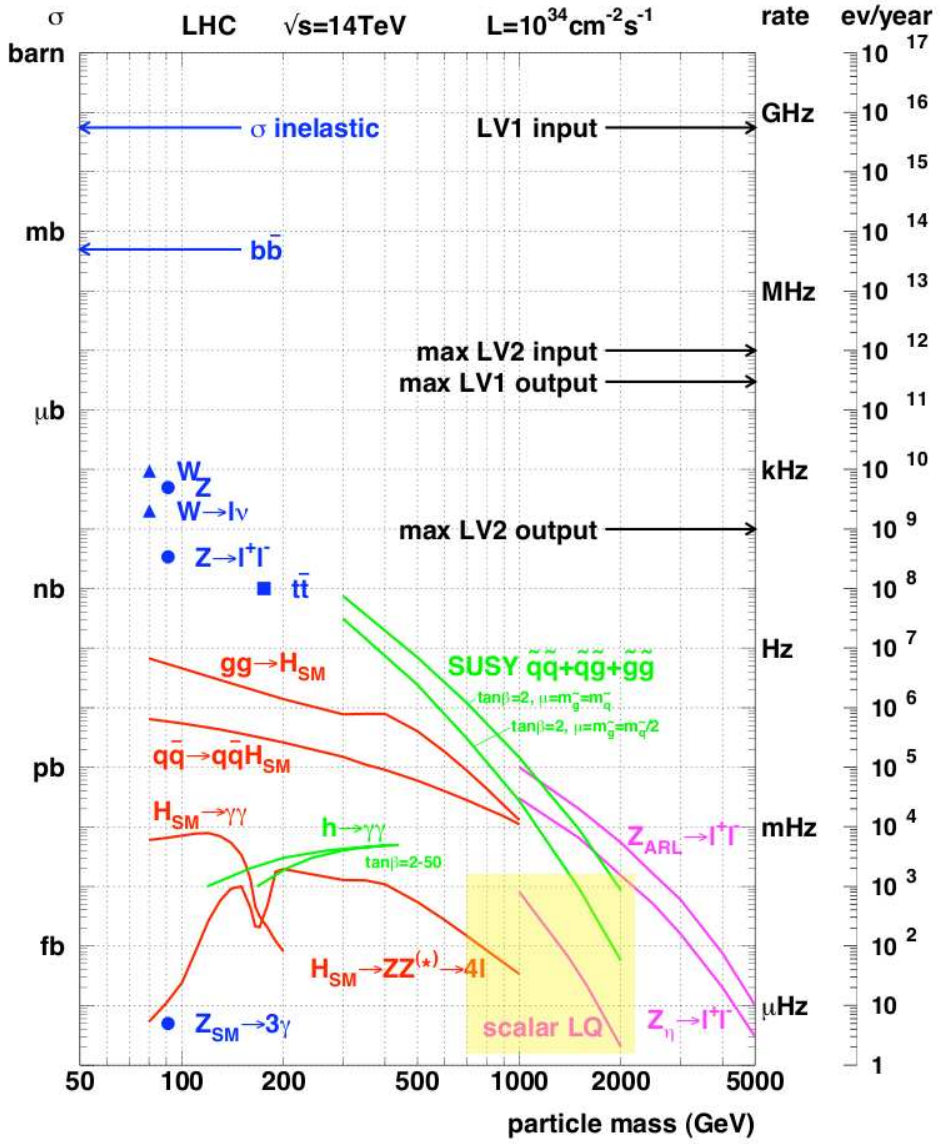

Figure 1.1: Production cross section (left axis) and yearly event rate (right axis) for SM processes and commonly studied processes beyond the SM for proton-proton collisions at a center of mass energy of 14 TeV with an instantaneous luminosity of 10^{34} cm^{-2}s^{-1}.

Quarks				Leptons		
Flavor	Charge	Spin		Flavor	Charge	Spin
u	$+1/3$	$1/2$		e	-1	$1/2$
d	$-2/3$	$1/2$		ν_e	0	$1/2$
c	$+1/3$	$1/2$		μ	-1	$1/2$
s	$-2/3$	$1/2$		ν_μ	0	$1/2$
t	$+1/3$	$1/2$		τ	-1	$1/2$
b	$-2/3$	$1/2$		ν_τ	0	$1/2$

Bosons			
Particle	Charge	Spin	Force
γ	0	1	Electroweak
W^+	$+1$	1	Electroweak
W^-	-1	1	Electroweak
Z^0	0	1	Electroweak
g	0	1	Strong

Table 1.1: Observed particles in the standard model

1.2 Theoretical Formalism

1.2.1 Euler-Lagrange Formulation

The SM is built on the interactions of the fermions with the fundamental forces through the vector bosons. An analogous model describing the interaction of particles in classical mechanics comes from the Euler-Lagrange approach shown in Eq. 1.3, where T is the kinetic energy, U the potential energy, and q_i any spatial coordinate.

$$\frac{d}{dt}(\frac{\partial L}{\partial \dot{q}_i}) = \frac{\partial L}{\partial q_i} \tag{1.3}$$

It is possible to formulate a Lagrangian density for fields as a function of their space and time coordinates, x_μ by extending the Euler-Lagrange formalism from classical mechanics. The Dirac Lagrangian for a free, spin 1/2 field is shown in Equation 1.4, where ψ is the wave function operator of the particle with mass m, and γ^μ are the gamma matrices defined in Appendix A. This Lagrangian, by construction, satisfies Eq. 1.3.

$$\mathbf{L} = i(\hbar c)\bar{\psi}\gamma^\mu\partial_\mu\psi - (mc^2)\bar{\psi}\psi \tag{1.4}$$

If the field, ψ, is modified by a global phase factor, $e^{i\theta}$, we expect the physics to remain unchanged, as one could simply redefine globally the point of "zero" phase. Clearly, Eq. 1.4 does remain unchanged under the transformation $\psi \rightarrow e^{i\theta}\psi$.

If the phase of the transformation is a function of space-like coordinates, $\psi \rightarrow e^{i\theta(x)}\psi$ (local gauge transformation), an extra term in the Lagrangian appears as

a result of the derivative. It can be modified to be invariant under local gauge transformations by the addition of a vector field, A_μ and the substitution shown in Eq. 1.5.

$$\partial_\mu \rightarrow D_\mu = \partial_\mu + i\frac{q}{\hbar c}A_\mu \tag{1.5}$$

The new Lagrangian is invariant under local gauge transformation only if A_μ is constrained to transform according to Eq. 1.6, and is massless (Appendix A).

$$A_\mu \rightarrow A_\mu - \frac{\hbar c}{q}\partial_\mu \theta \tag{1.6}$$

The new Lagrangian for this gauge invariant, spin 1/2 field is shown in Equation 1.7, where $F^{\mu\nu} = \partial^\mu A^\nu - \partial^\nu A^\mu$.

$$\mathbf{L} = [i\hbar c\bar{\psi}\gamma^\mu\partial_\mu\psi - mc^2\bar{\psi}\psi] + [\frac{-1}{16\pi}F^{\mu\nu}F_{\mu\nu}] - [(q\bar{\psi}\gamma^\mu\psi)A_\mu] \tag{1.7}$$

This may be recognized as the Lagrangian for electrodynamics, the interaction of point charges with the massless photon constrained by Maxwell's Equations [10]. The condition on the transformation of A_μ shown in Eq. 1.6 does not effect the electric or the magnetic field, and so is an allowed constraint on the potential. This model, then, is built from the symmetry of the Lagrangian under transformations of fields of the form $e^{i\theta(x)}$, one representation of which is the group of 1x1 Unitary matricies, or U(1).

A consequence of the invariance of this Lagrangian under a global gauge variation of the electromagnetic field is the conservation of electric charge. The correla-

tion between conserved quantities and differentiable symmetries in Nature was first proven by Noether in 1917 [11]. Noether concluded that for any differentiable symmetry of the action there exists a conserved quantity of the system. Based on the observed conservation of any quantity in the interaction of fundamental particles, in this case the charge of the fermion, a Lagrangian can be constructed in accordance with Noether's theorem.

1.2.2 Electroweak Field

Interactions between charged leptons and neutrinos led physicists to propose a model in which the leptons are organized into doublets, two-dimensional vectors of two single complex fields. In this model, ψ is a doublet representing the wave function of the lepton. Local gauge transformations may now be expressed as SU(2) transformations of the form in Eq. 1.8,

$$\psi \rightarrow \psi' = e^{i\vec{\epsilon}\cdot\vec{t}}\psi \tag{1.8}$$

where $\vec{\epsilon}$ is a vector of three real parameters depending on x_μ, and $\vec{t}$ is a vector of the Pauli matrices defined in Appendix A.1.

It is possible to create a Lagrangian for ψ which is invariant under such local gauge transformations by defining a triplet of gauge fields, A^1_μ, A^2_μ, and A^3_μ, one for each matrix t_i, and requiring that the derivative transform as shown in Eq. 1.9,

$$\partial_\mu \rightarrow D_\mu = \partial_\mu + igA_\mu \cdot \vec{t} \tag{1.9}$$

where g is a free parameter[1]. The three fields A_μ are required to transform as in

[1]Using the notation presented in [3].

Eq. 1.10 to maintain local gauge invariance.

$$\vec{A_\mu} \cdot \vec{t} \rightarrow \vec{A'_\mu} \cdot \vec{t} = e^{i\vec{\epsilon}\cdot\vec{t}}(A_\mu \cdot \vec{t} - \frac{\vec{i}}{g}\partial_\mu)e^{-i\vec{\epsilon}\cdot\vec{t}} \tag{1.10}$$

The resulting gauge invariant Lagrangian contains terms for vector bosons that one might initially assume to be the mediators of the weak interaction, the $W^\pm$ and Z^0 bosons. The boson field terms in this Lagrangian, however, are massless, whereas the weak bosons in Nature are seen to be massive.

A gauge invariant field theory with massive bosons can be formulated by introducing a new field, ϕ, where the potential of the field is symmetric about $\phi = 0$, but the minimum value of the potential (the ground state) is not at zero. This is known as spontaneous symmetry breaking: the non-vanishing value of the potential in the ground state chooses a preferred combination of quantum numbers and breaks the $SU(2)$ symmetry. For example, the potential in the Lagrangian in Eq. 1.11 is symmetric with respect to ϕ about $\phi = 0$, but has a minimum at $\phi^\dagger\phi = -\mu/2\lambda$.

$$\mathbf{L} = (\partial_\mu\phi^\dagger)(\partial^\mu\phi) - \mu^2\phi^\dagger\phi - \lambda(\phi^\dagger\phi)^2 \tag{1.11}$$

This Lagrangian alone is not invariant under local gauge transformations. As done previously, the transformation of the derivative may be defined in a way to make the Lagrangian invariant, shown in Eq. 1.12,

$$\partial_\mu\phi \rightarrow D_\mu\phi = \partial\phi + ig\vec{A_\mu} \cdot \vec{t}\phi + 1/2ig'B_\mu\phi \tag{1.12}$$

where g and g' are independent coupling strengths of the fields, $\vec{A_\mu}$ is a triplet of gauge fields, and B_μ is a singlet gauge field.

The choice to add B_μ to the Lagrangian at this point is not necessary to achieve local gauge invariance, but becomes useful to help generate the left-right handed structure of the weak interactions, and to incorporate the electromagnetic interaction into the symmetry. The charged vector bosons are observed to interact only with left handed fields, while the neutral vector bosons interact with both the left and right handed fields. To account for this, the $\vec{A}_\mu$ fields are assumed to interact only with left handed fields, and the Lagrangian of these fields is required to be invariant under $\mathrm{SU}(2)_L$ transformations. The single B_μ field interacts with both left and right handed fields and the Lagrangian is required to be invariant under U(1) transformations since the components of the doublet are not interchanged in these interactions. The conserved quantum number associated with the B_μ field was suggested in 1961 by Glashow in the form of a 'weak hypercharge' current, Y, a linear combination of electromagnetic charge and isospin [12]. This connects the electromagnetic interaction with the weak interaction through the underlying symmetry group $SU(2)_L \times U(1)_Y$.

To understand the physics of the new Lagrangian it is useful to write it in terms of small perturbations $\sigma(x_\mu)/\sqrt{2}$ about the ground state (where the $\sqrt{2}$ is chosen for convenience later in the calculation of the Lagrangian). The new covariant derivative takes the form shown in Eq. 1.13,

$$\begin{aligned} D_\mu\phi^\dagger D^\mu\phi &= 1/2\partial_\mu\sigma(x_\mu)\partial^\mu\sigma(x_\mu) \\ &\quad +[1/4g^2(A_{\mu 1}A_1^\mu + A_{\mu 2}A_2^\mu) \\ &\quad +1/4g^2(A_{\mu 3} - (g'/g)B_\mu)^2](\eta + \sigma(x_\mu)/\sqrt{2})^2 \end{aligned} \tag{1.13}$$

where higher order terms in $\sigma(x_\mu)$ are neglected.

If this Lagrangian is to describe the weak interaction there will have to be two quantized fields of definite charge, the W^+ and W^- bosons. These are made from linear combinations of the A_μ fields, as in Eq. 1.14.

$$\begin{aligned} W_\mu^+ &= \frac{1}{\sqrt{2}}(A_{\mu 1} - iA_{\mu 2}) \\ W_\mu^- &= \frac{1}{\sqrt{2}}(A_{\mu 1} + iA_{\mu 2}) \end{aligned} \tag{1.14}$$

The B_μ and the $A_{\mu 3}$ are combined as in Eq. 1.15 to make the two neutral vector bosons, the Z^0 and the photon.

$$\begin{aligned} Z_\mu &= cos\theta_W A_{\mu 3} - sin\theta_W B_\mu \\ A_\mu &= sin\theta_W A_{\mu 3} + cos\theta_W B_\mu \end{aligned} \tag{1.15}$$

The angle θ_W, the Weinberg angle, is an adjustable parameter of the model relating the two previously independent coupling strengths, g' and g.

The full Lagrangian then contains, among other terms, two massive charged vector field terms associated with the W^+ and W^- bosons, a massive neutral vector field term associated with the Z^0 boson, and a massless vector field term associated with the photon, all of which have been experimentally observed. It also contains a massless scalar field term, σ, referred to as the Higgs field, which has not yet been observed in Nature.

1.2.3 Quantum Choromodynamics

Just as the single field was expanded to a two-dimensional doublet for charged and neutral leptons, so can it be expanded to a three-dimensional vector of single

colored fields to accommodate the quarks. This Lagrangian must be invariant under transformations that can be expressed as rotations by elements of the SU(3) group, as the physics of the interaction is expected to be the same for all colors. The cost of this is the introduction of eight gauge fields which can be interpreted as the eight uniquely colored gluons mediating the strong force.

The quarks, being electrically charged, also interact via the electroweak force. The electroweak couplings between quarks within the same generation are largest, although intergenerational charged current interactions are observed. In 1963 Cabibbo suggested that the coupling between quarks within the first generation via the weak force carries a factor of $cos\theta_c$, while the coupling between first and second generation quarks carries a factor of $sin\theta_c$, where θ_c (the "Cabibo angle") is determined empirically to be small. One interpretation of this is that, while the quarks are eigenstates of the SU(3) strong symmetry, they do not correspond to eigenstates of the electroweak force.

Kobayashi and Maskawa were able to expand the 2-dimensional Cabibbo mixing matrix to include interactions between all three generations of quarks [13]. The matrix elements can be parameterized with three generalized Cabibbo-like angles, θ_1, θ_2, and θ_3, and one unique phase, δ, as is shown in Eq. 1.16, where c_i is $cos\theta_i$, s_i is $sin\theta_i$, d, s and b are the down, strange and bottom strong eigenstates respectively,

and d', s' and b' correspond to the weak eigenstates.

$$\begin{pmatrix} d' \\ s' \\ b' \end{pmatrix} = \begin{pmatrix} c_1 & s_1 c_3 & s_1 s_3 \\ -s_1 c_2 & c_1 c_2 c_3 - s_2 s_3 e^{i\delta} & c_1 c_2 s_3 + s_2 c_3 e^{i\delta} \\ -s_1 s_2 & c_2 s_2 c_3 + c_2 s_3 e^{i\delta} & c_1 s_2 s_3 - c_2 c_3 e^{i\delta} \end{pmatrix} \begin{pmatrix} d \\ s \\ b \end{pmatrix} \tag{1.16}$$

No interactions between quarks with the same electric charge in different generations has been observed. This type of interaction is forbidden by the Glashow-Iliopoulus-Maiani (GIM) mechanism [14], a model of weak interactions that is largely credited with the predicted existence of the charm quark.

1.2.4 Summary

The complete Lagrangian for the SM can then be expressed as the combination of three separate Lagrangians: one that describes fields invariant under transformations by elements of the $\mathrm{U}(1)_Y$ group (weak hypercharge), a second of left handed doublets that satisfies invariance under transformations by elements of the $\mathrm{SU}(2)_L$ group (weak isospin), and a third of three-vector colored fields that satisfies invariance under transformations by elements of the SU(3) group (strong interactions). The total underlying symmetry of the SM can be expressed as:

$$SU(3)_c \times SU(2)_L \times U(1)_Y \tag{1.17}$$

1.3 Leptoquarks

The symmetry between the generations of leptons and quarks have led to many theories in which they are interrelated [19]. In grand unified theories (GUTs) the leptons and quarks are embedded in a larger underlying symmetry, for example the E(6) model of Pati and Salam [16]. Technicolor offers an alternative to the Higgs mechanism to explain boson mass by introducing new gauge fields that are manifest only at higher energies, opening the door for new massive bosons coupling to both the quarks and leptons. Compositeness theories postulate either quarks, leptons or both are composed of yet undiscovered particles that combine to form stable states.

A certain class of theories addressing the symmetry between the generations of leptons and quarks contain particles named "leptoquarks" that carry lepton and baryon number simultaneously. The leptoquarks (LQ) would then be free to decay to a lepton and a quark. The models share at least 4 important parameters: the Yukawa coupling, λ, at the lepton-quark-LQ vertex; the branching fraction, β, into a charged lepton and quark (compared to the decay to a neutrino and quark); the mass of the LQ; and the spin. In this analysis only scalar (spin 0) LQs with a β of 1 are considered.

The production cross section for LQs of masses within reach of the LHC experiments is dominated by pair production, as shown in Fig. 1.2 for a center of mass energy of 14 TeV. The cross sections for pair and single LQ production become similar at a LQ mass closer to 700 GeV at a center of mass energy of 7 TeV, where, for convenience, a system of units is adopted such that c = 1 for the whole of

this document. Leading order production mechanisms for LQs in p-p collisions are shown in Fig. 1.3. At the energies typical of LHC collisions the dominant production mechanism of LQs is gluon-gluon fusion due to the large momentum fraction carried by the gluon within the proton at high energies. The production cross section for this process depends only on α_{strong}, the coupling strength of the strong force, and is independent of λ.

The LQ then decays to a lepton and quark, and the $\overline{LQ}$ to an anti-quark and an anti-lepton, as shown in Fig. 1.4.

Inter-generational mixing of the LQs is strictly bounded by current experimental limits on flavor changing neutral currents. If a sincle LQ could couple to multiple generations of quarks, an energetic quark could decay to a LQ and lepton, which could then recombine to a quark of a different flavor. The exclusion of such interactions implies LQs would exist in three generations with flavors corresponding to the generations of the leptons and quarks. This is in contrast to both quarks and leptons that show generational mixing through electroweak interactions, a clue that the mass of possible LQs could be very high. This analysis considers only first generation LQ pair production, resulting in a signal of two energetic electrons and two energetic quarks.

The pair production cross section for LQs depends both on the center of mass energy of the collision as well as the mass of the LQ, as shown in Fig. 1.5. This analysis uses data collected at a center of mass energy of 7 TeV.

Several searches for LQs at previous experiments have provided lower limits on the possible masses of all generations of LQs. At the Large Electron-Positron

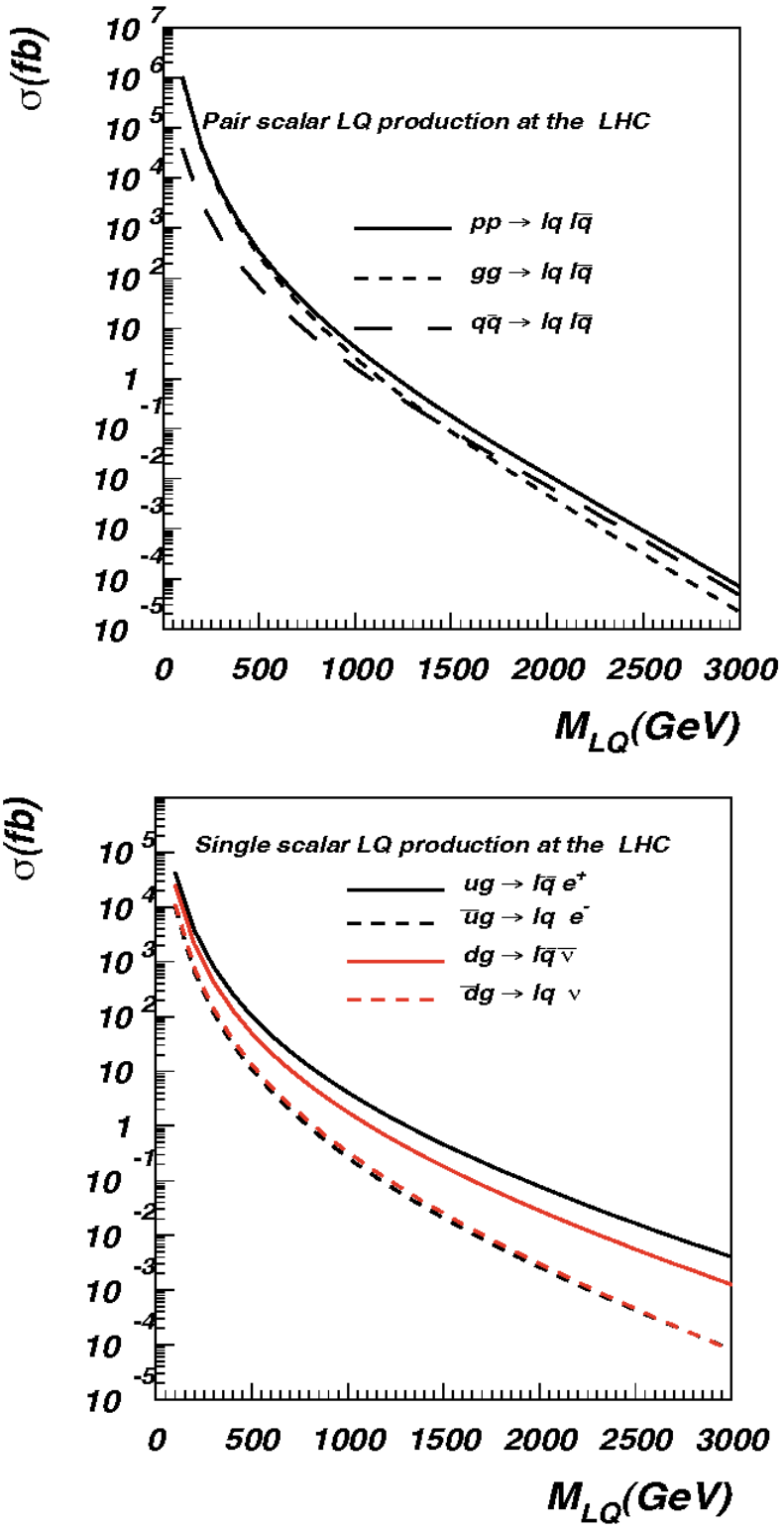

Figure 1.2: Top: Pair production cross section of scalar LQ at a center of mass energy of 14 TeV. Bottom: Single LQ production cross section at a center of mass energy of 14 TeV [17].

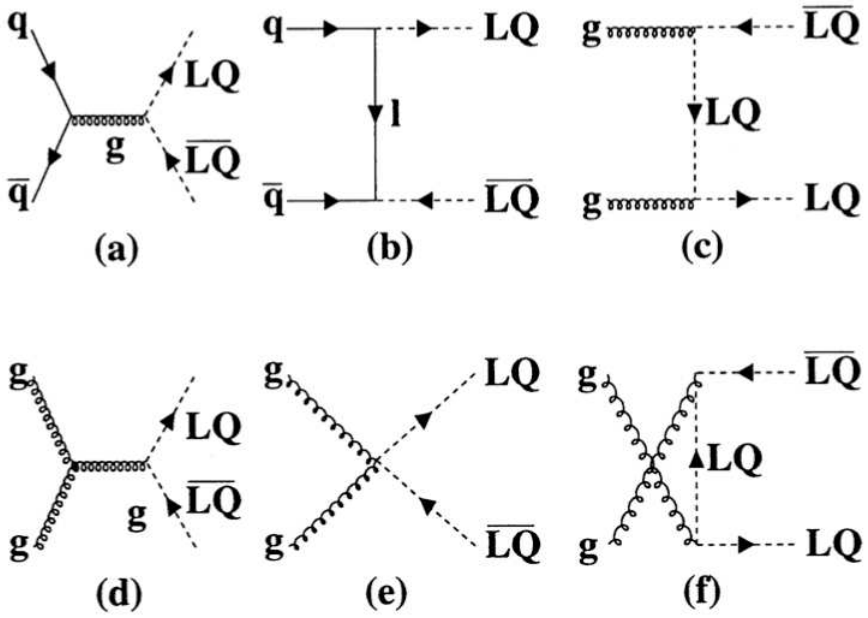

Figure 1.3: Tree level production mechanisms for first generation scalar leptoquarks [18].

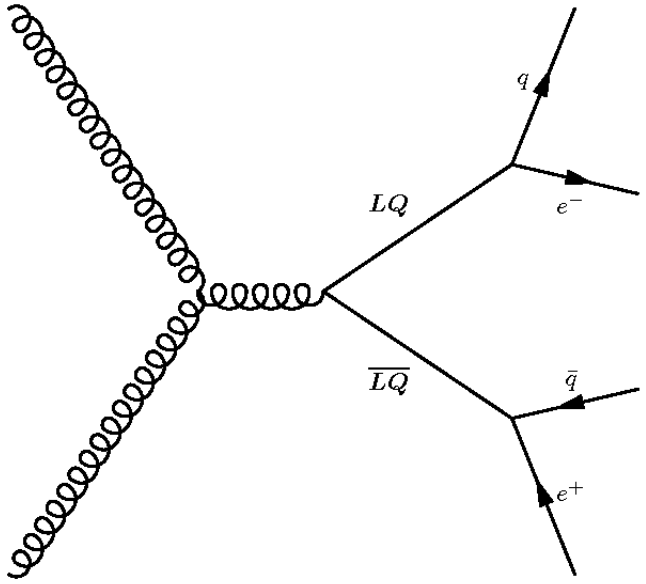

Figure 1.4: Dominant production and decay mechanism for first generation scalar leptoquarks at the LHC.

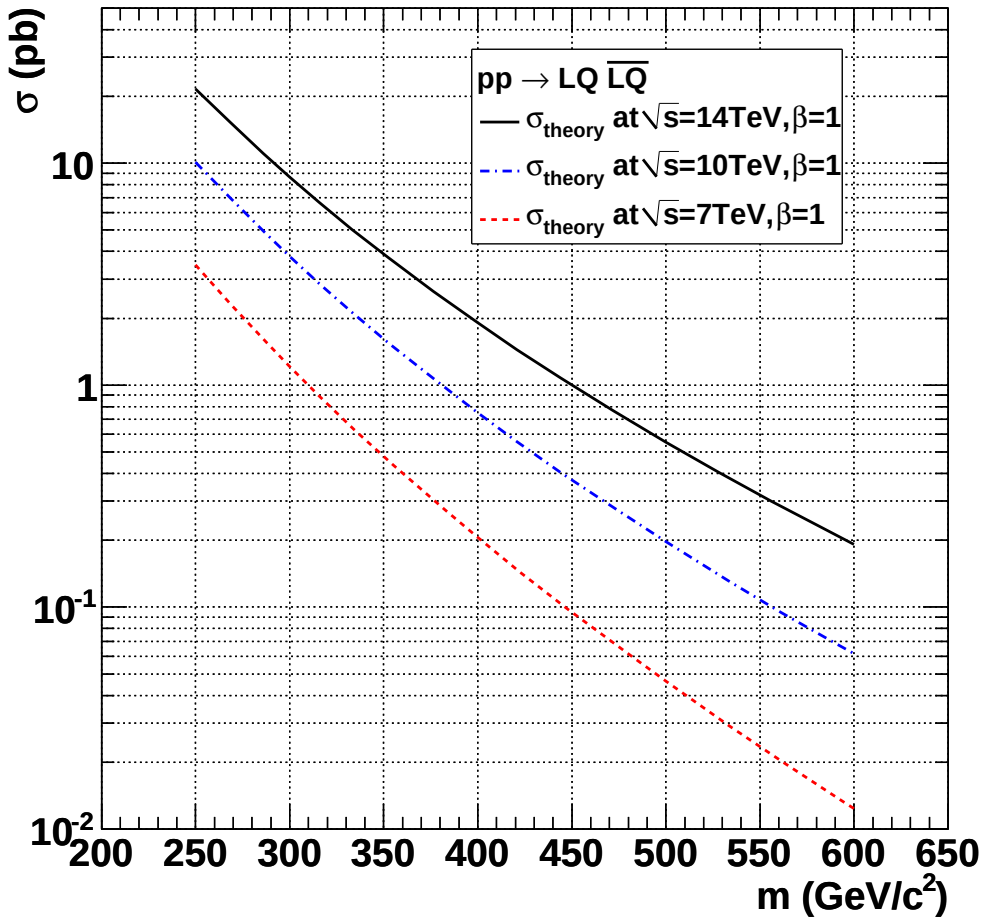

Figure 1.5: Pair production cross section of first generation scalar LQs at 3 different values of the center of mass energy for proton-proton collisions.

collider (LEP) at CERN (1989-2000), the existence of first generation scalar LQs was excluded below a mass of 45.5 GeV for pair production and below a mass of 65 GeV for single LQ production with a 95% confidence level [20]. The Hadron-Electron Ring Accelerator (HERA) in Hamburg, Germany (1992-2007) was able to set limits on the Yukawa coupling, λ as a function of LQ mass given the s-channel production possibilities in lepton-proton collisions. Results from HERA place λ on the order of α_{weak} or smaller with a 95% confidence level for LQ masses accessible at the LHC. Given such values of λ, masses smaller than 215 GeV were excluded for first generation scalar LQs decaying to electrons and quarks [21].

The most recent results from the DØ Collaboration at the Fermilab National Accelerator ($p\bar{p}$ collisions at a center of mass energy of $\sqrt{s}$=1.96 TeV) have placed the lower limit on the mass of first generation scalar leptoquarks with $\beta = 1$ at 299 GeV [15]. The analysis of the Tevatron data was conducted with 1 fb^{-1} of data. The region of the LQ mass vs β plane excluded by the DØ Collaboration is shown in Fig. 1.6. A previous combined result from the Collider Detector at Fermilab (CDF) and DØ with a combined integrated luminosity of approximately 250 pb^{-1} set a 95% confidence level lower limit on the mass of first generation scalar LQs at 242 GeV [23].

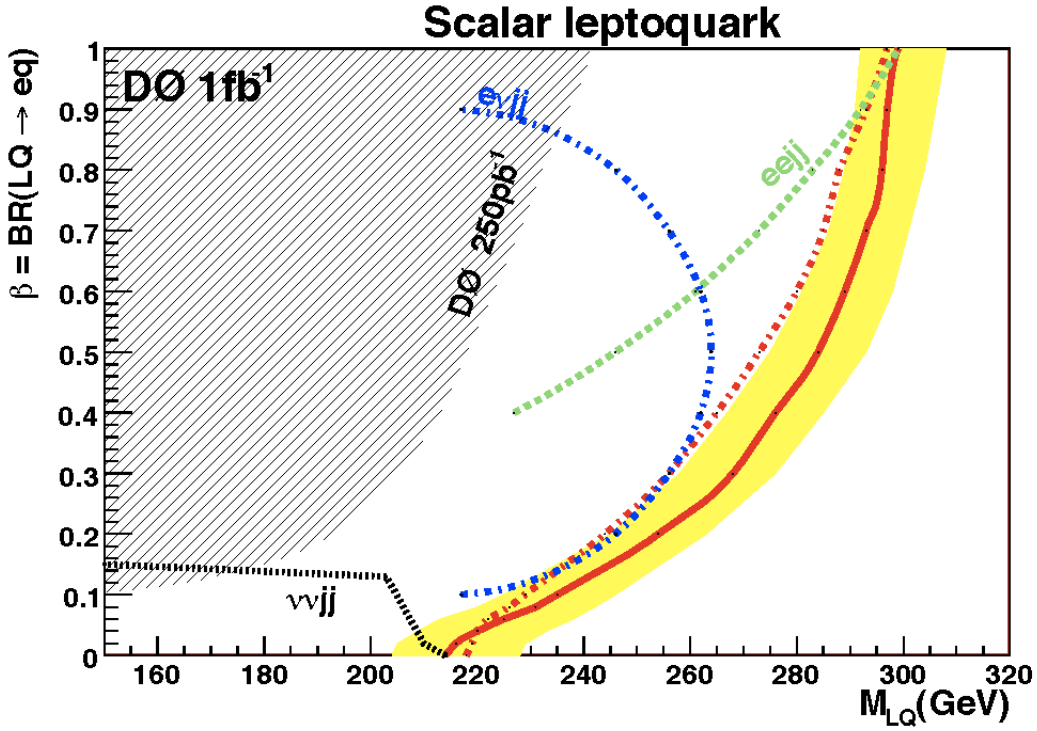

Figure 1.6: β vs LQ mass region excluded by the DØ Collaboration. The red line with yellow band represents the combined results of β=1, β=0.5, and β=0 [22].

Chapter 2

Apparatus

2.1 The Large Hadron Collider

Many of the particles in the SM are short lived and are rarely produced under conditions where they can be carefully observed in Nature. The study of these heavy, rare particles can be accomplished by producing them in collisions of very high energy particles. The energy of the initial particles is transformed in these collisions to mass energy of the heavier particles, which then decay to secondary particles that can be detected. The Large Hadron Collider (LHC) at the European Organization for Nuclear Research (CERN) achieves this by producing two counter rotating beams of protons accelerated to nearly the speed of light, and crossing the beams at 4 points around the ring to induce collisions, as shown in Fig. 2.1.

2.1.1 Proton injection scheme

To produce the beams, protons are first collected from hydrogen gas using a Duoplasmatron operating at 100 kV. The gas is fed into a cathode chamber and dissociates. Magnetic fields constrict the gas and force it through a canal where it is injected into the Linac 2 accelerator and accelerated to an energy of 50 MeV (0.3c). The protons are then injected into the Proton Synchrotron Booster (PSB) and accelerated to 1.4 GeV. The PSB feeds into the Proton Synchrotron (PS) and

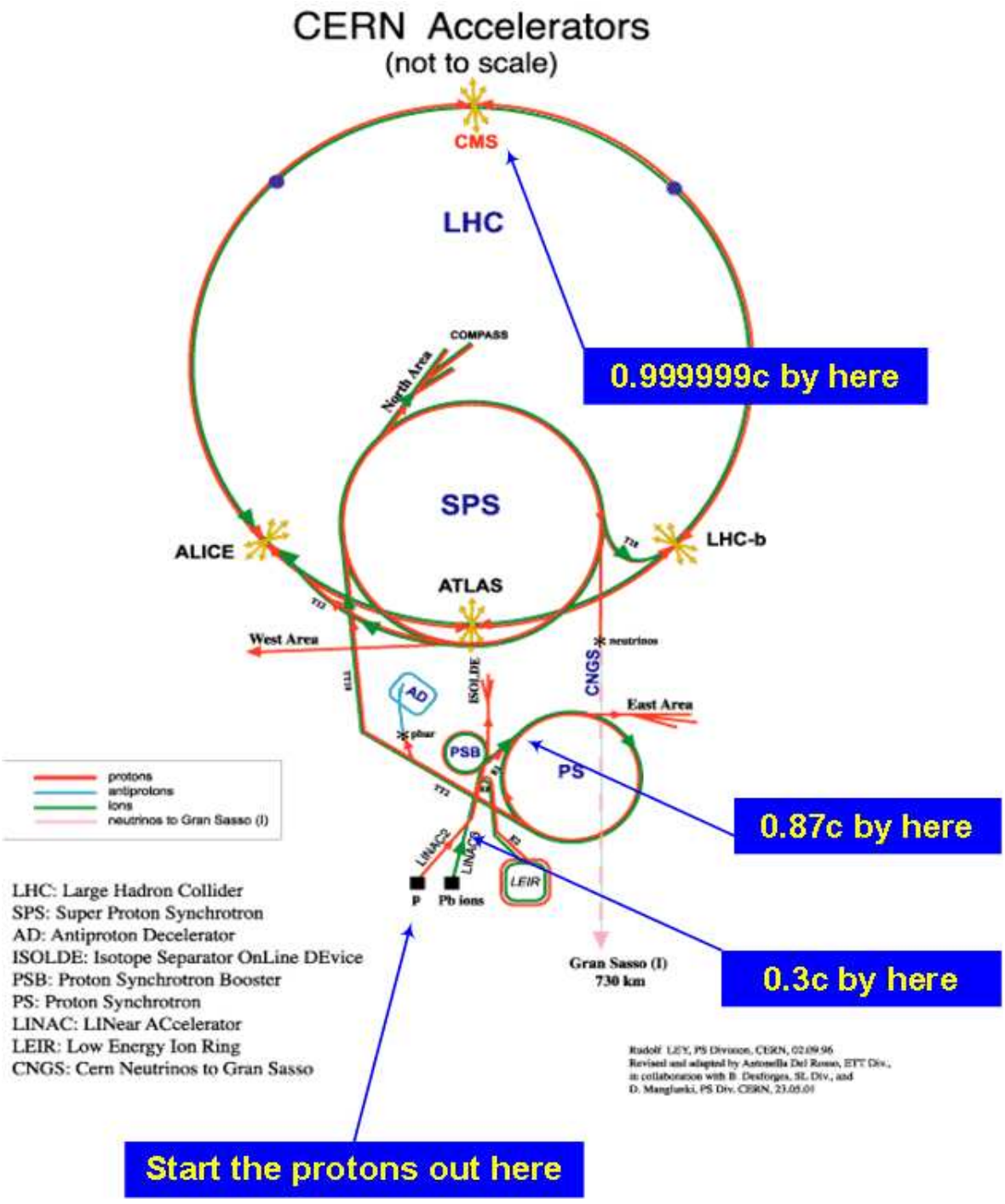

Figure 2.1: LHC proton injection chain at the CERN complex [24].

accelerates the beams to 28 GeV. In the PS the protons are arranged into bunches with a spacing of 25 nanoseconds. The beams are extracted from the PS and fed into the Super Proton Synchrotron (SPS) where they are accelerated to a beam energy of 450 GeV. After the SPS the protons are injected into the main LHC accelerator and accelerated to the full beam energy of 3.5 TeV [25]. The full design energy of the LHC is 7 TeV per beam. This is planned to be achieved in 2012.

2.1.2 Beam control

The LHC tunnel consists of cryogenically cooled dipole and quadrupole magnets arranged in a 27 km ring, housed in an underground tunnel between 50 and 100 m below the Swiss and French countrysides outside the city of Geneva. Once the protons are injected into the main LHC tunnel they are directed around the ring by 1232 dipole magnets. Radio-Frequency (RF) cavities operating at 400 MHz accelerate the protons to their nominal beam energy, and help maintain the beam energy as the protons radiate photons along their circular path. 16 Klystrons of 300 kW each are used to generate the 4800 kW of power required by the RF cavities controlling the beams, although only 275 kW is supplied to each beam directly. The beams are focused by 386 quadrupole magnets that squeeze the beams to a diameter of approximately 0.02 mm at the crossing points where the detectors are located [26].

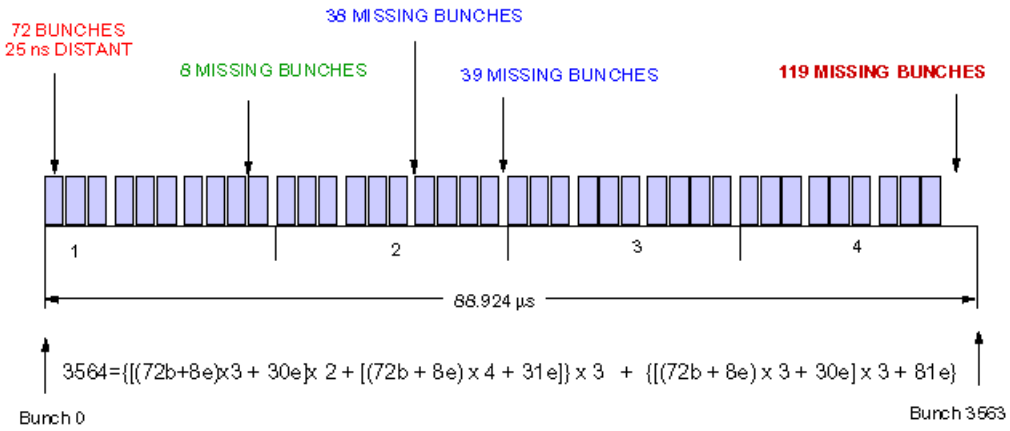

Figure 2.2: Representation of the beam structure of the LHC, showing 25-ns intervals filled with protons and gaps to allow time for magnet adjustments during beam dump conditions. The equation shows the pattern of filled bunches ("b") and gaps ("e") that sum to the total 3564 bunches in one orbit of the beam.

2.1.3 Beam structure

The 25-ns bunches of protons in the LHC beam are not continuous. Gaps are placed in the beam structure, as shown in Fig. 2.2, to provide opportunities for the beam to be steered toward a dump location in the event that the beam must be discarded. As the magnets are adjusted in the case of a beam dump, the path of the beam sweeps out an arc crossing potentially sensitive detector and beam control materials. A beam dump is designed to occur only when the empty bunches coincide with the time the beam path sweeps between the beam pipe and the dump location. The gap between bunches 3445 and 3564 corresponds to the LHC beam dump window. The smaller gaps correspond to beam dump windows from the smaller accelerators in the injection chain.

2.2 The Compact Muon Solenoid Experiment

The Compact Muon Solenoid (CMS) is a multi-purpose detector built around one of four beam crossing point at the LHC. A list of contributing authors to CMS publications as of November, 2010 can be found in Appendix E. CMS consists of 4 sub-detectors layered in a cylindrical barrel with two end-caps, as illustrated in Fig. 2.3, along with a system of forward detectors positioned close to the beam pipe at a variety of distances from the interaction point. A large electromagnet surrounds the inner barrel sub-detectors and produces a 3.8 Tesla axial magnetic field (2.4 GJ of stored energy) along the center of the detector. Closest to the center of the detector and nearest the collision point of the protons is the Inner Tracker, designed to provide a high-precision measurement of the curvature of the path of charged particles in the magnetic field. This is enclosed by an electromagnetic calorimeter and a hadronic calorimeter. The superconducting solenoid surrounds the barrel calorimeters and is followed by muon detection chambers. Information from each detector component is filtered using an online trigger system to determine which events to save. Beam monitoring is achieved with Beam Scintillator Counters (BSCs), a series of scintillating tiles providing hit and coincidence information, and the Button Beam Pickup (BPTX), designed to provide timing and bunch structure information.

A common coordinate system is used to define location within CMS. The z coordinate describes the distance along the beam axis away from the interaction point. The azimuthal angle, ϕ, is defined as the angle from the horizontal in a plane

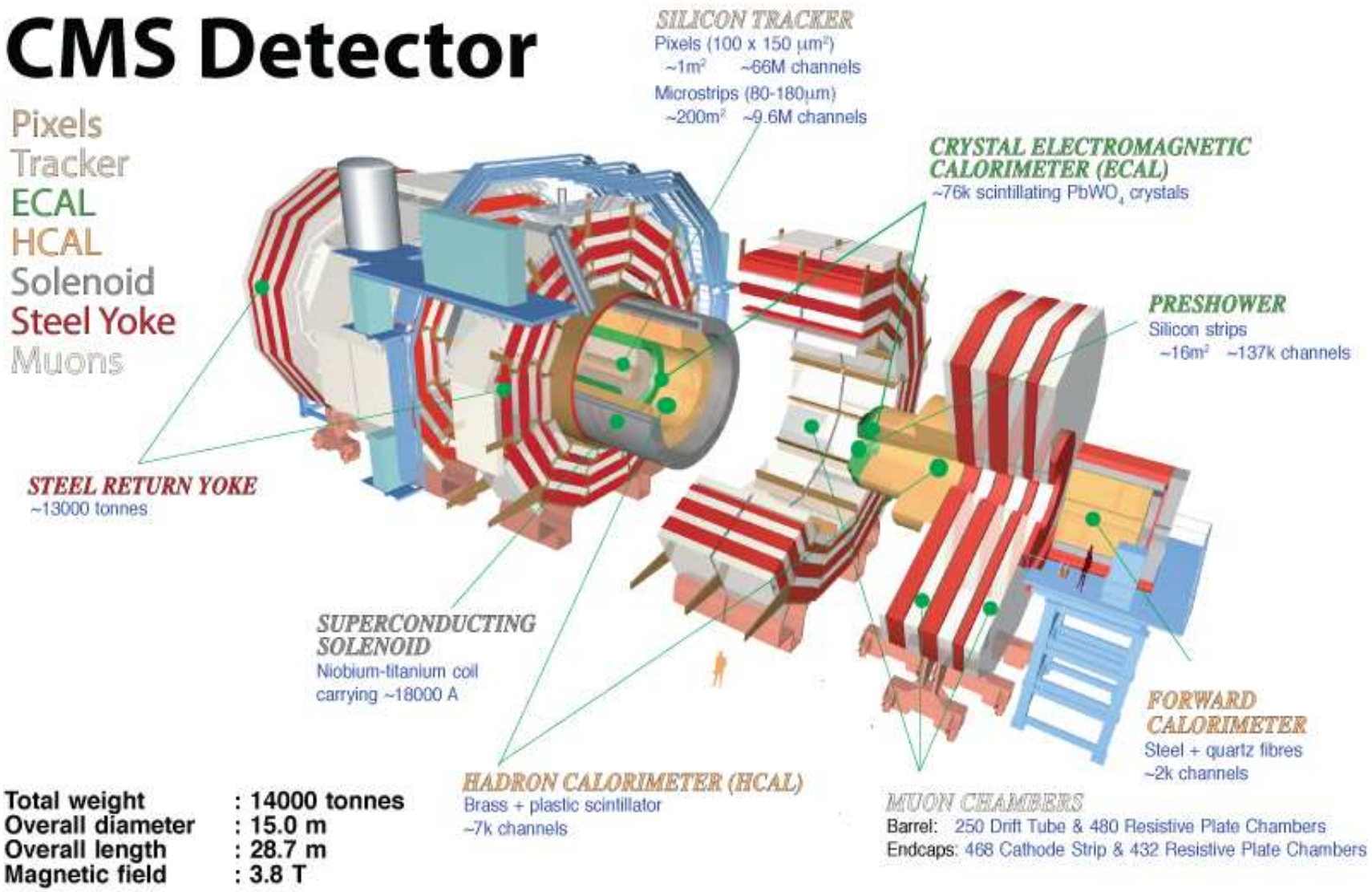

Figure 2.3: The Compact Muon Solenoid detector, shown with sub-detector systems in barrel and endcap regions, and forward hadron calorimeter [27].

perpendicular to the beam pipe, ranging from $-\pi$ to $+\pi$ with ϕ=0 pointing towards the center of the LHC ring. The polar angle, θ, is measured from the beam axis and has a range from 0 (pointing west, +z direction) to π. Pseudorapidity η, defined in Eq. 2.1, is often used instead of polar angle because, in the zero mass limit, the rate of particle production in minimum bias events (no hard scatter) is roughly constant as a function of η.

$$\eta = -ln(tan\frac{\theta}{2}) = \frac{1}{2}ln(\frac{|p| + p_L}{|p| - p_L}) \tag{2.1}$$

p_L is the component of the particle momentum along the direction of the beam axis. The opening angle between two particles when measured using pseudorapidity is invariant under Lorentz boosts along the beam axis.

2.2.1 The Inner Tracker

The tracking system located within the solenoid is composed of a high resolution pixel detector located between 4.4 cm and 10.2 cm from the interaction point, followed by a silicon strip tracker out to a radius of 1.1 m [28], as is shown in Fig. 2.4.

The LHC is expected to produce about 1000 particles hitting the inner surface of the CMS tracker in every 25 ns bunch at design luminosity, leading to a hit rate density of 1 MHz/mm^2 at a radius of 4 cm from the beam axis. In order to meet the demanding performance requirements on the tracking system, the design relies on a single channel occupancy at high luminosity of between 1% and 3%. This requires a pixilated detector at radii less than 10 cm.

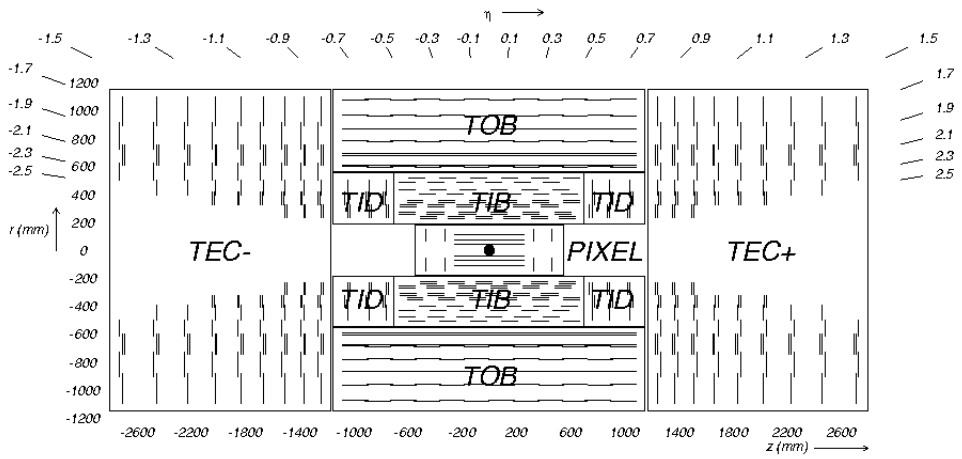

Figure 2.4: Inner Tracker of CMS, consisting of a pixel detector closest to the interaction point, followed by layers of silicon strip detectors in the inner barrel (TIB), outer barrel (TOB), inner disc (TID) and endcap (TEC) regions [29].

Each pixel contains a thin layer of depleted silicon (high resistance n-substrate). As a charged particle passes through the thin layer of silicon it creates electron-hole pairs that separate due to a bias voltage of 300 V across the chip. The buildup of charge is read out through an active amplifier. The pixel detector is three layers deep in the barrel region and two discs deep on each of the endcaps, for a sum of 1440 pixel modules and 66 million pixels.

At radii larger than 10 cm the particle flux is reduced by the preceding material, which allows the use of silicon micro-strip detectors. The two-dimensional position of the charged particle at each layer is determined by the combination of two signals from perpendicular, successive strips. This is in contrast to the pixels that provide three-dimensional information from a single hit. The strips are six inch wafers of n-doped silicon with p^+ implants on the front side. Radiation damage to

the silicon will eventually lead to the inversion of the silicon to p-type. Implants of n^+ on the back of the wafer allow the continued use of the $p-n$ junction after the inversion of the bulk material. In total there are 10 layers of strips in the barrel, three end disc layers with a radius of 55 cm extending to a z of 116 cm along the beam axis, and nine endcap layers at a radius of 113.5 cm for a total of 9.3 million strips.

2.2.2 The Electromagnetic Calorimeter

The electromagnetic calorimeter (ECAL) is composed of transparent lead tungstate ($PbWO_4$) crystals cut in truncated pyramidal shapes aligned in a quasi-projective direction toward the interaction point in order to minimize the amount of non-instrumented material aligned with particle trajectories [30], as shown in Fig. 2.5. As a charged particle traverses a crystal it scintillates, emitting photons with wavelengths between 420 and 430nm. The scintillation light is reflected off the polished sides of the crystal, and directed to avalanche photodiodes (APDs) at the end of the crystals in the barrel region, and to vacuum phototriodes (VPTs) in the crystals in the endcap. The phototriodes are photomulitpliers with a single gain stage, making them less effected by the non-uniform magnetic field and high radiation environment of the endcap. The CMS ECAL phototriodes contain a gain of approximately 9.5 at design operating conditions. The charge collected from the APD or VPT is a measure of the energy of the original particle.

The barrel region of the ECAL (EB) contains 61,200 crystals, while the two

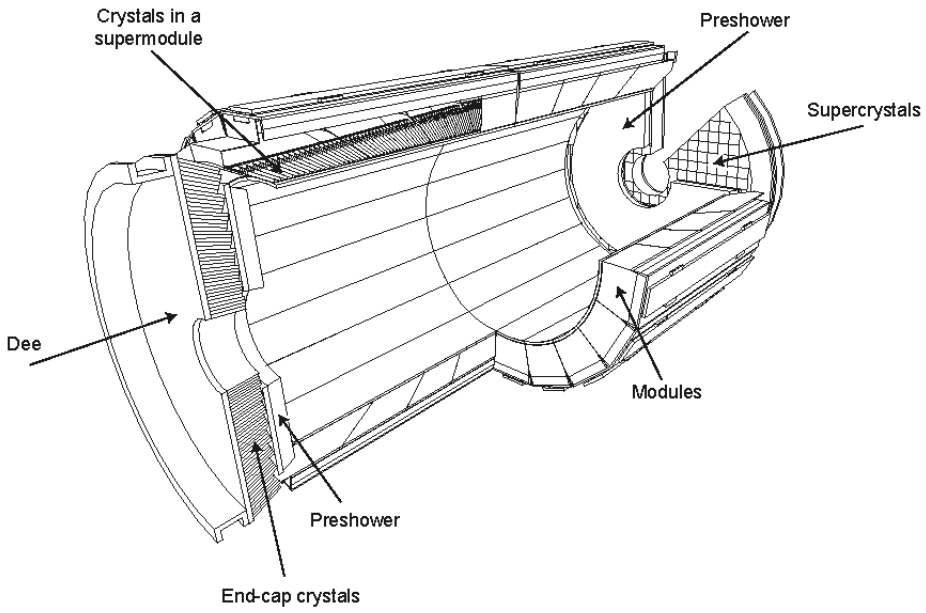

Figure 2.5: CMS Electromagnetic Calorimeter: Cross section of modules in the barrel region and Dee components in the endcap region [31].

endcap regions contain 7,324 crystals each. Lead tungstate is particularly well suited for compact electromagnetic shower measurements due to its small Moliere radius of 2.2 cm, and short radiation length of 0.89 cm. This can be compared to competing designs of liquid argon calorimeters with a Moliere radius of 10.1 cm and radiation length of 14 cm. The scintillation decay time for these crystals is such that approximately 80% of the light is emitted within the 25ns beam crossing window. This and the small rise time for the APDs and VPTs (less than 2ns for the APDs in the barrel) allow nearly all the scintillation photons from charged particles to be collected before the following beam crossing.

The transparency of the crystals degrades under high levels of ionizing radiation. Color centers form in the crystals, resulting in a loss in light transmission

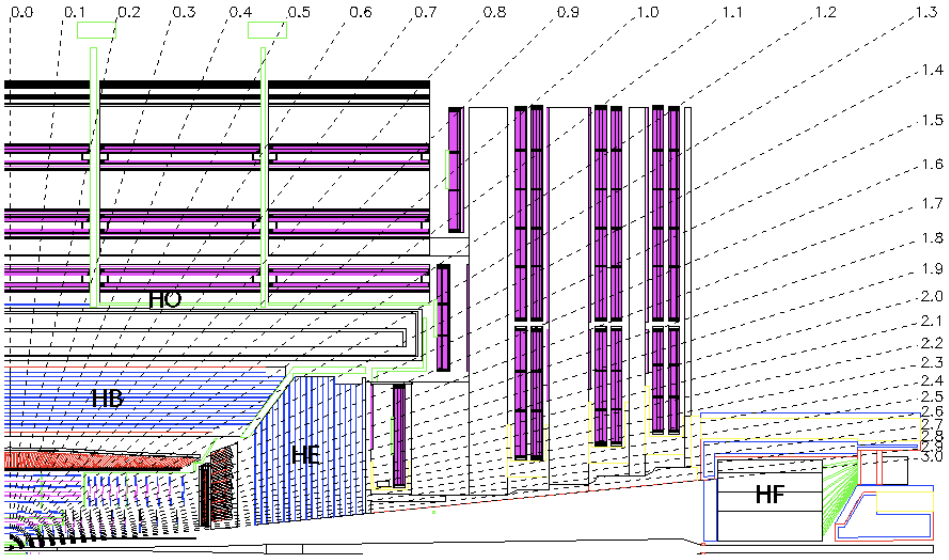

Figure 2.6: CMS Hadronic Calorimeter: barrel (HB), endcap (HE), outer (HO) and forward (HF) regions [34].

at particular wavelengths. Calibration of and correction for the transmission loss is achieved by measuring the response in the crystals to injected laser light during the gap in filled bunches once per full orbit of the beam in order to monitor the response over the lifetime of the experiment.

2.2.3 The Hadronic Calorimeter

The hadronic calorimeter (HCAL) consists of 4 components: the barrel, endcap, outer, and forward regions [32], as shown in Fig. 2.6. The barrel and endcap regions lie directly outside those of the ECAL, while the outer region of HCAL is located outside of the solenoid, directly before the muon detection chambers. The forward region lies past the endcap of the muon detector, the front face lying at a distance of 11.2 m along the beam axis from the interaction point.

The HCAL in CMS is a sampling calorimeter consisting of alternating layers of dense absorbing material and active scintillation material. High energy hadrons traveling through the detector deposit energy in the absorber and generate hadron showers as they interact with the material. As the showers pass through the scintillator layers, each charged particle in the shower produces light that is collected and registered as charge on the high-voltage photodiodes (HPDs) [33]. The size and density of these showers provide a measure of the energy of the original particle.

The absorbing plates in the barrel region (HB) consist of a 40 mm-thick front steel plate, 14 brass plates varying in thickness from 50.5 to 56.5 mm, and a 75 mm-thick steel back plate. The steel plates on either side of the barrel are included to increase structural strength. Between the absorbing plates are 3.7 mm-thick tiles of plastic scintillator containing wavelength shifting waveguide fibers to collect the light and direct it to HPDs. The endcap region (HE) consists mostly of 19 layers of 79 mm-thick brass plates with 9 mm gaps for the scintillator tiles, although parts of the endcap overlapping with the barrel have as few as six layers of brass. Overlap of the barrel and endcap regions achieves a minimal amount of projective dead material from the interaction point.

Particles of very high energy create proportionally large showers in the absorbing material of the HCAL. With so many particles in the shower there is a chance that some will penetrate the full depth of the detector and"punch through" the final layer. Instrumented scintillator tiles are placed outside of the solenoid in the barrel region where the number of interaction lengths of the inner HCAL is smallest in order to catch the tails of the largest showers. This outer calorimeter (HO) uses the

first layer of steel of the solenoid return yoke as the absorbing material. In the most central portion of the barrel two layers of scintillator tile are sandwiched around the first layer of steel return yolk. Along the rest of the barrel region the scintillator tiles are placed only on the outside of the first steel return yolk layer.

The forward calorimeter (HF) has a small overlap region with HE and extends to an η of 5 on either side of the interaction point. Due to the large forward momentum of the initial partons, the majority of the final state particles will travel away from the interaction point at small angles relative to the beam axis, resulting in a more severe radiation environment for detectors in the forward regions. Additionally, the beams contain a "halo" of particles with orbits slightly off from the nominal beam orbit that interact with detector material close to the beam pipe. Quartz fibers are used instead of scintillator tile in the HF due to the high radiation environment. The absorbing material is steel. The fibers are placed into machined grooves in the steel parallel to the beam pipe. Cherenkov light produced from particle interactions with the quartz is directed to photomultiplier tubes (PMTs). The steel of HF provides enough shielding from radiation to make the use of PMTs feasible. Both electromagnetic and hadronic showers will stimulate light in the fibers of the HF. In order to discriminate between these types of showers half the fibers are shorter, covering only the back portion of the HF. The electromagnetic (EM) interaction length in steel is significantly smaller than the nuclear interaction length, causing the EM showers to dissipate early and deposit less energy in the shorter fibers.

2.2.4 The Muon Detector

The CMS solenoid produces a 3.8 T magnetic field along the center of the detector. Outside of the solenoid the field is contained nearly entirely in layers of steel return yokes enclosing the endcap and barrel regions. This containment helps make the solenoidal field more uniform. The layers of the muon system are interspersed between the return yokes of the magnet and employ three types of technology: drift tubes, cathode strip chambers and resistive plate chambers [35].

The drift tubes (DTs) are rectangular tubes between 2 and 3 meters in length containing an Ar/CO_2 gas mixture, as shown in Fig. 2.7. A voltage of 3.6 kV is applied to a central anode wire. Electrode strips on the top and bottom of the tubes and cathode strips along the sides of the chamber help shape the field inside the tube to keep the drift velocity relatively uniform over the volume of the tube.

As a charged particle passes through, the gas is ionized and the freed charge is drawn to the central wire, registering a current, as shown in Fig. 2.7. Measurement of the signal timing gives information on the distance of the charged particle's path from the wire in the tube. Successive signals in layers of perpendicular tubes allows three-dimensional reconstruction of the particle's path.

In the barrel region there are four layers of rectangular DT chambers at increasing radii from the beam axis, as is shown in Fig. 2.8 by the rectangles labeled "MB/Z/X/Y". Each chamber contains a layer of tubes running parallel to the beam, followed by an aluminum honeycomb plate for support and structure, followed by a layer of tubes perpendicular to the beam and another layer of tubes parallel to the

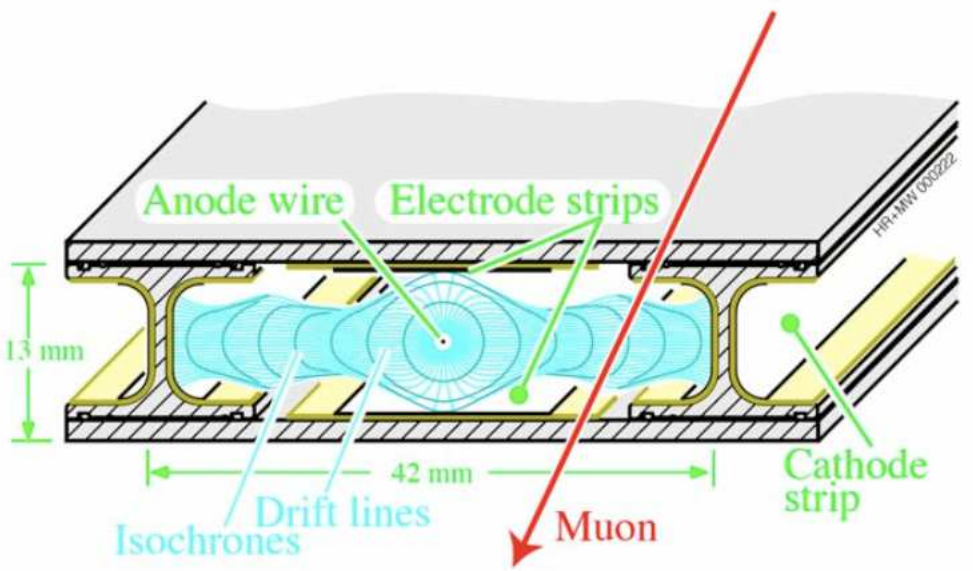

Figure 2.7: Cross sectional view of a drift tube used in the CMS DT sub-detector [36].

beam axis. In total, the DTs contain approximately 172,000 sensitive wires.

The environment in the endcap is significantly different than that of the barrel. The magnetic field is stronger and less uniform, the radiation environment is more harsh and the expected signal rate is higher. In light of these constraints the muon system in the endcap employs four layers of cathode strip chambers (CSCs) at increasing z, as shown in Fig. 2.9.

A CSC is composed of seven trapezoidal panels with gaps between each pair of panels filled with an $Ar/CO_2/CF_4$ gas mixture and planes of closely spaced anode wires. Cathode strips running perpendicular to the anode wires (radially outward from the beam axis) line the panels. Ionizing charged particles passing through the chamber cause an avalanche of charge drawn to the anode wires, which in turn

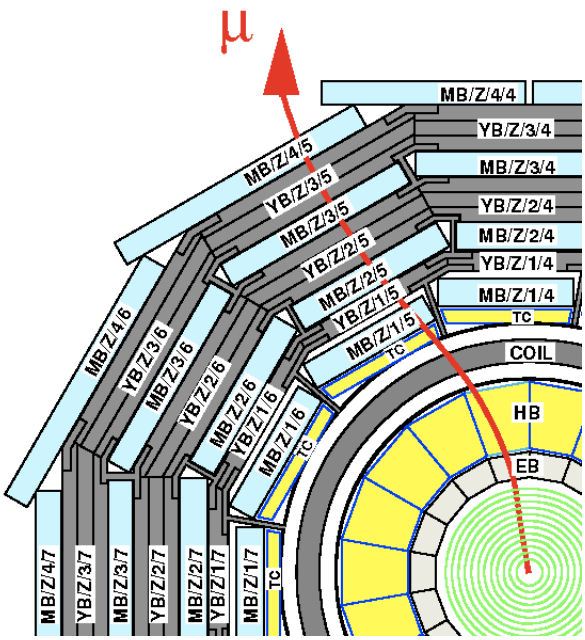

Figure 2.8: Location of the drift tube modules in the CMS barrel region [37].

induces an image charge on the cathode strips. Readout of both the anode wire and cathode strip allows two-dimensional imaging of each particle's path. The entire CSC sub-system contains approximately 220,000 cathode strip channels and 180,000 anode wire channels.

Muons, being relatively easy to detect due to their charge and smaller radiation losses in matter than electrons, offer a uniquely clean signal for triggering the data collection of interesting events. Panels of resistive plate chambers (RPCs) are located in the muon system in both the barrel and endcaps with the specific goal of providing additional fast and precise information to the trigger system to compliment the trigger information passed from the DT and CSC systems. The RPCs are gaseous parallel-plate double-gap chambers with a charge integration time smaller

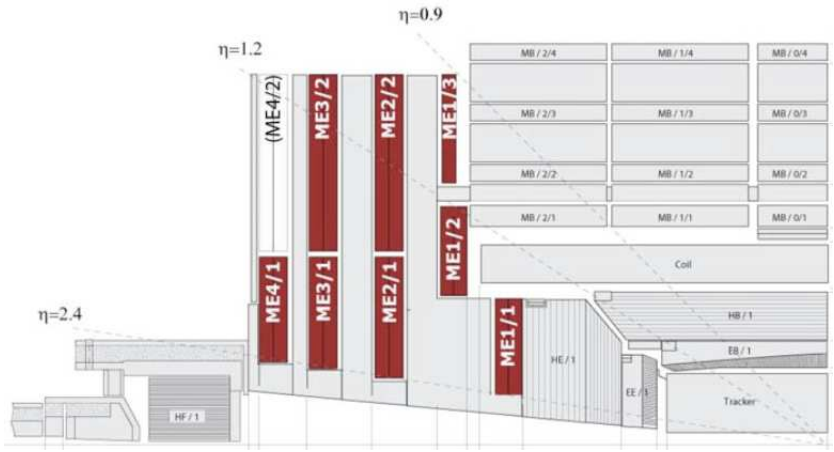

Figure 2.9: Location of cathode strip chamber modules in CMS endcap region [38].

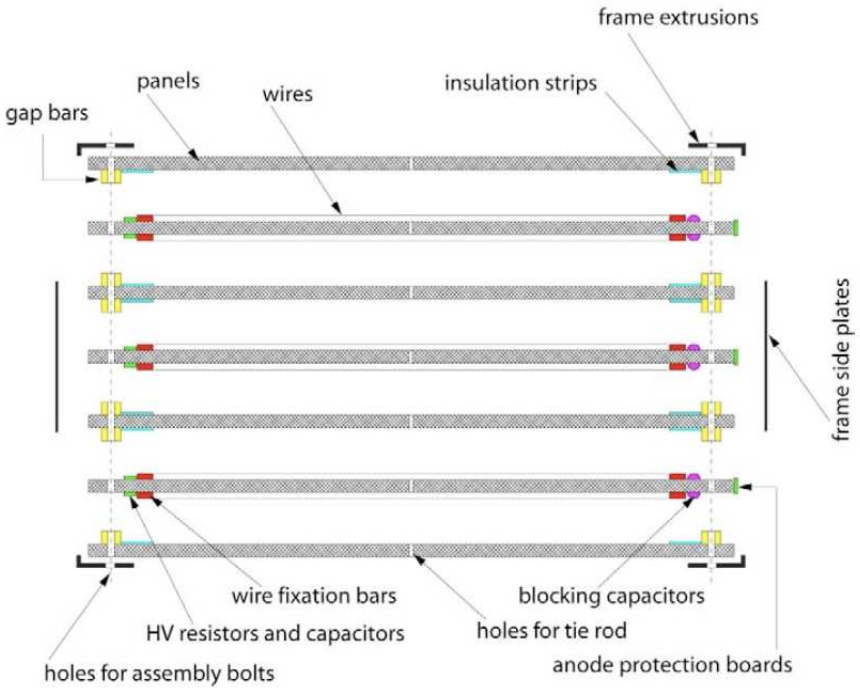

Figure 2.10: Cross sectional view of a cathode strip chamber [39].

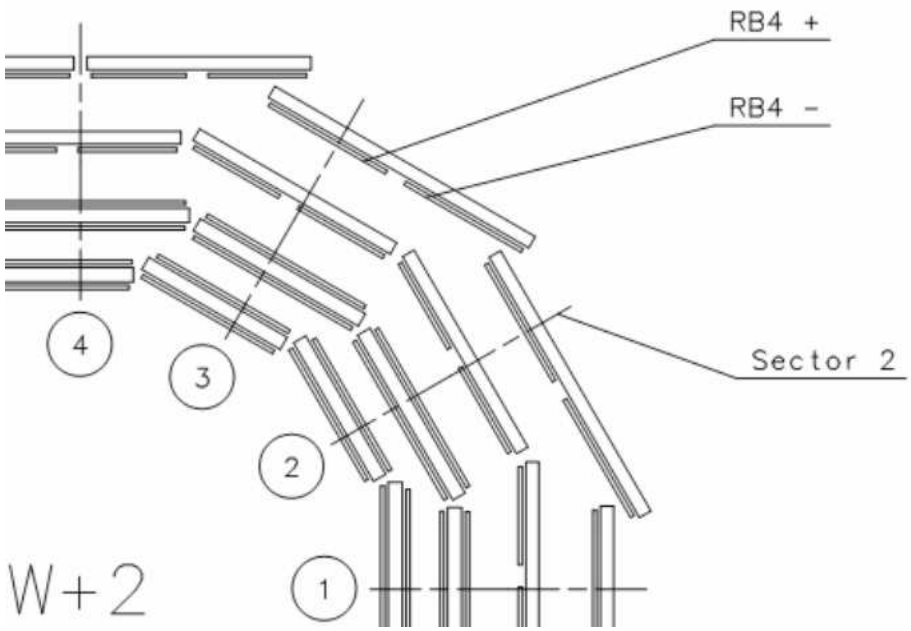

Figure 2.11: Location of resistive plate chambers in CMS barrel region [40].

than the 25-ns bunch structure of the LHC. Each signal is therefore uniquely associated with a beam crossing, despite the expected high rate of ionizing tracks.

In the RPCs a plate of high voltage read-out strips located in the center of the chamber separates two gas filled gaps. As a charged particle passes through the chamber an avalanche of charge is induced in both gaps and the two signals are summed. The small width of the gaps accounts for the fast read-out capability.

The barrel region contains one RPC on each side of the DTs in the first two layers, and one RPC on the inner side of each DT in the outer two layers for a total of 6 RPC layers (Figure 2.11), while each endcap contains 3 RPC layers.

2.2.5 The Forward Detectors

The region of the detector closest to the beam pipe is covered by two forward sub-detectors, the Zero Degree Calorimeter (ZDC) and the Centauro And Strange Object Research detector (CASTOR) [41]. Each detector contains an electromagnetic (EM) section and a hadronic (HAD) section, both sampling calorimeters made of tungsten and quartz similar in design to HF. Relativistic charged particles produce Cherenkov light in the quartz that is directed to PMTs using air-core light guides. The tungsten plates act as absorbers.

The ZDC is composed of two identical calorimeters located approximately 140m along the beam pipe on either side of the CMS interaction point, outside the CMS experimental cavern. The EM section is located closest to the beam crossing area and contains 33 layers of alternating 2 mm-thick tungsten plates and ribbons of 0.7 mm diameter quartz fibers, as shown in Fig. 2.12. After exiting the tungsten the fibers are divided into bundles creating five horizontal readout channels. The HAD section contains 24 layers of 15.5 mm-thick tungsten plates oriented at 45° to the beam axis to increase the Cherenkov light production, alternating with ribbons of 0.7 mm diameter quartz fibers. The HAD fibers are grouped into 4 longitudinal readout channels, yielding a total of 9 channels from each side, 18 in the total ZDC detector.

The ZDC is uniquely situated to contribute greatly to diffractive studies in proton-proton collisions, and to compliment the very forward regions of CMS in Pb-Pb collisions.

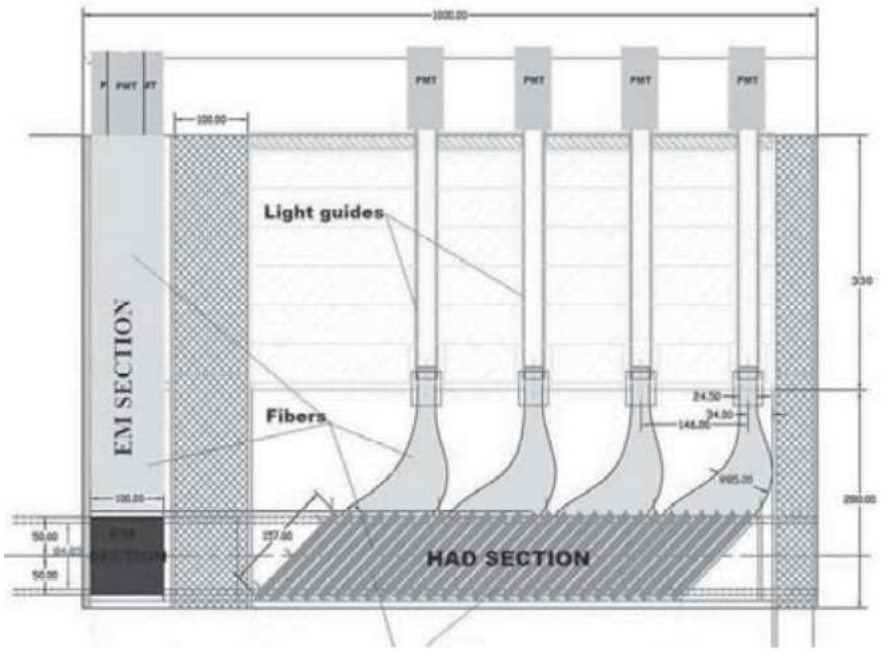

Figure 2.12: Zero Degree Calorimeter in CMS [42]

CASTOR is also composed of two calorimeters on either side of the interaction region. The CASTOR calorimeters sit directly behind the HF on the beam axis, inside the CMS experimental cavern, approximately 14.4 m from the interaction point. The detector components are wedges built into two half cylinders that, when closed, entirely surround the beam pipe. In each wedge the EM section is nearest the interaction area with 10 vertical 5.0 mm tungsten plates and 10 1.0 mm quartz plates, as shown in Fig. 2.13. These are split into two readout channels. The HAD section contains 60 10.0 mm tungsten plates and 60 4.0 mm quartz plates inclined at an angle of 45° to the beam axis, split into 12 readout channels. The CASTOR calorimeters on both sides have 8 wedges each, giving a total of 224 channels.

The physics goals of CASTOR are to compliment the nucleus-nucleus physics

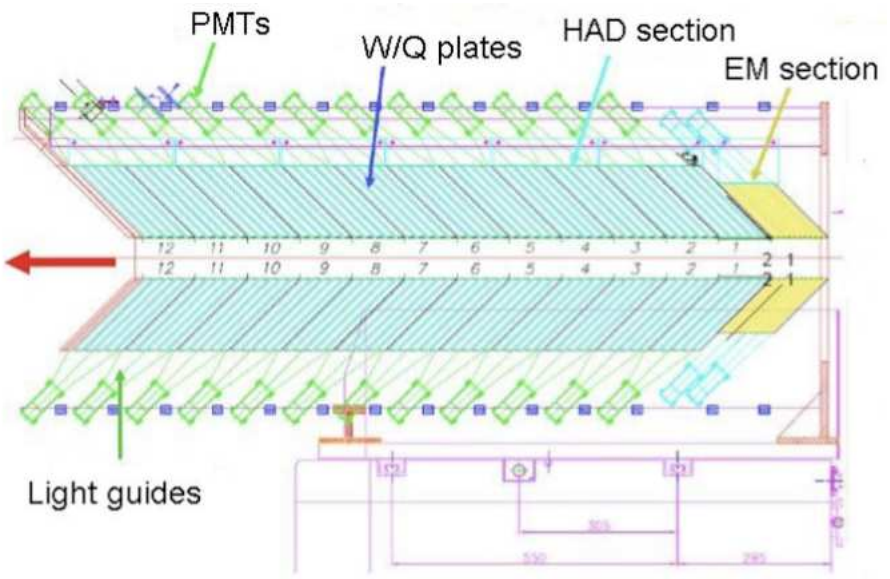

Figure 2.13: CASTOR sub-detector in CMS [43]

program at high rapidity, and to provide information on Centauro related phenomena [44], events first observed by high altitude cosmic ray observatories and characterized by the high energy contained in the shower (occasionally more than 8000 TeV).

2.2.6 The Trigger

The expected high rate of interactions at the LHC (nearly 10^9 Hz of proton-proton collisions at design luminosity) and the large number of read-out channels associated with one event in CMS make it unfeasible to read out and store data from every bunch crossing. The trigger system provides a fast decision chain using input from all detectors to determine if the information from individual bunch crossings warrants saving [45], minimizing dead time associated with readout.

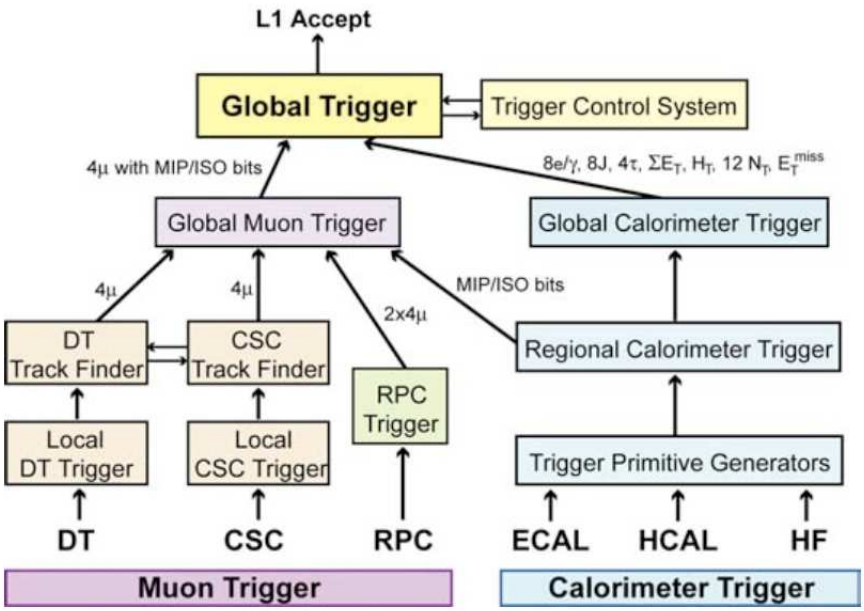

Figure 2.14: Diagram of information flow in the Level 1 trigger chain in CMS [46]

There are two main components of the trigger system: Level 1 (L1), which uses mostly specialized programable electronics located on the detector or in the electronics cavern directly adjacent to the detector, and the High Level Trigger (HLT), a software system implemented on an array of approximately 1000 commercial processors located above ground next to the CMS control room.

The L1 trigger receives coarse information passed up the trigger chain from each sub-detector while the full readout of each event is stored in buffers, as is shown in Fig. 2.14. It is designed to operate at an output acceptance rate of 100 kHz, achieving a reduction in event rate by a factor of approximately 400 from the 40 MHz beam crossing rate of the LHC.

The calorimeters pass a coarse sum of energy deposits in small areas (trigger

towers) to the Regional Calorimeter Trigger (RCT), which sums transverse energy from the different calorimeters in the trigger towers and identifies electron/photon candidates. The RCT is responsible for translating channel-oriented energy deposits into $\eta-\phi$-oriented physics objects for evaluation of the L1 criteria. This information is passed to the Global Calorimeter Trigger (GCT), which makes global energy sums such as missing transverse energy, total transverse energy, H_T (sum of energy of all jets above a threshold), and clusters of energy as an approximation of hadron jets.

The trigger chain for the muon systems runs in parallel to the calorimeter trigger path. It consists of local DT and CSC triggers that feed track finding algorithms, and the RPC trigger. All muon triggers are collected by the Global Muon Trigger (GMT), which also accepts information from the RCT. The GMT and GCT information are combined and processed by the Global Trigger (GT). The GT may issue a L1 Accept back to the trigger chain, which then is propagated down the tree to all sub-detectors so that the correct event information is sent to the data acquisition system (DAQ), which is in turn used as input for the HLT.

The information passed through the L1 chain contains no specific reference to the corresponding bunch crossing. When a L1 Accept command is received by a sub-detector the delay due to each step in the trigger chain must be accounted for when selecting the event information from the buffer to send to the DAQ. This synchronous pipeline nature of the system demands careful calibration by each sub-detector.

The HLT software is flexible, designed to change over time. Unlike the L1 Trigger, the HLT has access to the full readout of all the detector information. It

selects and sorts events based on menus of triggers, some requiring complex calculations based on the event content. The final output rate of the HLT is designed to be no more than 100 Hz, an overall combined L1 and HLT reduction in the event rate by approximately a factor of 4×10^5.

Chapter 3

Event Generation and Simulation

Comparison between the measured results of an experiment and the theoretical expectations is an important indication of how well one understands the process measured. Theoretical calculations for high energy proton collisions are relatively straightforward for interactions at tree level, where partons from the protons either exchange a boson or fuse to form a particle that then decays. However, the outgoing particles are electrically charged and so radiate energy as they bend in the magnetic field or pass through detector material (bremsstrahlung), creating showers of charged particles. If the outgoing particles are colored they will hadronize, resulting in a jet of colorless particles. An additional complication comes from initial processes that involve virtual intermediate states in the interaction. All of these factors lead to difficult, if not impossible calculations in a practical sense if all vertices are considered at the same time.

Tools to approximate these complex events have been developed in order to produce simulated data that can be easily compared with experimental data from real collisions. Monte Carlo algorithms are used to mimic the probabilistic nature of each interactions in order to generate a spectrum of events similar to that seen in data. Modeling these interactions with some accuracy is essential for many reasons: it allows testing of designs before detectors are built, it provides a development bed

for software tools to analyze the data, it aids in predicting the topology and rates of interesting events so that searches may be tailored to a particular signal, and it helps interpret the data results within the context of what is understood about the SM.

The production of these artificial events is broken into two steps: event generation, which mimics the collision of the protons in the hard scatter and any radiation from initial or final particles; and event simulation, which models the interaction of the particles produced in the initial collision with the detector material.

3.1 Event Generation

The goal of event generation is to create a list of all outgoing particles produced from the interaction of two incident particles, along with the physical properties of the outgoing particles such as momentum and position. The approach of most event generators is to split the particle generation into smaller pieces. The user may request a particular hard scatter process, or sets of processes. Final state particles are predicted based on matrix elements for the quantum field interactions. All possible channels for the requested process are considered and added appropriately. After the parton interaction processes are considered the initial and final state particles are allowed to radiate via both the electromagnetic and strong force, producing initial and final state radiation (ISR and FSR) and increasing the number of final state particles. Finally, all final state particles are allowed to hadronize to jets of colorless particles using approximations of the strong interaction.

Details of how ISR and FSR are simulated differ between various event generation tools, resulting in differences in hadron jet topologies between the various tools. The final state under study by the user may dictate which tool most accurately represents the collision events of interest.

3.1.1 Pythia

PYTHIA [47], one of the most widely used event generation tools, uses matrix element calculations for the pure hard scatter process, not including any ISR or FSR in the interaction at the matrix element level. Any colored particle in the initial or final state is then allowed to hadronize according to a parton shower model called the 'Lund string model'. The confinement of strongly interacting particles, leading to the proliferation of colorless particles in hadron jets, was previously not well implemented in event generators. The success of the Lund model in predicting results at the PETRA and PEP e^+e^- experiments led to its widespread acceptance.

The string model approximates the strong interaction as a stretchable string connecting any two quark pairs. The potential energy of the string increases as the particles move apart. When the energy stored in the string becomes greater than the mass energy of a quark-antiquark pair the string is broken and a new quark pair created, connecting to the initial particles so as the minimize the energy in the new strings. Radiated gluons increase the tension in the string by adding small kinks along the length of the string, increasing the energy stored. The shower of partons continues as each new string stretches and again breaks, with no bound to

the number of branches per event.

Because of the nature of the approximations used for gluon radiation, this method poorly predicts the rate of multiple jets with large separation. It does, however, predict well the substructure of each jet, as this is formed by nearly collinear radiation and hadronization, both processes that are well modeled by the Lund method.

3.1.2 Matrix Element Generators

The accurate simulation of events with large jet multiplicities has become more important as modern colliders have shifted to hadron-hadron collisions, and as accelerator energies have increased. Parton shower event generators such as PYTHIA do a poor job of predicting the rate of events with multiple jets that are well separated. Such jets arise from higher order processes and can not be modeled accurately with approximations for collinear gluon radiation.

Several event generation programs have been developed that use exact matrix element (ME) calculations for ISR and FSR contributions up to a cut-off energy, then merge the result with traditional parton shower generators for the hadronization step. Gluon radiation is added to the pure hard scatter processes in the ME calculation where the final state particles are above some energy threshold, Q_{cut}. Particles below the cutoff energy are passed to a parton-shower based generator with the assumption that below this energy the approximation of the process used by the showering algorithm is relatively accurate. This method takes into account

possible interference of multiple channels before determining the amplitude of a particular final state, leading to a more accurate representation of multijet events.

Cone algorithms are used to identify jets after the parton-shower stage and final state jets are matched to ME level partons. It is possible for events with nearly identical jet topologies in an overlap region of phase space to be generated from final state gluon radiation either at the ME level or from parton shower hadronization. To avoid double counting of these events the ME event weight is adjusted based on the number of jets after the parton shower to achieve exclusive samples at the scale of Q_{cut}.

The various ME generation tools differ in how they calculate the matrix elements and how they perform the integration of the squared amplitude over the phase space. Alpgen [48] is one example of an event generator that uses exact leading order matrix element calculations (in the perturbative QCD expansion) of the differential cross section for partonic final states. It contains approximately 15 basic pre-defined hard scatter processes that are added to final state gluon radiation to produce events with higher jet multiplicities. The MEs are calculated with the ALPHA algorithm [49], which considers the Green's function generator for the associated Lagrangian. This method preserves the full color and spin information, which is taken into account in processes with heavy particles in the final state.

Madgraph [50] [51], another popular ME generator, uses predefined Feynman rules to calculate all possible subprocesses based on the requested hard scatter process. It then produces a mapping for the required integration over phase space by identifying singularities in the Feynman diagrams. A partner program, MadEvent,

generates standalone code to calculate cross sections and unweighted events. The user can generate any number of events and pass them directly to a parton-shower generator for hadronization.

3.1.3 Parton Distribution Functions

Both ME and parton shower generators require the cross section of specific processes as input in order to generate an appropriate spectrum of events. Given two initial partons q_i and q_j with known momenta and n final state partons q_n with known momenta and n small (typically ≤ 3), perturbative QCD can predict the cross section of the process $q_i + q_j \rightarrow \sum_n q_n$. Theory calculations can not, however, predict the distribution of momentum among the partons within the proton. Parton distribution functions (PDFs) describing the fractional momentum of the initial proton carried by each constituent must be determined experimentally, then convoluted with the momentum specific QCD cross section to get the total cross section.

Experimental data from deep inelastic scattering experiments (Section 1.1.1), fixed target neutrino experiments and well understood processes in p-p collisions are used to fit functions describing the fraction x of the total proton momentum carried by each parton. The p-p cross section of any process can then be factorized into probability functions, as shown in Equation 3.1, where $P_1,\ P_2$ are the momenta of the initial protons, $x_1,\ x_2$ is the momentum fraction of the partons in the hard scatter, $f_1,\ f_2$ are the PDFs for the partons, Q is the square root of the total

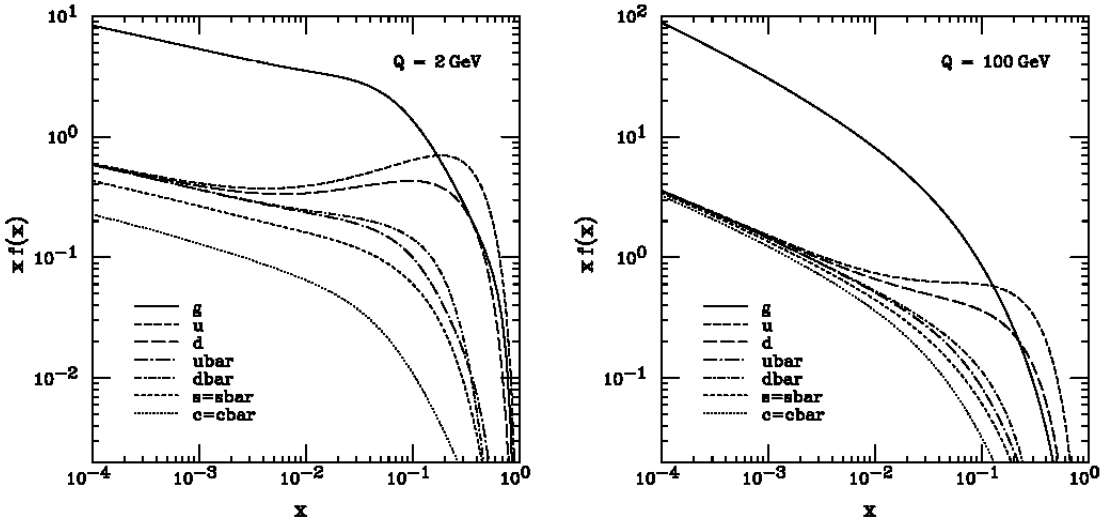

Figure 3.1: Parton Distribution Functions from the CTEQ collaboration for two values of interaction scale, Q. The horizontal axis is the fraction of the total proton momentum carried by the parton, x. The vertical axis shows the product of the parton momentum fraction and the PDF.

momentum transfered between initial state partons in the interaction, σ_{ij} is the momentum specific cross section of the hard scatter between partons q_i and q_j, and the sum is taken over all partons.

$$\sigma(P_1, P_2) = \Sigma_{i,j} \int f_1(x_1, Q^2) f_2(x_2, Q^2) \times \sigma_{ij}(x_1, x_2, Q^2) dx_1 dx_2 dQ^2 \tag{3.1}$$

Figure 3.1 contains the PDFs from the CTEQ collaboration at two values of Q. As Q increases, a larger fraction of the momentum is carried by the sea quarks and the gluons. This contributes to the difference in dominant production mechanisms for heavy particles at the LHC compared to Fermilab's Tevatron where the beam energy is lower.

3.2 Event Simulation

The results of the collision at the center of the detector are recorded in millions of electronic channels from the various subdetectors as the particles from the collision interact with the matter of the detector. The simulation of these signals requires a detailed model of detector material and geometry, an intricate understanding of interaction within the material, and an efficient computational framework to accommodate the large number of particles produced. For CMS this is provided by GEANT4 [52].

The design model of GEANT4 is to provide a modular simulation toolkit that enables the user to easily configure the tools to meet a variety needs. The toolkit allows users to specify the size, geometry and material of detector components. It then steps particles through the detector, simulating the detector response based on multiple physical interaction approaches and implementations. The level of intricacy is configurable by the user to accommodate desired efficiency and accuracy.

GEANT4 was originally designed at CERN in the 1990s. After the initial production release in 1998, the GEANT4 collaboration was establish in 1999 with the mission to maintain and improve the toolkit and to provide user support.

In GEANT4 a particle is stepped through the geometry of the detector by a tracking process, interacting with the simulated detector through a series of processes. The types of processes considered include particle decay, hadronic physics, electromagnetic and optical processes such as scintillation and Cherenkov radiation, and the GEANT4 optimized process of transportation. All physical processes rele-

vant to a particle propose a "step", and the tracking algorithm chooses the processes that are appropriate and applies them, stepping the particle through the detector material in an iterative process. The tracking process is generic and does not depend on the particular particle.

In the geometric model of the detector some material may be specified by the user as "sensitive", the material that produces a signal to be read out. As the tracking process tracks particles hitting designated sensitive areas of the detector "hits" are created automatically. From a collection of hits a "digit" is created and added to other "digits" from the same event, or several events in the case of pile-up. The digitization process is not automatic. It must be invoked by the user, which allows flexibility over the number of events to be digitized together.

The detector model can be adjusted by the user to accurately represent current conditions in the detector with respect to malfunctioning hardware and detector noise. As the state of the detector changes the simulation can be adjusted to mimic the change to best understand the impact on user analysis.

After digitization the simulated data is in the same format as collision data coming from the detector, and can be passed from GEANT4 to the detector specific reconstruction software responsible for identifying particles and their physical properties, which is discussed in the following chapter.

Chapter 4

Event Reconstruction and Particle Identification

The CMS Software (CMSSW) is a framework and set of packages used to identify and reconstruct the physics information of an event from the digitized signals. The software is modular and highly configurable to allow analysis specific customization by the user. Reconstructed object information is stored in the ROOT file format [53], structured in a CMS specific Event Data Module format. The algorithms used to reconstruct objects used in this analysis are discussed here.

4.1 Electron Reconstruction

Two complementary algorithms are used to reconstruct electrons in CMSSW in order to optimize the energy resolution: an ECAL-driven algorithm for medium-energy electrons and a tracker-driven routine for low energy electrons [54]. Electrons with transverse momentum, p_T (projection of momentum onto the plane perpendicular to the beam axis) less than 5 GeV present a unique challenge for reconstruction due to the large fraction of energy lost to bremsstrahlung in the tracker material before showering in the ECAL. The tracker-driven method is optimized for these low energy electrons. The ECAL-driven method is optimized to reconstruct electrons with a p_T between 5-50 GeV, the typical range for electrons from W and Z boson decays. ECAL-driven electrons are used exclusively in this analysis, as electrons

from LQ decays at or above the current mass limit typically have p_T well above 5 GeV, and high momentum electrons can be poorly reconstructed with the tracker driven algorithm due to the small curvature of the track.

The reconstruction of electrons is broken into several steps: energy clustering to identify ECAL cells associated with the electron energy deposition, identification and matching of the track of the electron from signals in the tracker layers, and energy corrections determined from MC to adjust the measured energy toward the true particle energy [54].

4.1.1 ECAL Clustering

The path of the electron through the detector is curved due to the 3.8 T axial magnetic field. As the electron interacts with the dense material in the tracker it radiates photons along its direction of motion, which then deposit energy in ECAL in an arc in ϕ. The clustering algorithms in CMSSW are designed to identify and cluster the cells hit by the bremsstrahlung, then group associated clusters creating a "supercluster", in an attempt to recover the initial energy of the electron before it entered the tracker and radiated.

Two methods are used within CMSSW to recover the energy lost by the radiating photons [55] [56]. The "hybrid clustering method" creates clusters of crystals three to five crystals wide in η and contiguous in ϕ that are separated from other energy deposits by 3 crystal wide regions in η of less than 100 MeV. Clusters within a configurable ϕ window are considered to originate from a single electron and are

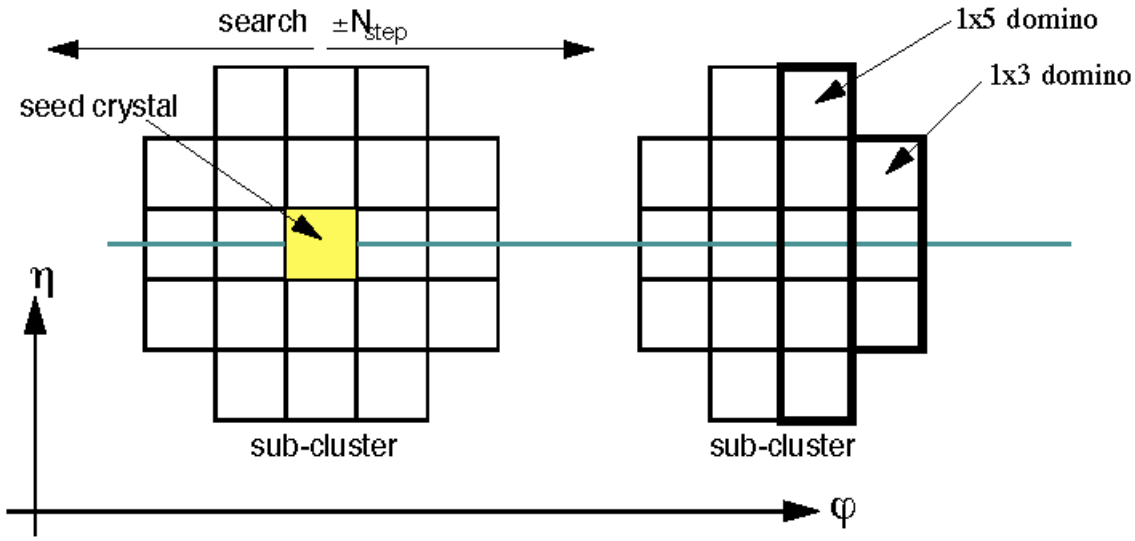

Figure 4.1: Hybrid Supercluster electron algorithm: Clusters of three to five crystals in η and contiguous in ϕ are grouped to form superclusters using the hybrid clustering algorithm [57].

collected into a supercluster, as shown in Fig. 4.1. Hybrid superclusters are used to seed the electrons in the barrel region where the algorithm can exploit the lateral shower shape and the simplicity of the barrel geometry to fix the η window of clustering.

Electron reconstruction in the endcap region uses the "island" clustering method, which uses the most energetic crystals as cluster seeds and searches for additional energetic crystals near each seed, as shown in Fig. 4.2. From a seed crystal the algorithm moves in both directions in ϕ, adding each crystal it encounters to the cluster if the energy of the crystal is smaller than the previously encountered crystal and is non-zero. If either of these conditions is not met the algorithm moves by one crystal in η on either side of the seed crystal, then repeats the clustering in ϕ.

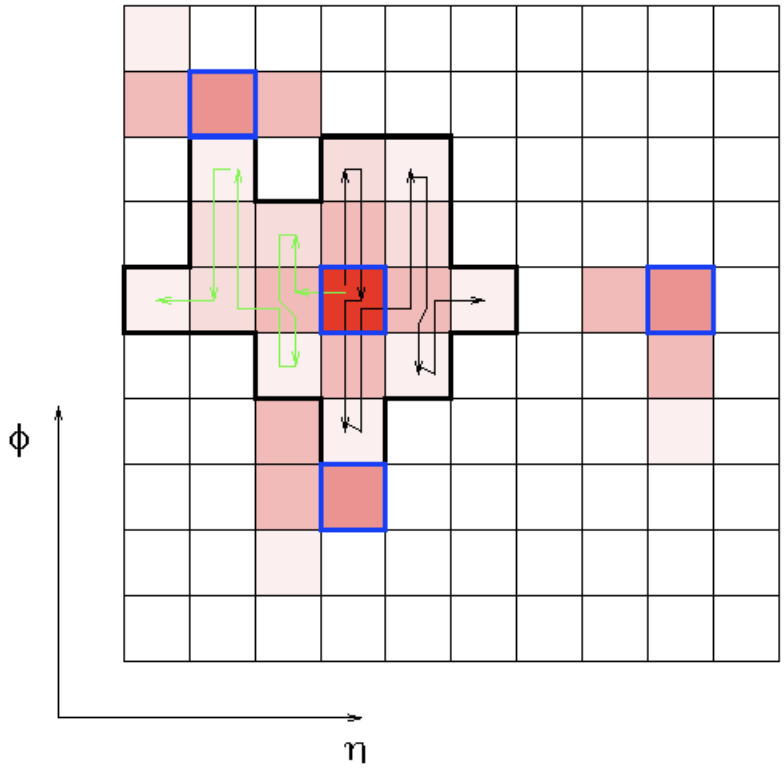

Figure 4.2: Island Supercluster electron algorithm: Rows of crystals with monotonically decreasing energy are clustered in both η and ϕ [58].

The clustering in the η direction continues according to the same conditions as the clustering in ϕ, adding crystals monotonically decreasing in energy to the cluster. Groups of clusters along a "ϕ road" are grouped together to form superclusters.

In order to be considered as a seed for an ECAL driven electron a supercluster of either hybrid or island type must have a transverse energy (E_T) of at least 4.0 GeV, and the ratio of energy in the HCAL to that in the ECAL in a cone of radius $\Delta R \equiv \sqrt{\Delta\eta^2 + \Delta\phi^2} = 0.15$ centered at the energy-weighted mean location of the crystals in the supercluster must be less than 0.15.

4.1.2 Track Reconstruction and Matching

Information from the tracker is used to identify a track and match it spatially to a supercluster of energy in ECAL. The track search begins with the "seed generator" component, which creates seeds consisting of two hits in the pixel detector (Section 2.2.1), pointing to a location consistent with the beam crossing spot. In order to reduce the number of possible seeds considered for track extrapolation a supercluster-driven pixel seed finding algorithm has been developed. The algorithm first calculates the energy-weighted location of the electron and associated bremsstrahlung photons. This is the impact point that would have been measured had the electron not radiated. Using this energy-weighted location in the ECAL, trajectories for both electron charge hypotheses are projected backwards through the tracker. A window in ϕ and z is considered around the intersection of this trajectory with the innermost layer of the pixel detector. If a hit is found in this window a new vertex hypothesis is calculated using the supercluster location and the pixel hit, and a second hit in the second pixel layer is searched for within a window along a new trajectory. If no hit is found in the initial window of the first pixel layer a first hit is searched for in the second pixel layer [59].

Once a track seed and a supercluster are identified, the "track builder" software component uses a Gaussian Sum Filter technique [60] to combine information from multiple tracker layers into a smooth curve. This method attempts to fit a smooth curve to a set of data points by defining the curve as a sum of gaussians with independent mean, amplitude and rms. The goal of the technique is to find

the minimum number of gaussians that can be used to describe a curve within a prescribed accuracy.

The track reconstruction is abandoned if no hit is found in two consecutive layers near the projected track. In order to be considered matched to an ECAL supercluster, the distance between the supercluster and the projection of the track intersection with the ECAL inner surface must be less than 0.02 in η and 0.15 in ϕ. If the track building procedure is successful the track parameters are determined based on the point of closest approach to the generated vertex.

4.1.3 Electron Energy Corrections and Uncertainties

The calorimeter-measured energy from electrons and bremsstrahlung photons is not always an accurate measure of the initial energy of the electron. This is due to energy loss in the material of the Tracker, and because the energy is not always well contained in the reconstructed supercluster due to the difficulty of identifying and clustering crystals correctly. This results in a generally smaller reconstructed energy than the true initial energy of the electron. The fractional containment of the energy within the supercluster can be estimated as a function of the number of crystals contained in the seed cluster, and the reconstructed supercluster energy can be adjusted accordingly [61]. MC studies show that as the number of crystals contained in the seed cluster increases as the supercluster energy approaches the generator level electron energy. A function is fit to the MC distribution of the ratio of supercluster energy to generated electron energy as a function of the number of

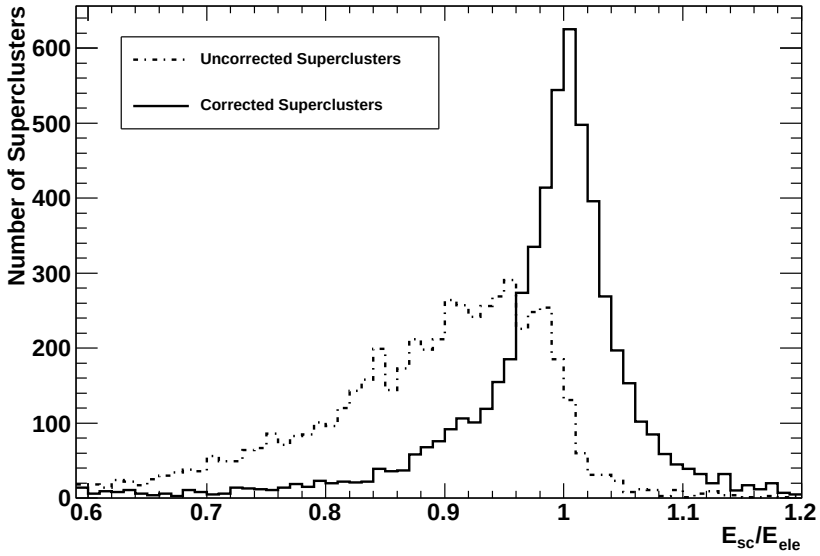

Figure 4.3: The ratio of raw supercluster energy to generator level electron energy and corrected supercluster energy to generated electron energy in MC events.

crystals in the seed cluster in order to determine the energy corrections.

Figure 4.3 shows the ratio of the reconstructed supercluster energy to the generated true electron energy before and after the corrections for electrons in the endcap region in MC Z boson events. After the corrections are applied the distribution is centered at one and the distribution is narrower. An estimate on the uncertainty associated with the electron energy measurement is achieved by comparing the location of the mass peak in W and Z boson events in data to the currently accepted empirical values of the boson masses [62]. Early data provides an estimate of less than 1% in the barrel and approximately 3% in the endcap for this uncertainty.

4.1.4 ECAL Anomalous Noise Cleaning

Isolated high energy deposits have been observed in the barrel region of ECAL at a rate of approximately 1 in 10^3 minimum bias events, corresponding to a noise probability of 1.6×10^{-8} per crystal per minimum bias event. The rate of these anomalous signals scales linearly with instantaneous luminosity. At this time these are believed to be caused by neutrons scattering protons out of the epoxy on the face of the APD (Section 2.2.2). The proton is a highly ionizing particle that triggers a large signal in the sensitive material of the APD [63]. The anomalous signals are characterized by a large energy deposit in a single crystal with little or no energy deposited in the surrounding crystals, and by a unique timing signature in the readout of the APDs. The energy of such signals ranges from GeV up to of order TeV.

Figure 4.4 shows the comparison between the arrival time of the reconstructed hit and the ratio of energy in the 4 crystals bordering the signal crystal to the energy in the signal crystal (E4/E1). The anomalous hits tend to have more than 95% of the energy isolated in one crystal (1- E4/E1>0.95), and to arrive earlier than signals from true EM objects. The reconstructed energy of each crystal incorporates an average offset subtraction, allowing for negative energy crystals. Two algorithms have been developed to minimize the effect of these anomalous signals on the data, one algorithm based on the topology of the energy deposit and the other based on the time distribution of the signal. These algorithms are implemented in the default reconstruction software to remove such signals from the collections of physics objects.

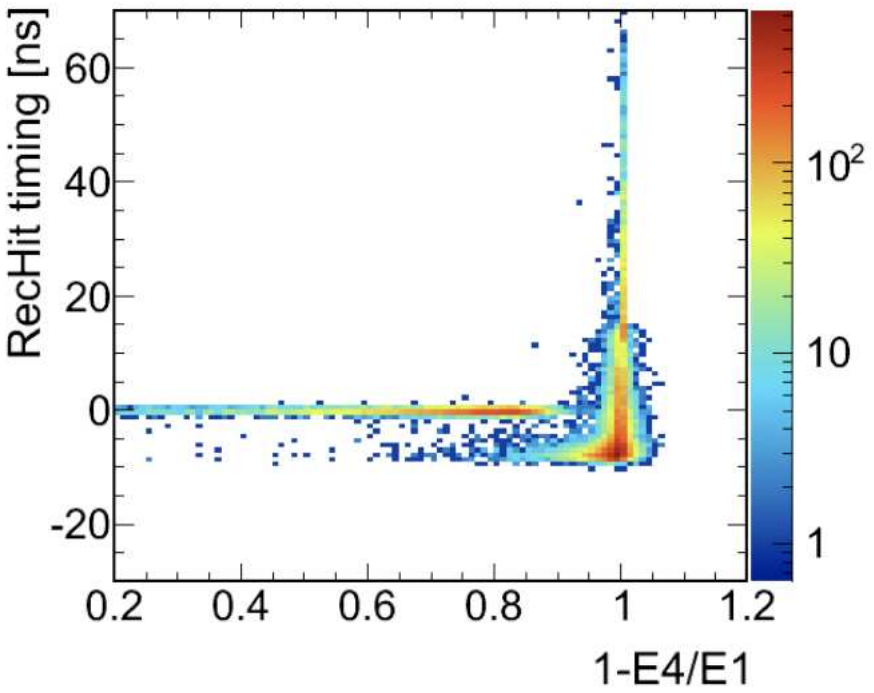

Figure 4.4: Comparison of adjusted arrival time of the reconstructed hit in the ECAL to the isolation of the signal [64]. The data outside the narrow band at 0 ns in RecHit timing tend to correspond to isolated, anomalous signals.

4.2 Jet Reconstruction

Hadronic jets, containing large numbers of both charged and neutral particles, register signals in the inner tracker, ECAL and HCAL. Three types of reconstructed jets are available in CMSSW based on the objects used to identify the jets: Calorimeter jets (CaloJets), which rely solely on information from the calorimeters; Jet-Plus-Tracks (JPTJets) jets, which are calorimeter jets with corrected energy based on the tracks originating from the jet production vertex; and Particle Flow (PFJets), which use individual reconstructed particles to determine the jet properties. This analysis uses exclusively CaloJets for historical reasons, the other two algorithms being relatively new when the analysis was started.

4.2.1 Jet-Finding Algorithm

Jet properties vary based on initial parton momentum, parton flavor, and statistical fluctuations within the shower. Multiple algorithms to identify jets and accurately cluster energy deposits have been studied by the CMS Jet-ID group. Three calorimeter jet algorithms are officially supported in CMSSW: Iterative Cone (iCone) [65]; Seedless Infrared Safe Cone (SISCone) [65]; and anti-k_t [66]. The iCone algorithm has a short and predictable execution time, but uses a fixed cone radius to calculate jets which does not allow for different size or shaped jets in the case of overlap. Jets calculated with the SISCone algorithm have a wide variety of shapes, allowing distinction between overlapping jets from nearby particles. However, soft (low energy) particles may deform the shape of the jet significantly. Anti-k_t jets

that are isolated have very regularly shaped boundaries, and overlapping jets are well differentiated. The Jet-ID group has recommended that all general analyses use anti-k$_t$ jets, and this prescription is followed in this analysis.

The anti-k$_t$ jet algorithm starts with energetic calorimeter towers as seeds for jets, then attempts to cluster nearby energy deposits coming from the same shower. Given a seed tower i, the algorithm considers all other towers j, by calculating a weighted metric between i and j, as shown in Equation 4.1, where k_{ti} (k_{tj}) is the transverse momentum (or transverse energy in the case of calorimeter cells) of tower i (j). R is a user configurable parameter affecting the jet cone size. In CMSSW jets formed by the anti-k$_t$ algorithm with R = 0.5 and 0.7 are available. Δ_{ij} is the distance between the two towers i and j defined in Equation 4.2, where η_i is the pseudorapidity (Section 2.2) and ϕ_i the azimuthal angle. If d_{ij} is less than d_{iB} (Equation 4.3), j is clustered with i to form a jet and j is removed from the list of seed towers.

$$d_{ij} = min(1/k_{ti}^2, 1/k_{tj}^2)\frac{\Delta_{ij}^2}{R^2} \tag{4.1}$$

$$\Delta_{ij}^2 = (\eta_i - \eta_j)^2 + (\phi_i - \phi_j)^2 \tag{4.2}$$

$$d_{iB} = 1/k_{ti}^2 \tag{4.3}$$

To understand the general characteristics of this algorithm, consider two calorimeter cells, i and j, separated by a distance Δ_{ij}. If $k_{ti} >> k_{tj}$, the d_{ij} for this pair

will be small, depending almost entirely on the cell with the larger energy, while if k_{ti} and k_{tj} are both small, d_{ij} will be much larger. Therefore low energy cells in the vicinity of a high energy cell will be clustered with the high energy cells rather than with each other. Similarly, the addition of a low energy cell within a distance of 2R to a high energy cell will be clustered with the higher energy cell, not into a soft jet.

This is of concern due to possible divergencies in QCD calculations resulting from infrared and collinear radiation (IRC). The mechanism is similar to that seen in QED where soft collinear photons cancel divergencies due to internal loops and are mitigated via cutoffs applied to both experimental data and MC. In perturbative QCD calculations, soft gluon emission (infrared) and collinear splitting both lead to infinities that cancel each other in the total cross section. In algorithms that are not IRC safe soft emission and collinear splitting can lead to different jet multiplicities, preventing the infinities from canceling out. In the anti-k_t algorithm the cells resulting in soft radiation or collinear splitting will be clustered into the same jet, leaving the algorithm IRC safe.

4.2.2 Jet Energy Scale Corrections and Uncertainties

The energy reconstructed in the jet can differ from that of the original hadronizing particle for a variety of reasons. In this analysis we correct for two sources of this discrepancy: the non-linear response of the detector with respect to energy, and the non-uniformity of the detector material in η, including variations in the number of interaction lengths and gaps in instrumented material leading to dead

areas. The raw energy calculated by the clustering of calorimeter cells is corrected as a function of the measured p_T and the η of the center of the jet. The corrections are derived from MC studies, comparing the energy of the jet at generator level to the reconstructed energy in the detector [67]. Figure 4.5 (a) shows the jet response ($p_T^{CaloJet}/p_T^{Gen\ Jet}$) as a function of η before and after the correction is applied. Figure 4.5 (b) shows the jet correction factor ($p_T^{Gen\ Jet}/p_T^{CaloJet}$) as a function of p_T of the raw calorimeter jet.

Residual energy corrections are applied to account for electronics noise and excess energy due to signals left over from previous bunch crossings (pile-up). These are calculated by identifying events from W boson decays and constraining the reconstructed mass of the W boson to agree with previously well measured results. The residual energy corrections are applied in this analysis.

The uncertainty on the measurement of the jet energy is a crucial systematic uncertainty in any analysis involving jets. There are several methods to estimate the magnitude of these uncertainties [68]. One of the most direct ways is to compare the p_T spectra of jets in data and in MC simulation. In early data taking at CMS this is shown to be within the conservative estimate of 10% adopted by pre- and early-data analyses.

4.2.3 HCAL Anomalous Noise Cleaning

High energy signals have been observed in the HCAL even in the absence of proton beams through CMS. These are attributed to a discharge in single HPDs

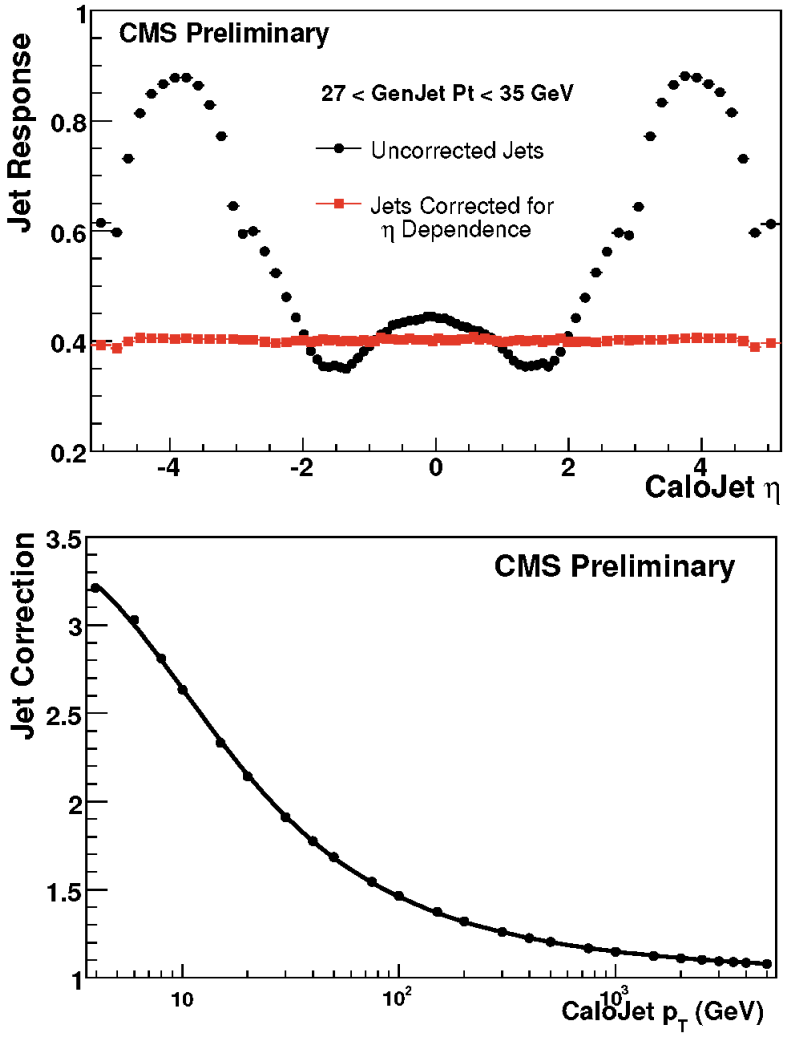

Figure 4.5: Top: Jet response as a function of jet η. Bottom: Jet correction factor as a function of jet p_T. Both are from MC studies [69].

(Sec. 2.2.3) and manifest as energy in several channels along η within a single ϕ slice, corresponding to channels sharing the same HPD, and are estimated to affect approximately 1 in 10^5 collision events. At this time these signals are believed to be due to charge accumulation on the HPD that occasionally discharges rapidly along the side walls of the tube [70]. Occasionally noise is observed that effects all 4 HPDs in a single readout box (RBX), causing a characteristic energy signal along η in 4 consecutive ϕ rows. The exact source of this noise is not currently understood. The timing structure of these noise events is also significantly different from that of collision events.

A filter module is run on the data after the standard reconstruction to reject events containing either HPD discharges or RBX noise [70]. The filter rejects events based on the energy distribution of signals in single HPDs and multiple HPDs sharing a single readout box, as well as the timing information for each signal.

Chapter 5

Analysis

5.1 Data and MC Samples

Data used in this analysis was collected between March 20 and October 30, 2010 comprising a total integrated luminosity of 34.7 pb^{-1}. The run numbers for the data range from 131511 to 149442, although not all runs within this range are included. The instantaneous luminosity during this period increased from 4×10^{28} $cm^{-2}s^{-1}$ to 1×10^{32} $cm^{-2}s^{-1}$ (100 events per μb cross section per second). The center-of-mass energy of the colliding beams was 7 TeV. Data are included in this analysis only if certified by a central CMS group responsible for evaluating the condition of all sub-detectors during the period of data collection. In addition, a reconstructed primary vertex is required within 24 cm in the z direction of the beam crossing point and a radius of 2 cm of the beam axis [72], and the fraction of tracks classified as "high purity" (passing tight requirements on the normalized χ^2 and number of hits in the track) must be larger than 25% in all events in order to reject events due to protons scraping the beam pipe rather than proton-proton collisions. A list of the CMS-specific dataset names is provided in Appendix B.

The data are compared to Monte Carlo (MC) samples of leptoquark (LQ) signal and several standard model (SM) processes that are expected to produce events similar to those from LQ decays. All samples were produced by the CMS production

team during 2010. LQ signal samples, summarized in Tab. 5.1, were produced using the PYTHIA event generator with CTEQ6L1 PDF sets, with detector simulation provided by the GEANT4 simulation tool kit. μ in Tab. 5.1 refers to the choice of factorization and renormalization scale for the cross section calculation.

LQ mass (GeV)	Equivalent Lumi. Generated(pb^{-1})	σ_{NLO} (pb)			δ_σ (pb) due to PDF unc.
		$\mu = M_{LQ}$	$\mu = M_{LQ}/2$	$\mu = 2M_{LQ}$	
300	4.13×10^4	1.21	1.37 (+13%)	1.04 (-14%)	0.16 (±13%)
320	6.07×10^4	0.82	0.93 (+13%)	0.71 (-14%)	0.11 (±14%)
340	8.77×10^4	0.57	0.64 (+13%)	0.49 (-14%)	0.08 (±15%)
370	1.48×10^5	0.34	0.38 (+13%)	0.29 (-14%)	0.05 (±15%)
400	2.38×10^5	0.21	0.23 (+13%)	0.18 (-14%)	0.04 (±17%)

Table 5.1: LQ MC samples used in this analysis with the theoretical cross section and uncertainty due to variation in factorization and renormalization scale(μ), and choice of PDF[71]. MC samples of 50,000 events were generated at each LQ mass point.

The signature of events containing first generation LQs at LHC energies is an energetic electron, an energetic positron and two energetic hadron jets (Figure 1.4). MC samples of SM processes with similar signatures are used to estimate the contribution to the selected events from non-signal processes. The MC background samples used for this analysis are listed below:

- $t\bar{t}$ + jets events, generated using MADGRAPH, including all allowed SM decay channels.

- Z/$\gamma*$ + N jets events (with N_{jet} $\leq$5), generated using ALPGEN, in four bins of $\hat{p}_T$ (the component of the total momentum transverse to the beam axis transfered in the collision,) from 0 to 1600 GeV, Z decaying into leptons (e, μ, τ).

- W + N jets events (with N_{jet} $\leq$5), generated using ALPGEN, in four bins of $\hat{p}_T$ from 0 to 1600 GeV, W decaying into leptons (e, μ, τ).

- VV events ($VV = WW$, WZ or ZZ), generated with PYTHIA, including all allowed SM W and Z decay channels.

- Single top events, generated with MADGRAPH , including all allowed SM top decay channels.

- γ + jets events, generated with MADGRAPH, in three bins of H_T (the linear sum of the p_T of final state objects) starting from 40 GeV.

5.2 Event Selection

The analysis strategy employed selects events with two high energy leptons and two high energy jets and imposes requirements on kinematic variables to reduce the number of SM process events selected. In this analysis both leptons are treated as electrons, as no distinction is made in the selection of events based on the charge of the lepton, The term "electron" is understood to refer to the lightest SM charged lepton, regardless of the charge. The dominant SM background processes contain two opposite sign leptons just as the signal does, leading to no significant advantage

to charge discrimination.

Event selection criteria are set that are optimized using MC to reduce the number of SM background and detector noise events selected, without sacrificing a significant fraction of signal events. Events passing the selection criteria in the data are counted and compared to the predicted number of such events from SM processes. Strict quality requirements on the electrons and jets reduce the contamination due to detector noise and SM events with fake electrons. Constraints on kinematic variables effectively reduce the number of SM background events with real jets and electrons.

5.2.1 Trigger

Events are filtered based on HLT results (Section 2.2.6) into "Primary Datasets" (PDs) that are made available to the user. This analysis uses the EGamma and Electron PD. The EGamma PD contains events passing all photon and electron triggers for data taken with an instantaneous luminosity less than 2×10^{31} cm^{-2}s^{-1}, at which point the data volume became large enough that smaller categories were warranted. Subsequent EGamma data are divided into an Electron PD containing all events passing electron triggers (used here for selection of signal events and estimation of background events with real electrons), and a Photon PD (used here to estimate the background contribution from events with fake electrons). The trigger tables used to filter the Electron and EGamma PDs for instantaneous luminosities greater than 10^{30} cm^{-2}s^{-1} are listed in Appendix D. The EGamma and Electron PDs contain a

total of 70.3 million events.

The minimum trigger requirements for the PDs are looser in transverse energy (E_T) and object identification (ID) criteria than those imposed on the electrons in the analysis selection criteria. No additional HLT requirement is imposed. Table 5.2 lists the E_T thresholds for the lowest E_T trigger contained in the PD with no prescale factor, the range of run numbers over which it was implemented, and the criteria for passing the trigger. The ID criteria used by the HLT are defined as follows:

- H/E: the ratio of the hadronic energy to the electromagnetic energy in the calorimeters within a radius of R $\equiv \sqrt{\Delta\eta^2 + \Delta\phi^2} = 0.15$ of the supercluster.

- $\sigma_{i\eta i\eta}$: the weighted second moment in η of the electron shower, used to help identify fake electrons from hadron jets:

$$\sigma_{i\eta i\eta} = \frac{\sum_k^{5x5} w_k \times (\imath_\eta^k - \bar{\imath}_\eta)^2}{\sum_k^{5x5} w_k} \quad ,$$

  where $\imath_\eta^k$ is the index of the η position of the k^{th} crystal in a 5x5 matrix of crystals centered on the seed crystal of the cluster associated with the electron, $\bar{\imath}_\eta$ is the energy weighted mean index of the η position of the 5x5 block, and w_k is a weight given to each crystal defined by

$$w_k = \max[0,\ 4.2 + \ln(\frac{E_k}{E_{5\times5}})] \quad ,$$

  where E_k is the energy of the k^{th} crystal and E_{5x5} is the total energy deposited in the 5x5 block. The weight varies logarithmically to reduce the effect of fluctuations and detector noise. The values for the endcap are corrected for

the different crystal size with respect to the barrel region. This variable differs from $\sigma_{\eta\eta}$ by the use of crystal index rather than η value directly.

- $\Delta\eta^{trk-SC}$ and $\Delta\phi^{trk-SC}$: the difference in η and ϕ between the track position extrapolated from the inner layer tracker to the ECAL surface and the location of the supercluster.

Events passing the triggers listed in Table 5.2 must also first pass a L1 trigger. The L1 for the lowest E_T triggers requires at least 5 GeV of E_T in the ECAL for runs with run number in the range 131511-147145, and 8 GeV of E_T in the ECAL for all subsequent runs.

HLT E_T threshold	Run Range Implemented	ID Criteria
10 GeV	132440-141949	H/E < 0.15
15 GeV	141950-146897	$\delta\eta^{trk-SC} < 0.01$, $\delta\phi^{trk-SC} < 0.08$ $\sigma_{i\eta i\eta} < 0.014$ (barrel), <0.035 (endcap) H/E < 0.15
17 GeV	146898-147145	$\delta\eta^{trk-SC} < 0.01$, $\delta\phi^{trk-SC} < 0.08$ $\sigma_{i\eta i\eta} < 0.014$ (barrel), <0.035 (endcap) H/E < 0.15
17 GeV	147146 -149442	$\delta\eta^{trk-SC} < 0.01$, $\delta\phi^{trk-SC} < 0.08$ $\sigma_{i\eta i\eta} < 0.012$ (barrel), <0.032 (endcap) H/E < 0.1

Table 5.2: HLT triggers used for the EGamma and Electron primary datasets.

5.2.2 Electron Candidate Criteria

Events are required to have two electrons with a maximum $|\eta|$ of 2.5 and a transverse momentum (p_T) of at least 30 GeV in order to minimize poorly reconstructed electrons with low energy, and those at or near the sub-detector boundaries. These cuts have little effect on the signal efficiency as the electrons from LQs at or above the current mass limit have a p_T spectrum peaked well above the cut of 30 GeV, as shown in Fig. 5.1 (a), and tend to be central, as shown in Fig. 5.1 (b).

The default electron collection present in the CMS reconstructed data (Sec. 4.1) contains loose ID constraints, allowing moderate contamination of the collection by fake electrons from jets. Further criteria have been developed by the High Energy Electron Pairs group (HEEP) within CMS to efficiently identify true electrons with high energy. Both electrons in candidate events are required to pass the HEEP criteria. These criteria consist of:

- H/E: The ratio of the hadronic energy to the electromagnetic energy in the calorimeters. See Sec.5.2.1 for details.

- $\sigma_{i\eta i\eta}$: The weighted second moment in η of the electron shower:

$$\sigma_{i\eta i\eta} = \frac{\sum_k^{5x5} w_k \times (\imath_\eta^k - \bar{\imath}_\eta)^2}{\sum_k^{5x5} w_k} \quad ,$$

  See Sec.5.2.1 for details.

- $\Delta\eta^{trk-SC}$ and $\Delta\phi^{trk-SC}$: The difference in η and ϕ between the track position extrapolated from the inner layer tracker to the ECAL surface and the location of the supercluster.

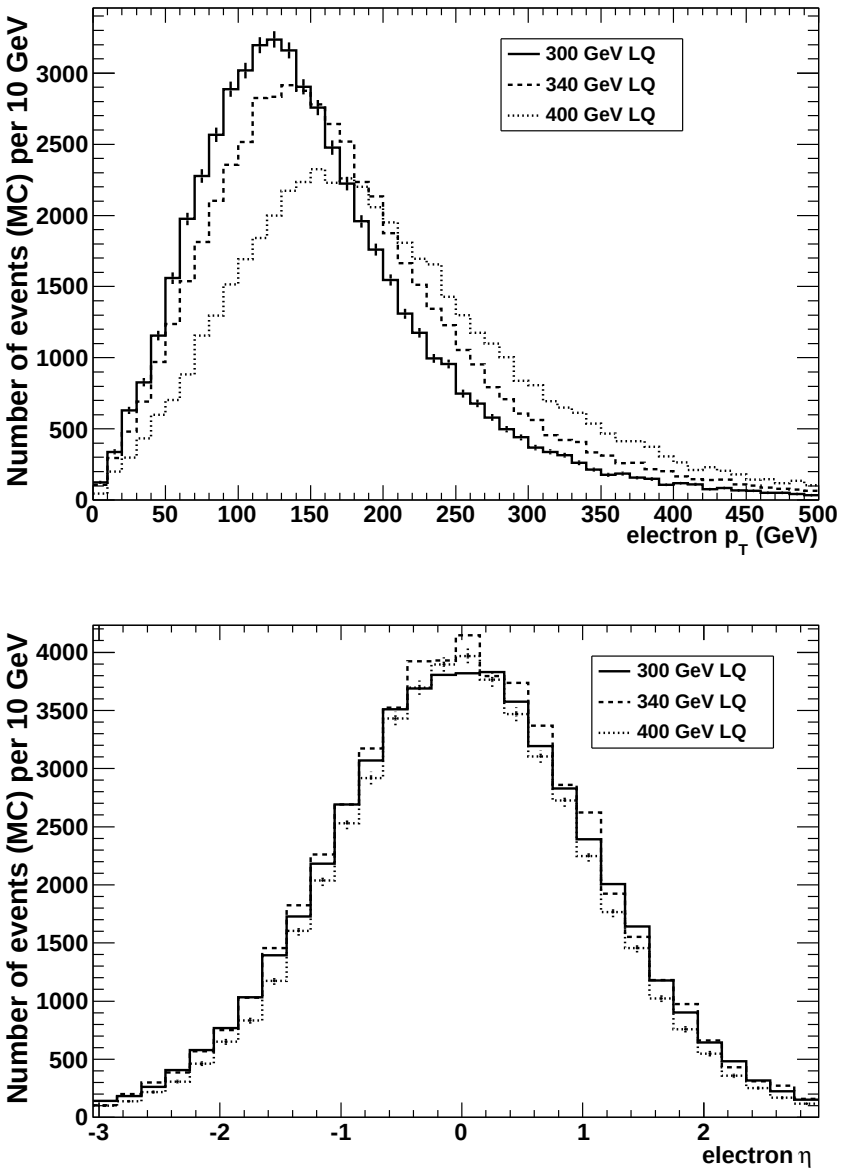

Figure 5.1: Distributions of p_T (top), and η (bottom) of generator level electrons from LQ decays in MC samples for three LQ mass hypotheses.

- Track isolation (Track iso): The sum of the p_T of tracks with p_T >0.7 GeV in the annulus with inner radius 0.04 and outer radius 0.3 centered at the supercluster. Contributing tracks must have z_0 (the minimum distance along the beam axis from the interaction point) within ±0.2 cm of z_0 of the electron track.

- Electromagnetic + Hadronic depth 1 isolation (EM+H1 iso): The electromagnetic energy of all the single channel energy deposits with $|E| > 0.08$ GeV (0.1 GeV in the endcap) in a cone of radius R < 0.3, centered on the electron's position in the calorimeter, excluding the energy deposits that make up the supercluster and those in an η strip of width of approximately 0.02 centered at the supercluster, plus the sum of all energy in the first scintillator depth of the hadronic channels within an annulus of inner radius 0.15 and outer radius 0.3 centered at the supercluster.

- Hadronic depth2 isolation (H2 iso) (endcap only): The sum of all energy in the hadronic channels in the second scintillator depth within an annulus of inner radius 0.15 and outer radius 0.3 centered at the supercluster.

- $E^{2\times5}/E^{5\times5}$: The ratio of energy in a 2×5 rectangle of crystals in ECAL to that in a square of 5×5 crystals, both centered at the supercluster.

The thresholds for the above criteria are listed in Table 5.3.

The efficiency of the HEEP criteria at identifying high energy electrons is calculated by the HEEP group using a "tag and probe" method on events from

Variable	Barrel Threshold	Endcap Threshold
H/E	< 0.05	< 0.05
$\sigma_{i\eta i\eta}$	n/a	< 0.03
$\Delta\eta^{trk-SC}$	< 0.005	< 0.007
$\Delta\phi^{trk-SC}$	< 0.09	< 0.09
Track iso	< 7.5	< 15
EM+H1 iso	$< 2 + 0.03 \times E_T$	< 2.5 if $E_T < 50$ else $< 2.5 + 0.03 \times (E_T - 50)$
H2 iso	n/a	< 0.5
E^{2x5}/E^{5x5}	>0.94 OR $E^{1x5}/E^{5x5} > 0.83$	n/a

Table 5.3: Criteria established by the High Energy Electron Pair (HEEP) group to identify high energy electrons, applied in addition to the standard reconstructed electron criteria.

Z boson decays. Events are selected containing two loose electrons with invariant mass close to the mass of the Z boson. One of the electrons is tagged by requiring it to be a HEEP electron. The other electron is probed to calculate the probability it passes the HEEP selection. This efficiency of the HEEP identification of a standard reconstructed electron is found to be 91.7±0.5% in the barrel, and 90.5±0.9% in the endcap [73].

5.2.3 Jet Candidate Criteria

Candidate events are also required to contain two jets with p_T greater than 30 GeV in order to avoid low energy jets that may be poorly calibrated, and an $|\eta|$ of less than 3.0 to avoid the forward region with high jet occupancy, as well as a larger rate of detector noise. Figure 5.2 shows the high p_T spectra and the mostly central η distribution of the jets from LQ decays at and above the DØ Collaboration mass limit. The peaks of the p_T spectra increase with the mass of the LQ as more mass energy is available for the daughter particles in the decay.

The jet reconstruction algorithm uses large clustered deposits of energy in the calorimeters to identify jets (Sec. 4.2.1). Since energetic electrons deposit the majority of their energy in the ECAL, they are also reconstructed as jets. These electron-jets are removed from the jet collection by comparing the set of HEEP electrons described in Sec. 5.2.2 to the jet collection and removing any jet within a radius of $\Delta\mathrm{R} = 0.3$ of a HEEP electron.

Jets are required to pass a set of loose ID criteria in an effort to distinguish detector noise from real jets originating from hadrons. The criteria are designed such that the signal is not isolated in one misfiring detector component by requiring a reasonable split between energy in the ECAL and HCAL. The jet ID criteria are:

- EMF (electromagnetic fraction) > 0.01 if $|\eta| < 2.6$: If the jet $|\eta|$ is less than 2.6, the fraction of the total jet energy contained in the ECAL (EMF) must be greater than 0.01. This removes nearly all jets that are due to detector noise in HB and HE and have no energy deposit in ECAL. The efficiency of this cut

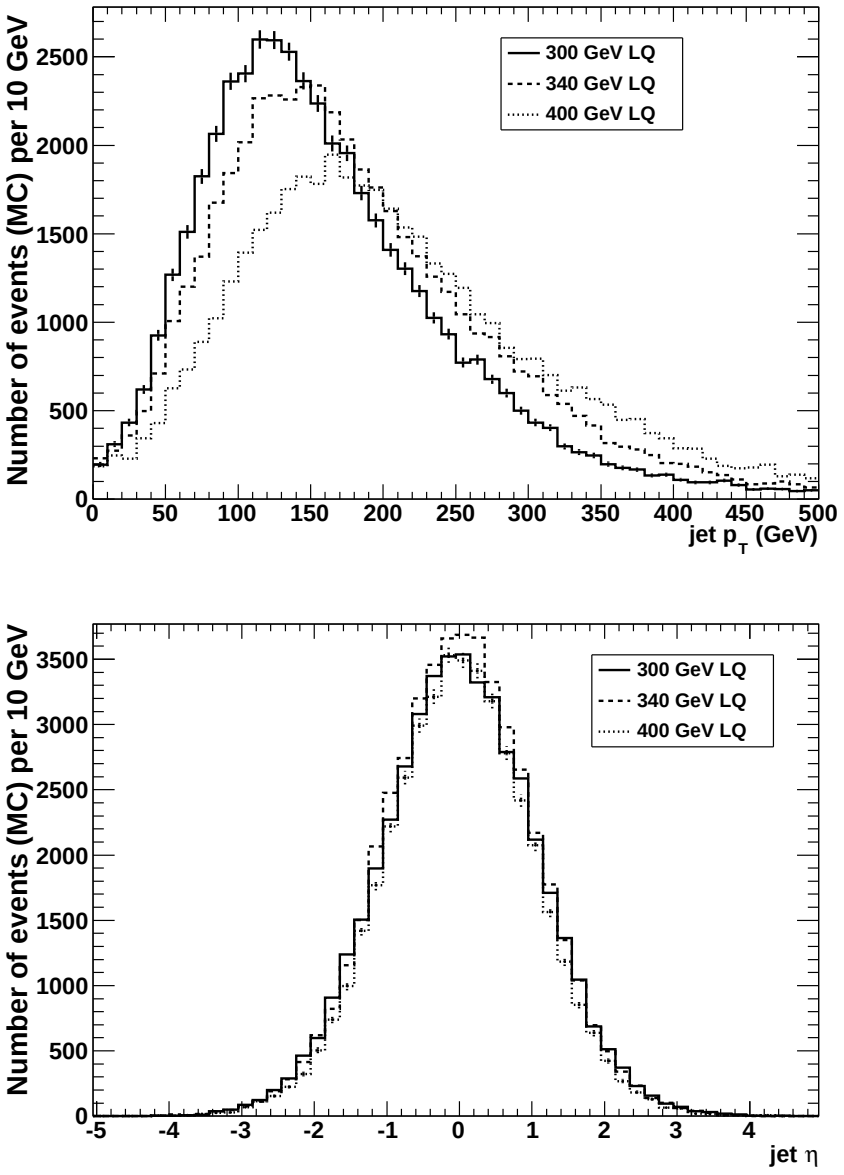

Figure 5.2: Distribution of p_T (top) and η (bottom) of generator level jets matched to quarks from LQ decays in MC samples for three LQ mass hypotheses.

in selecting physical jets was seen to be essentially 100% in a study including detector noise from data and jets from MC. There is no EMF requirement for jets with $2.6 < |\eta| < 3.25$. In this region the HE and HF overlap and the calculation of EMF is complicated due to the difference in measurement technique of the EM component of the jet between the two detectors.

- $N_{hits}^{90} > 1$: The number of calorimeter towers (combined ECAL and HCAL) containing 90 percent of the jet energy must be at least 2. This removes jets due to electrical discharges or noise in single towers.

- $f_{HPD} < 0.98$: The fraction of the jet energy contained in the HCAL HPD with the highest total energy in the jet must be less than 0.98. This significantly reduces fake jets due to HCAL detector noise (see Sec. 4.2.3).

These cuts are shown to be efficient at removing non-physical jets in data taken with no beams in the LHC when no physical jets are present [74].

5.2.4 Object Proximity

Two energetic objects hitting the detector in close proximity will overlap in the sensitive detector material, making it difficult to reconstruct either object properly. To avoid this problem, events are rejected in which either of the two most energetic jets are within a distance of R = 0.7 of the two most energetic electrons.

5.2.5 Electron Pair Invariant Mass

One of the dominant sources of SM background events passing the electron and jet criteria is the production of a Z boson or heavy photon ($\gamma*$) decaying to two electrons along with two jets from ISR or FSR. In order to reject Z events, the two electrons in the event are required to have an invariant mass greater than 125 GeV, well above the peak of the Z boson mass at 91 GeV, as can be seen in Figure 5.3. This cut has been optimized using a Bayesian approach to minimize the possible excluded cross section of LQ production in the absence of signal (Sec. 5.6). MC studies show this cut to be 92.3±0.1% efficient on events containing a 400 GeV LQ that pass the object selection criteria, and only 2.2±0.1% efficient on Z/$\gamma*$+jet events passing the object selection criteria.

5.2.6 Transverse Momentum Scalar Sum

Previous studies done in LQ searches by the DØ Collaboration [15] have investigated several discriminating variables and found the criterion with the largest discriminating power to be the scalar sum of the p_T of the two leading electrons and two leading jets, S_T, defined in Eq. 5.1.

$$S_T = p_{T\ ele1} + p_{T\ ele2} + p_{T\ jet1} + p_{T\ jet2} \tag{5.1}$$

This variable magnifies the difference between SM processes and LQ events in the individual object p_T spectra, which are shown in Fig. 5.4 for the two leading electrons in events passing the electron criteria only, and Fig. 5.5 for the two leading jets in events passing the electron and jet criteria and with an $M_{ee} > 50$ GeV.

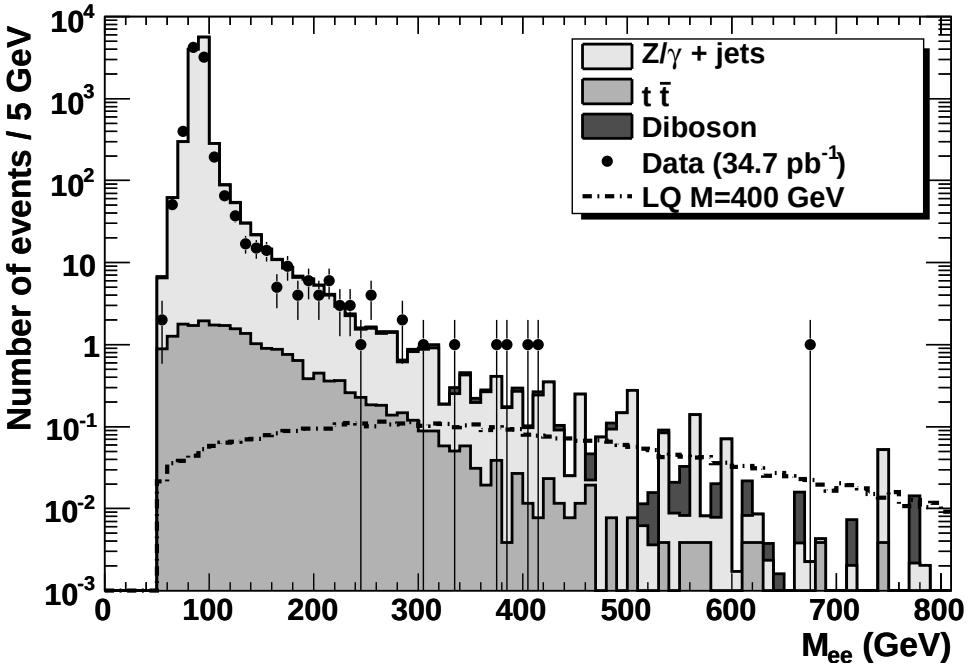

Figure 5.3: Invariant mass of the two electrons in events passing the electron object criteria. Only $M_{ee} > 50$ GeV is displayed in the histogram due to a cut of $M_{ee} > 40$ GeV in the MC sample used for Z/$\gamma*$+jets. Data (black dots) are seen to be in good agreement with the MC predictions (stacked histograms).

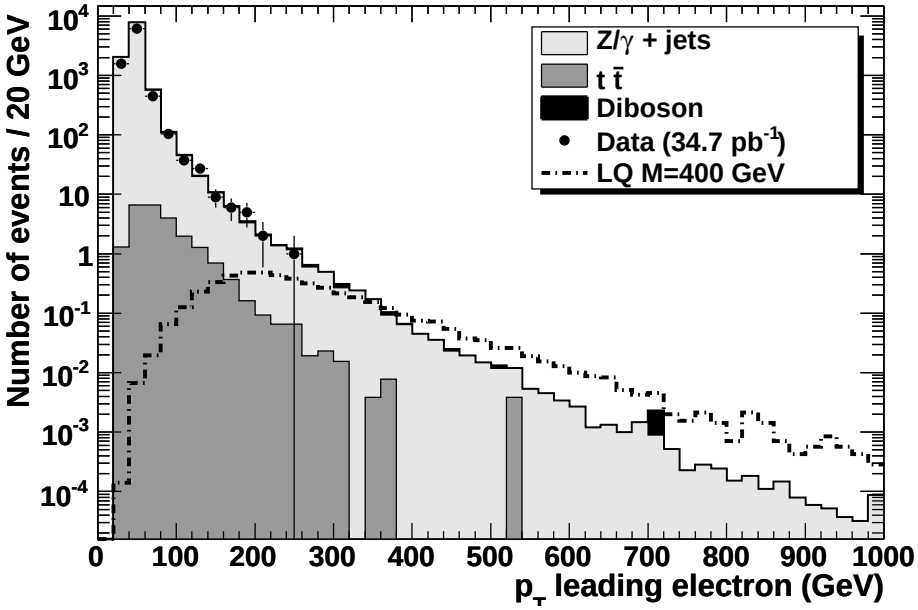

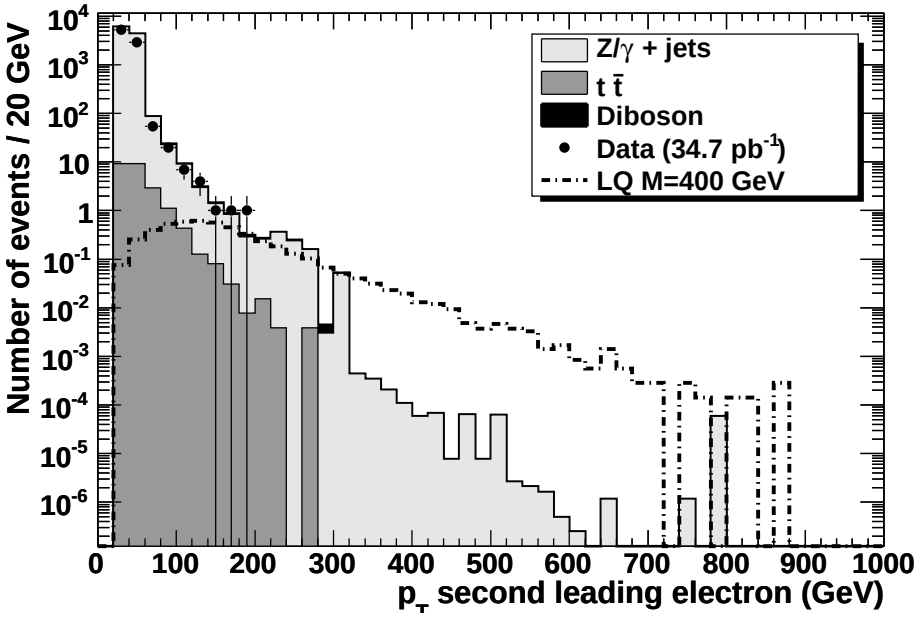

Figure 5.4: Distribution of the leading (top) and second leading (bottom) electron p_T for SM processes, LQ signal samples, and data. Data (black dots) is seen to have a good agreement with the MC predictions (combined histograms).

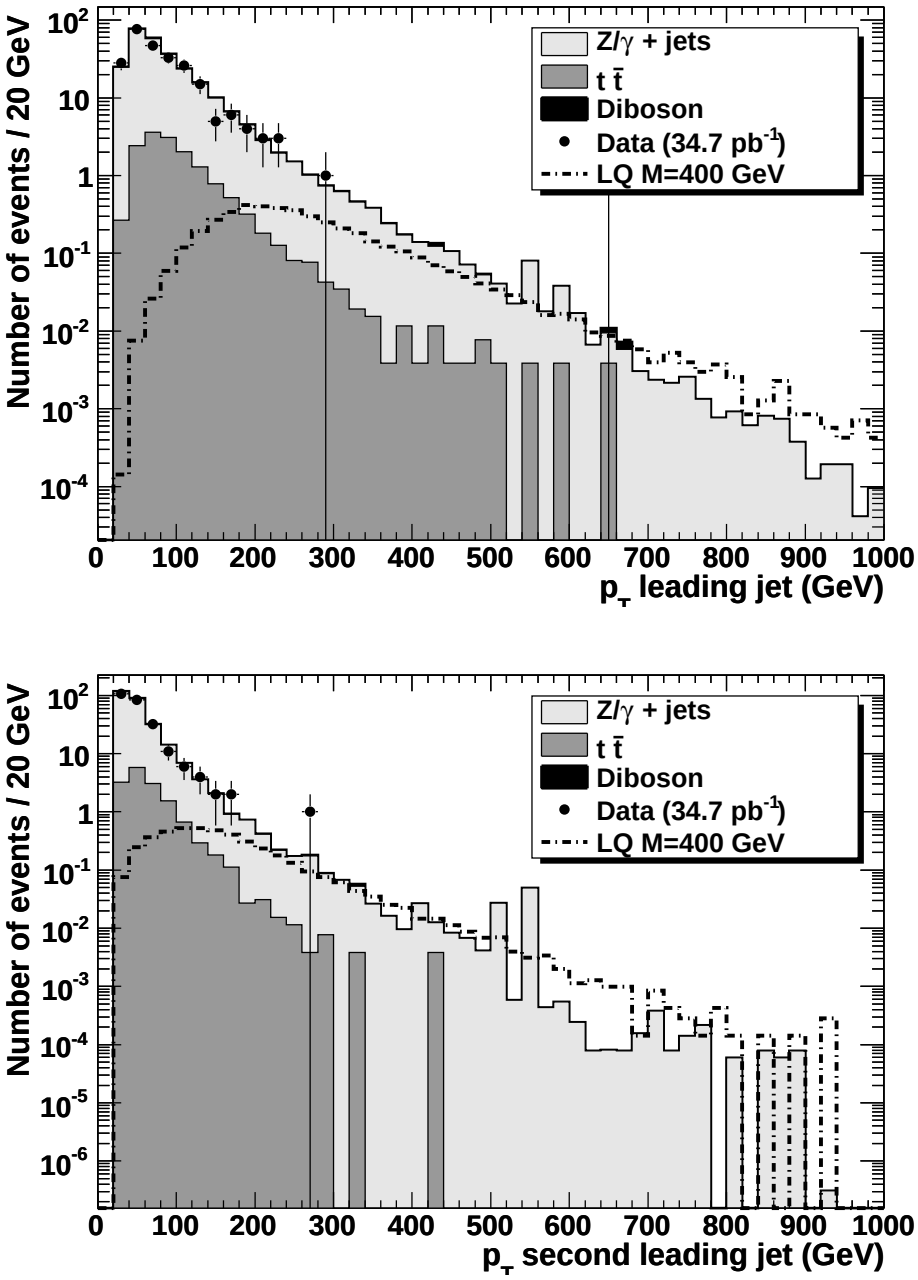

Figure 5.5: Distribution of the leading (top) and second leading (bottom) jet p_T for SM processes, LQ signal samples, and data. Data (black dots) is seen to have a good agreement with the MC predictions (combined histograms).

The threshold for this variable is optimized in this analysis to give the lowest possible cross section upper limit using the same Bayesian approach as that for the di-electron invariant mass threshold. Table 5.4 lists the optimized values of the S_T cut for various LQ mass hypotheses.

LQ Mass (GeV)	S_T Threshold (GeV)
300	470
320	490
340	510
370	540
400	560

Table 5.4: S_T threshold for various LQ masses.

Figure 5.6 shows the distribution of S_T for 400 GeV LQ events, as well as contributions from SM background with at least two HEEP electrons and two jets passing the jet criteria, and with di-electron invariant mass above 125 GeV.

5.2.7 Summary

Table 5.5 contains a summary of the event criteria, along with the total number of data events passing each cut. Only one data event passes all selection criteria. Similar tables showing the effect of each cut on MC signal events and the dominant SM background processes are provided in Appendix C.

An event display of the one remaining data event is shown in Fig. 5.7. The

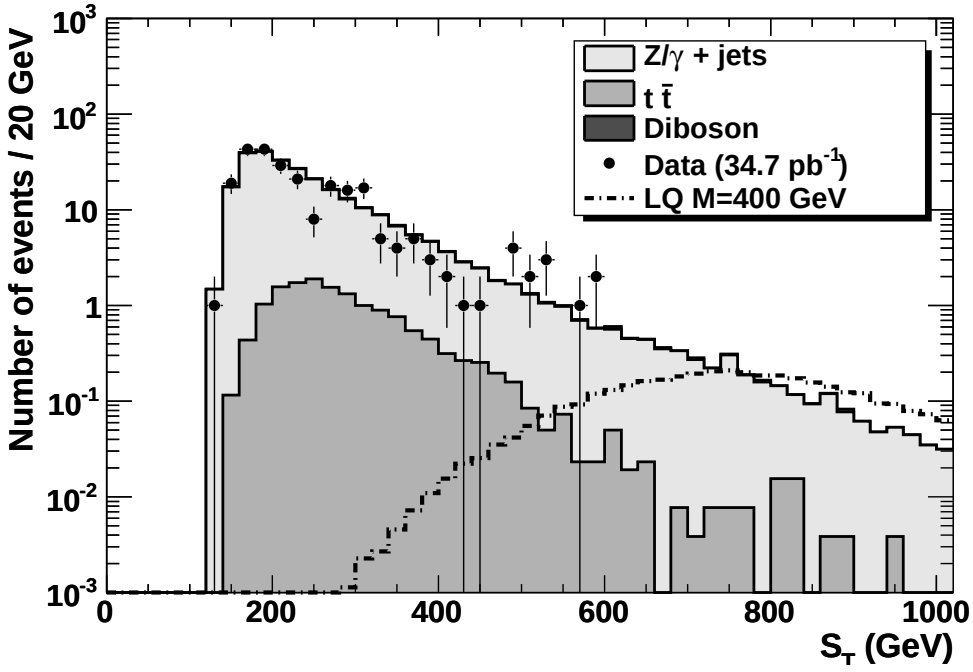

Figure 5.6: Distribution of S_T in events with a di-electron invariant mass larger than 125 GeV. Data (black dots) is seen to have a good agreement with the MC predictions (combined histograms).

Criteria	N_{events} Pass Data	Relative Efficiency	Total Efficiency wrt PD
Electron criteria	8.29×10^3	$(1.17 \pm 0.01) \times 10^{-4}$	$(1.17 \pm 0.01) \times 10^{-4}$
Jet criteria	2.75×10^2	$(3.32 \pm 0.20) \times 10^{-2}$	$(3.91 \pm 0.24) \times 10^{-6}$
$\Delta R(ele - jet) > 0.7$	2.55×10^2	$(9.27 \pm 0.83) \times 10^{-1}$	$(3.63 \pm 0.23) \times 10^{-6}$
$M_{ee} > 125$ GeV	9	$(3.53 \pm 1.20) \times 10^{-2}$	$(1.28 \pm 0.43) \times 10^{-7}$
$S_T > 470$ GeV	1	$(1.11 \pm 1.17) \times 10^{-1}$	$(1.42 \pm 1.42) \times 10^{-8}$
$S_T > 490$ GeV	1	1.00	$(1.42 \pm 1.42) \times 10^{-8}$
$S_T > 510$ GeV	1	1.00	$(1.42 \pm 1.42) \times 10^{-8}$
$S_T > 540$ GeV	1	1.00	$(1.42 \pm 1.42) \times 10^{-8}$
$S_T > 560$ GeV	1	1.00	$(1.42 \pm 1.42) \times 10^{-8}$

Table 5.5: Sequence of selection criteria and the number of data events passing each. Efficiency is quoted with respect to the primary dataset.

grey, three-dimensional cylindrical grid shows the surface of the inner detectors. The energy deposits in the calorimeters are shown as blocks along the outer surface of the grey grid. Reconstructed electrons and jets, as well as a single muon, are seen originating from the primary vertex.

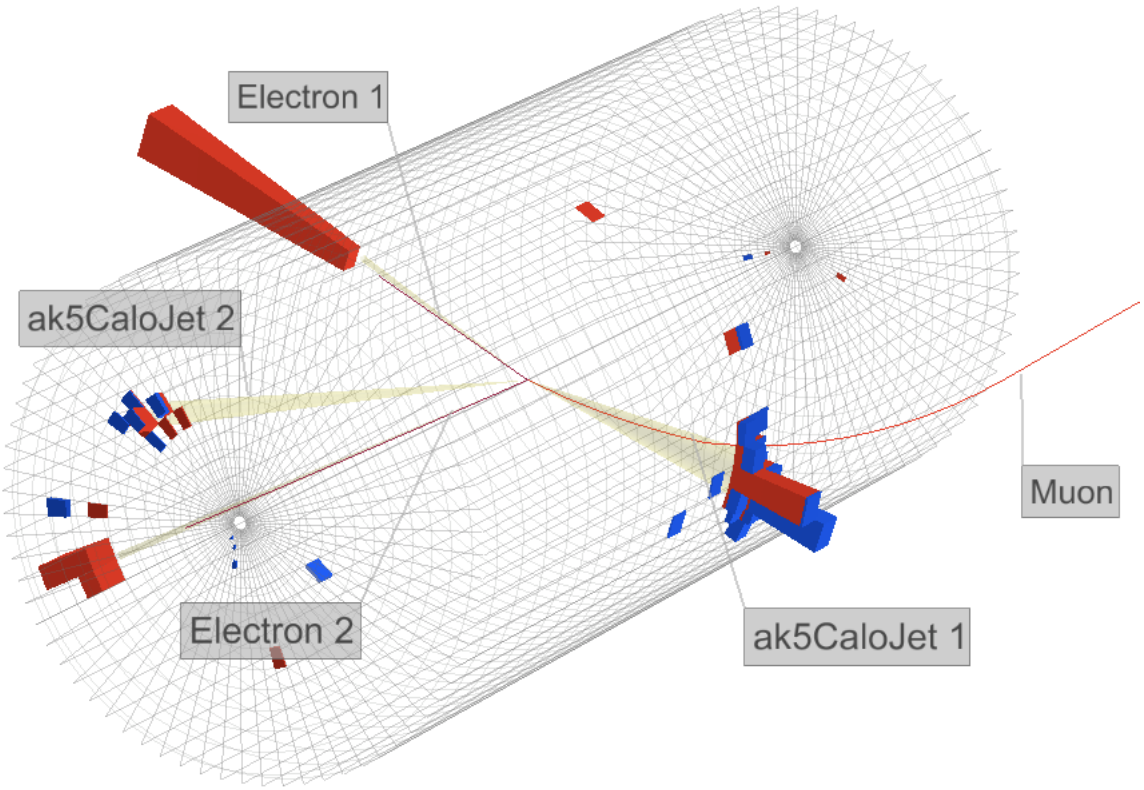

Figure 5.7: Three-dimensional representation of the reconstructed objects and calorimeter deposits for the single data event passing all selection criteria.

5.3 Estimation of Standard Model Contributions

5.3.1 Z/$\gamma*$ + Jets

The requirement that candidate events have a di-electron invariant mass above 125 GeV (Sec. 5.2.5) is highly effective at reducing the number of Z/$\gamma*$+jet events. The number of these background events remaining after the full selection criteria is estimated from MC. A scaling factor is applied in order to adjust the MC cross section such that the number of events in data and MC are in agreement in a sample enriched in Z/$\gamma*$+jet events. The scaling factor for the number of events passing all criteria is calculated by comparing data and MC in events near the Z boson mass peak, as shown in Eq. 5.2, where "purity" is the fractional purity of Z boson events at the mass peak as predicted by MC.

$$N^{Z/\gamma*}_{Final\ Selection} = N^{Z/\gamma*}_{MC\ Final\ Selection} \times \frac{N^{Z/\gamma*}_{Data\ Mass\ Peak} \times \text{purity}}{N^{Z/\gamma*}_{MC\ Mass\ Peak}} \tag{5.2}$$

Events are selected by requiring 2 HEEP electrons with $p_T > 30$ GeV with an invariant mass between 80 GeV and 100 GeV, two jets with $p_T > 30$ GeV, and an $S_T > 250$ GeV. Applying these requirements to MC samples from multiple SM processes results in a sample containing 97% Z events, with approximately 1.5% contamination each from $t\bar{t}$ and diboson events. The data contains 78 events with $80 < M_{ee} < 100$ GeV, while the MC prediction is 64.27 ± 0.90. This gives a scaling factor of 1.18 ± 0.13. It is not unexpected that this factor deviates from one since the MC does not model the Z boson events with two extra jets as well as those with

no extra jets. These jets come from initial state radiation, a process difficult to model well as discussed in Sec. 3.1.2. The relative uncertainty on the scaling factor, $0.13/1.18 = 11\%$ is taken as a systematic uncertainty on the size of the Z/$\gamma*$ +jets background. In all subsequent tables and histograms the rescaling factor is applied to the Z/$\gamma*$ +jets MC events.

5.3.2 Top Quark Pairs ($t\bar{t}$)

The only other source of a non-negligible contribution to the background from SM processes is the production of top/anti-top quark pairs ($t\bar{t}$), as shown in Fig. 5.8, where each top quark decays to a bottom quark and a W boson. The bottom quarks hadronize, and each W boson may decay either to a pair of quarks, or to a charged lepton and a neutrino. If both W bosons decay leptonically there are two jets in the event from the bottom quarks and two leptons in the events from the W bosons.

In order to estimate the contribution to the number of background events from $t\bar{t}$ decays, the MC prediction is scaled in a way similar to the method used to estimate the number of Z/$\gamma*$ +jets events. A control sample is selected using the knowledge that W bosons decay with nearly equal probability to electrons or muons. Events in which one of the W bosons decays to a muon creates a control sample from which a scale factor for the $t\bar{t}$ MC can be calculated.

Events are selected that have two jets and exactly one electron and one muon ("eμjj"). This sample is estimated to be approximately 95% pure top quark sample from MC studies [75], with the non-$t\bar{t}$ contamination derived mostly from di-boson

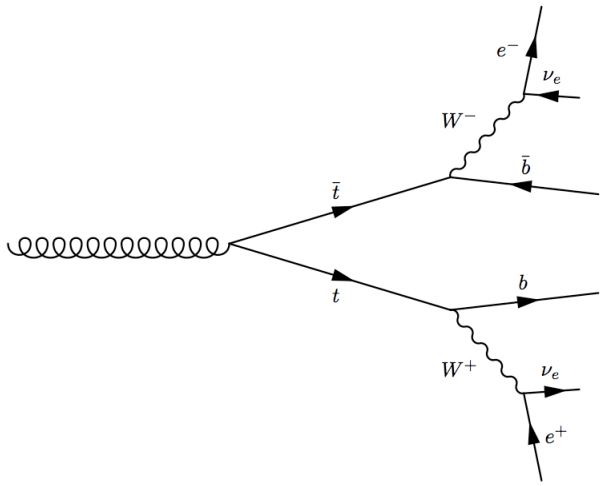

Figure 5.8: Leptonic decay of $t\bar{t}$ events. These events mimic the LQ signal events due to the two electrons from the W boson decays and the two jets from the b quarks.

events. The number of eμjj events in data is compared to that predicted from MC to produce a scale factor that can be applied to the MC prediction for eejj events, as shown in Eq. 5.3.

$$N^{t\bar{t}}_{eejj} = N^{t\bar{t}}_{MC\ eejj} \times \frac{N^{t\bar{t}}_{Data\ e\mu jj} \times \text{purity}}{N^{t\bar{t}}_{MC\ e\mu jj}} \tag{5.3}$$

The total number of eμjj events in the data is 25, compared to a MC prediction of 27.7 $\pm$ 0.3 events. This gives a scale factor of 0.86 $\pm$ 0.2. The MC prediction is left unscaled as this factor is consistent with 1. A systematic uncertainty on the size of the $t\bar{t}$ background is estimated using the statistical relative uncertainty on the size of the eμjj data sample, $1/\sqrt{25} = 20\%$.

5.3.3 QCD multi-jet background

The number of events with no true electrons in which two electrons are reconstructed is expected to be small. An estimate of this contribution is made by relaxing some of the requirements imposed on the electron candidates in order to create a sample dominated by multi-jet events (described later in this section), then applying a probability that the fake "electron" with relaxed requirements will pass the full electron selection criteria. The electron criteria which are removed to create a sample of fake electrons are: the matching of a track with the supercluster of energy in the ECAL, the shower shape variable $\sigma_{i\eta i\eta}$, and the hadronic isolation. Objects passing the new relaxed criteria are supercluster which pass the H/E and electromagnetic isolation thresholds only, as shown in Tab. 5.6.

Variable Name	Barrel Threshold	Endcap Threshold
H/E	< 0.05	< 0.05
Ecal Isolation (GeV)	$< 6 + 0.01 \times E_{TSC}$	$< 6 + 0.01 \times E_T$ if $E_T < 50$ GeV else: $< 6 + 0.01 \times (E_T - 50)$

Table 5.6: Isolation criteria for superclusters.

The probability for a fake "electron" to pass the HEEP selection ("fake rate") is estimated from the ratio $P(e|s) = N_e/N_s$, where N_e (N_s) is the total number of HEEP electrons (isolated superclusters). The set of events used to calculate the fake rate must pass the following criteria, designed to select a sample as enriched as possible in QCD di-jets events:

- at least one isolated supercluster with $p_T > 30$ GeV,
- at least three jets with $p_T > 30$ GeV,
- a separation in ϕ between the highest p_T jet and isolated supercluster of at least $\Delta\phi > 3.0$,
- if the event contains more than one isolated supercluster the invariant mass of any two superclusters must satisfy $M_{sc-sc} > 120$ GeV or $M_{sc-sc} < 60$ GeV,
- small reconstructed missing transverse energy, $\not\!\!E_T < 20$ GeV.

The requirements that $\Delta\phi_{SC-Jet} > 3.0$ and $\not\!\!E_T < 20$ GeV significantly reduce the contamination from $W \rightarrow e\nu$ events in the sample. The requirement on the invariant mass of the two superclusters reduces the contamination from $Z \rightarrow ee$ events.

MC studies shows that, after this selection, there is a irreducible contamination of N_e from γ + jet events of approximately 8.6% in the barrel and 8.3% in the endcap. To account for this, the fake rate applied to data to estimate the number of eejj events is decreased by a corresponding amount.

The ratio of N_e to N_s (fake probability) calculated from data, without the adjustment due to γ + jet contamination, is shown in Fig. 5.9 as a function of the supercluster p_T. A linear fit is performed on the fake rate obtained from data, separately for superclusters reconstructed in the barrel and in the endcaps of ECAL. The resulting fake rates without adjustment due to γ + jet event contamination are

shown in Eq. 5.4, with the errors on the rates taken from the fit results.

$$P(e|s)^{raw}_{barrel} = [(5.67 \pm 0.30) \times 10^{-3}] + [(4.85 \pm 0.67) \times 10^{-5}] \times p_{T\ sc}$$
$$P(e|s)^{raw}_{endcap} = [(1.29 \pm 0.07) \times 10^{-2}] + [(3.18 \pm 0.16) \times 10^{-4}] \times p_{T\ sc} \quad (5.4)$$

The fake rates are adjusted to account for the contamination of non-QCD events. The results are shown in Eq. 5.5.

$$P(e|s)_{barrel} = [(5.07 \pm 0.30) \times 10^{-3}] + [(4.85 \pm 0.67) \times 10^{-5}] \times p_{T\ sc}$$
$$P(e|s)_{endcap} = [(1.13 \pm 0.07) \times 10^{-2}] + [(3.18 \pm 0.16) \times 10^{-4}] \times p_{T\ sc} \quad (5.5)$$

In order to estimate the total number of QCD mulit-jet events passing the full selection criteria, events are first selected that pass a trigger requiring an HLT photon of at least 30 GeV. The photon objects at HLT level are reconstructed superclusters with a loose H/E requirement. This trigger was prescaled in runs with high instantaneous luminosity, leading to an equivalent integrated luminosity of 7.7 pb^{-1} for events passing this trigger. From this sample events are required to have two isolated superclusters of energy in ECAL and two jets ("ssjj") that pass all the kinematic selection criteria. The criteria of M_{ee} and S_T are replaced with equivalent criteria for the isolated superclusters. The number of QCD multi-jet events in the final sample is estimated by rescaling the ssjj events using the probability that both isolated superclusters are reconstructed as HEEP electrons, as shown in Eq. 5.6, where "s" is a reconstructed supercluster passing only the criteria listed in Table 5.6, "e" is a reconstructed electron passing the HEEP ID and isolation criteria, N^{QCD}_{eejj} is the number of QCD multi-jet events in the eejj sample,

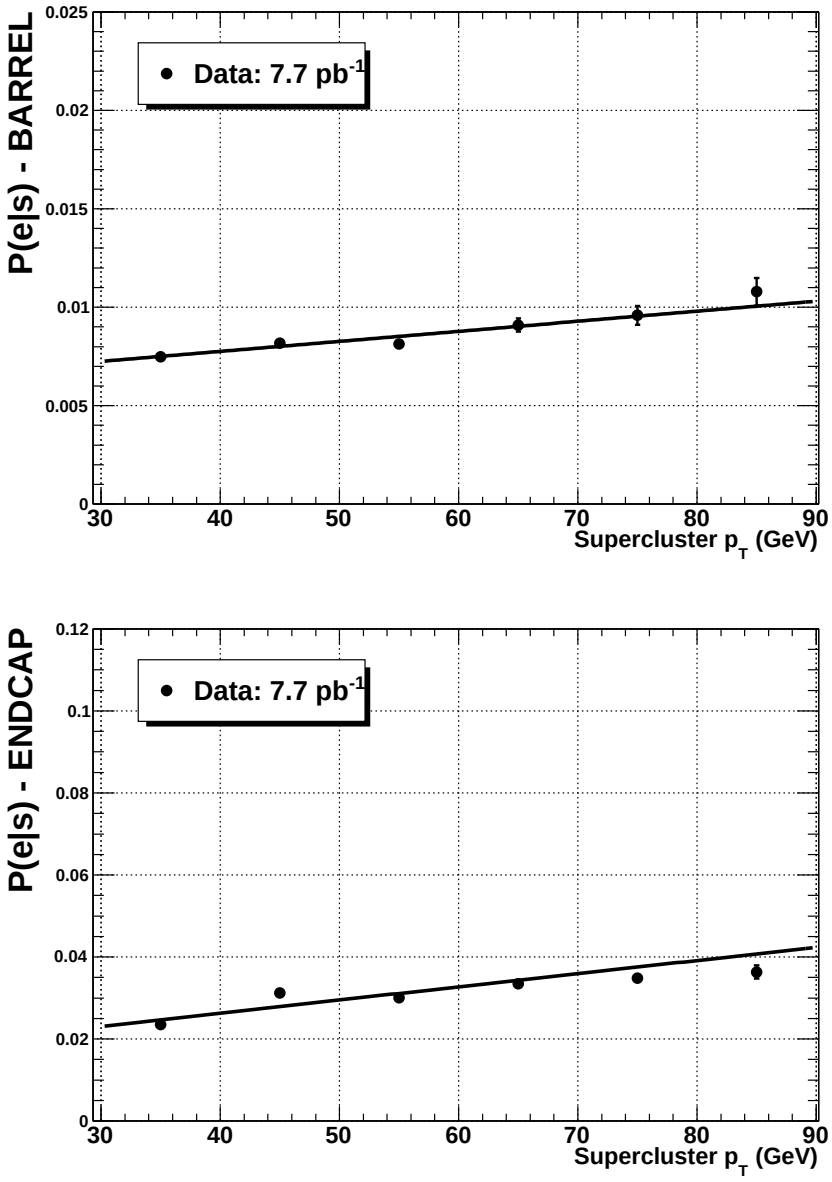

Figure 5.9: The probability (fake rate) that an isolated supercluster is reconstructed as a HEEP electron, before adjustment due to γ + jet contamination, as a function of p_T of the supercluster in the ECAL barrel (top) and endcaps (bottom).

and the sum is performed over the ssjj events in data passing all selection criteria.

$$N_{eejj}^{QCD} = \sum_{ssjj \text{ events in data}} P(e_1|p_T(s_1), \eta(s_1)) \times P(e_2|p_T(s_2), \eta(s_2)) \qquad (5.6)$$

The validity of Eq. 5.6 depends on the independence of $P(e_1|p_T(s_1), \eta(s_1))$ and $P(e_2|p_T(s_2), \eta(s_2))$. With larger statistics this may be investigated by comparing the number of predicted eejj events using both ssjj events and esjj events.

The number of QCD multi-jet events in the eejj sample is estimated using Eq. 5.6. The number of ssjj events in data and the number of predicted QCD multi-jet events in the eejj sample using the fake rate method are reported in Table 5.7. The predicted number of QCD multi-jet events approximately 5% of the total estimated background for all LQ masses considered.

S_T threshold (GeV)	N_{ssjj}^{data} 7.7pb^{-1}	N_{eejj}^{QCD} 7.7pb^{-1}	N_{eejj}^{QCD} 34.7pb^{-1}
470 ($M_{LQ} = 300$)	49	$(1.9 \pm 0.3) \times 10^{-2}$	$(8.6 \pm 1.2) \times 10^{-2}$
490 ($M_{LQ} = 320$)	34	$(1.4 \pm 0.2) \times 10^{-2}$	$(6.3 \pm 1.1) \times 10^{-2}$
510 ($M_{LQ} = 340$)	21	$(9.2 \pm 2.0) \times 10^{-3}$	$(4.1 \pm 0.9) \times 10^{-2}$
540 ($M_{LQ} = 370$)	15	$(6.5 \pm 1.7) \times 10^{-3}$	$(2.9 \pm 0.8) \times 10^{-2}$
560 ($M_{LQ} = 400$)	15	$(6.5 \pm 1.7) \times 10^{-3}$	$(2.9 \pm 0.8) \times 10^{-2}$

Table 5.7: The number of ssjj events in data and the number of predicted QCD multi-jet events in the eejj sample using the fake rate method. The uncertainty on the number of eejj events is derived from the statistics of the rescaled ssjj events.

A closure test is performed on the 7.7 pb^{-1} of data passing the photon HLT to test the validity of the fake rate method by predicting the number of QCD multi-jet

events in a data sample with fewer electrons. Events are selected with one HEEP electron, one supercluster and one jet ("esj" sample). The number of esj events in data with the invariant mass of the electron and supercluster greater than 100 GeV is 537. MC studies predict a contribution of 4% non-QCD SM events in this sample. This number is subtracted from the number of data esj events to give an estimate of 514 QCD multi-jet esj events in data.

The data-driven method described in the previous sections is applied to the data in order to predict the number of esj events from ssj events, a sample dominated by QCD multi-jet events. The number of ssj events to be reweighted is 20160. The predicted number of esj events based on the probability shown in Eq. 5.5 is 418.6 ± 2.9, where the uncertainty is based on the number of ssj events.

The relative difference between the prediction and the actual number of esj events is $|(514) - (418.6 \pm 2.9)|/514 = 23 \pm 4\%$. When this uncertainty is propagated to the eejj estimate where the fake rate is applied once for each electron, a factor of 2 is introduced, resulting in a total uncertainty of $2 \times 23\% = 46\%$.

The distributions in Fig. 5.10 show the p_T of the leading supercluster and the $S_{T\ reduced}$, the sum of the p_T of the three leading objects rather than four as in the full selection criteria, for both the re-weighted ssj sample (i.e. using the fake rate method) and the "actual" esj sample (obtained by counting the events in data passing the selection). A reasonable agreement is observed between the shape of the predicted and actual distributions, evidence that the background estimation method is relatively accurate.

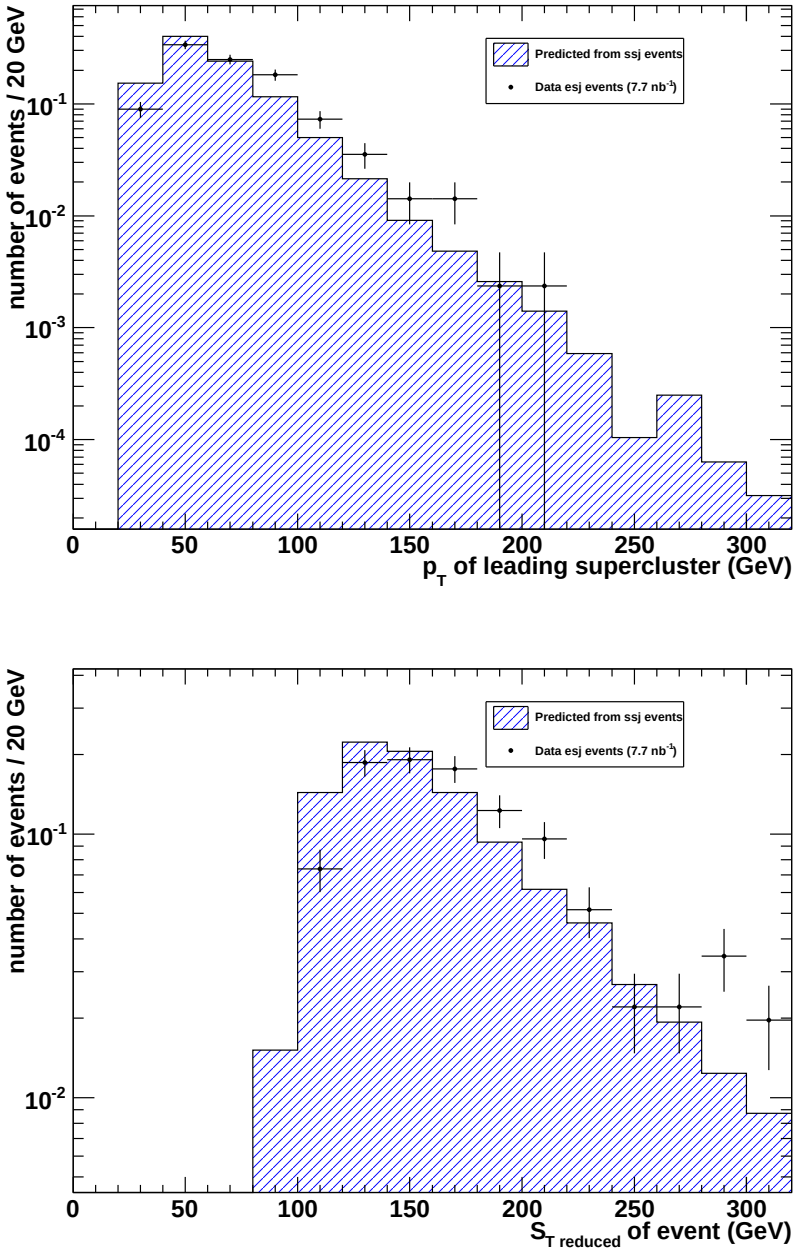

Figure 5.10: Distributions of the p_T of the leading EM object (left) and $S_{T\ reduced}$ (right) for events with one isolated supercluster, one HEEP electron, one jet compared to the distributions for events with two isolated superclusters and one jet reweighted. Both are normalized to unity.

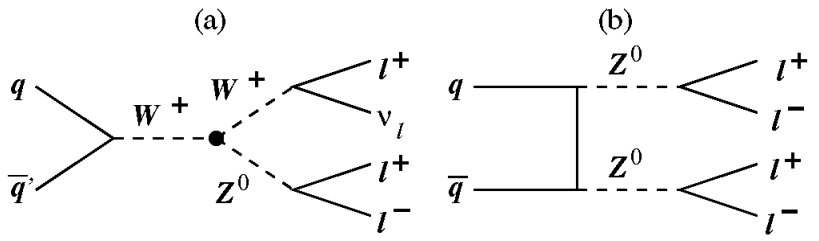

Figure 5.11: Dominant leading order diboson production mechanisms at the LHC.

5.3.4 Other Background Processes

Two other SM processes that may produce events passing the full selection criteria are considered: diboson (VV) events where two vector bosons are produced, and events with photons and jets (γ+jets) in which the photons are mistaken as electrons.

The dominant leading order processes for diboson production at the LHC are shown in Fig. 5.11. The radiation of a Z^0 boson by a W^+ (Figure 5.11 (a)) would proceed through a WWZ vertex. This coupling is non-abelian in the SM and has been shown to be small by experiments at the Tevatron [76] [77]. Additionally, in order for such an event to pass the full selection criteria the Z^0 could decay leptonically and the W^+ hadronically, requiring an additional jet from ISR or FSR, or, conversely, the Z^0 could decay hadronically, the W^+ leptonically and an additional lepton could be reconstructed from an ISR or FSR jet. Both of these configurations depend on contributions from ISR or FSR, reducing further the cross section for such processes producing events passing the selection criteria.

If two Z^0 bosons are produced, as shown in Fig. 5.11 (b), and one decays

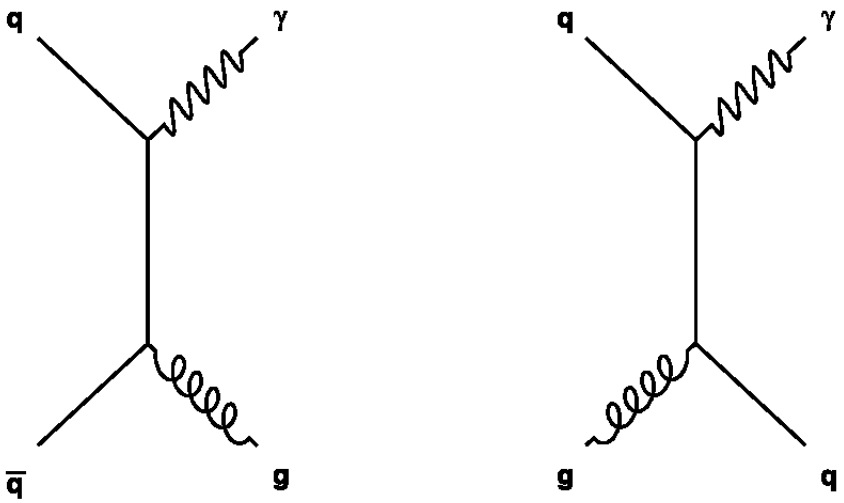

Figure 5.12: Leading order production mechanisms for $\gamma\gamma$+jets events at the LHC.

leptonically while the other decays hadronically, the event content will mimic that of a LQ decay. The production cross section for this process is small, though, as it involves two vertices with coupling strength α_{weak}.

The leading order production processes for events containing at least one photon and at least one jet are shown in Fig. 5.12. The combined cross section of such processes is estimated to be approximately 100 times larger than the process $Z^0 \rightarrow e^+e^-$ for comparison [78]. To pass the selection criteria, however, the process must contain an addition jet and photon from ISR or FSR, and both photons must be reconstructed as HEEP electrons. The probability that a photon will be reconstructed as a HEEP electron is approximately the same as the fake rate probability for an isolated cluster of energy in the ECAL. This is estimated in Sec. 5.3.3 to be approximately 10^{-2}. Applying this factor twice, once per photon, reduces the cross section by a factor of 10^{-4}, making the cross section for γ+jets events at least 10^{-2}

times smaller than that of $Z^0 \rightarrow e^+e^-$.

The negligible size of the contributions to the background events from VV and γ+jets processes are confirmed to be small in MC studies. For an integrated luminosity of 34.7 pb^{-1}, (6.7$\pm$2.3)$\times 10^{-2}$ VV events are predicted to pass the full selection criteria. No γ+jets MC events pass the full selection with the statistics available.

5.4 Systematic Uncertainties

Sources of systematic error are estimated using both MC techniques and methods derived from data. The main sources of error are discussed below. The estimated magnitude and effect of each source of error is listed in Table 5.8. Unless otherwise stated, the errors are assumed to be uncorrelated and therefore added in quadrature and used in 5.6 to calculate the limit on the excluded LQ production cross section.

1. **Jet and electron energy scale** - The reconstructed energy of both electrons and jets is affected by the performance of the calorimeters, introducing an uncertainty on the object energy. In order to estimate the effect of this uncertainty the full event selection is repeated scaling the electron and jet energies by the uncertainty on their energy scales estimated by the appropriate object groups within CMS.

   Uncertainty on the the jet energy scale is estimated to be close to 10% (Sec. 4.2.2). The effect of the jet energy uncertainty is shown to lead to a change in the signal efficiency of $\pm$5%, a change in the $t\bar{t}$ efficiency of approximately $\pm$28%,

a change in the Z/$\gamma*$ +jets efficiency of approximately ± 7%. The discrepancy in the effect of this uncertainty between $t\bar{t}$ and Z/$\gamma*$ +jets events is due to the difference in the selection criteria that most affects each background. The most effective cut on Z/$\gamma*$ +jets events is the requirement that the dielectron invariant mass be larger than 125 GeV, which does not depend on the jet energy. The most effective cut on $t\bar{t}$ events, however, is the large threshold on the S_T, which depends heavily on the jet energy.

Electron energy uncertainty is estimated to be less than 1% in the barrel and approximately 3% in the endcap, which leads to a change in the signal efficiency of ±1%, a change in the $t\bar{t}$ efficiency of approximately ±5%, and a change in the Z/$\gamma*$ +jets efficiency of approximately ± 8%.

The uncertainties on the jet and electron energy scales are combined for Z/$\gamma*$ +jets and $t\bar{t}$ events taking into account their relative contributions to the total background and assuming these uncertainties are correlated for the two backgrounds.

2. **Integrated luminosity of the data** - Luminosity is calculated by dividing the number of events registered in the very forward region of HF (Sec. 2.2.3) by the total theoretical cross section of all SM processes and the MC estimated fraction of events recovered in that region ("efficiency") (see Eq. 1.2). Both the theoretical cross section and the efficiency have uncertainties associated with them, leading to an overall uncertainty in the calculated integrated luminosity.

   The uncertainty on this calculation is estimated by the CMS Luminosity group

to be 11% for the period of data taking considered [79]. This effect is taken into account on the signal but not on the background as the MC estimates for the dominant backgrounds are scaled to data and the uncertainties derived from the scaling incorporate the uncertainty on the luminosity.

3. **Statistical uncertainty on the MC samples** -

   The statistical uncertainty on MC LQ events passing the full selection criteria is summarized in Table 5.9. For $t\bar{t}$ contributions the statistical uncertainty associated with the number of MC events is 7%, while for Z/$\gamma*$ +jets events it is 8%.

4. **Electron reconstruction, identification and isolation efficiencies** -

   The uncertainty on the electron reconstruction efficiency has been estimated by the CMS EGamma working group by selecting Z boson events with one electron passing tight identification criteria and a supercluster in the ECAL passing loose isolation criteria. The reconstruction efficiency is the probability that the supercluster will be reconstructed as an electron. The uncertainty on the efficiency is found to be 0.5% in the barrel and 0.8% in the endcap [80]. The uncertainties on the HEEP identification and isolation efficiencies have been estimated by the HEEP group using the tag and probe method described in 5.2.2. They are currently estimated to be 0.5% for the barrel and 0.9% for the endcap [81]. MC studies suggest this efficiency decreases with the addition of jets in the events. A conservative estimate is taken on the total reconstruction efficiency uncertainty (reconstructed electron + HEEP criteria)

to be 5% per electron.

5. **Uncertainties from the data-driven background estimates** - The data-driven techniques for QCD multi-jet background estimates are discussed in Sec. 5.3.3. A closure test performed on a data sample enriched in QCD multi-jet events suggests a 46% uncertainty on the intrinsic precision of the method, which contributes a 2% uncertainty to the total background as the QCD estimate is approximately 5% of the total number of background events.

   The uncertainties on scale factors for the Z/$\gamma*$+jet and $t\bar{t}$ events are discussed in Secs. 5.3.1 and 5.3.2, respectively, and are taken to be ± 12% and ± 20%.

Systematic Uncertainty	Magnitude	Effect on Signal Efficiency	Effect on $N_{t\bar{t}}$	Effect on $N_{Z/\gamma*+\text{jet}}$	Effect on N_{AllBkg}
Jet Energy Scale	±10%	±5%	±28%	±7%	±14%
Electron Energy Scale	±1%(3%)	±1%	±5%	±8%	±7%
Integrated Luminosity	±11%	±11%	-	-	-
MC Statistics		±1%	±7%	±8%	±8%
Electron Reco/ID/Iso	±5% per e	±10%	±10%	±10%	±10%
Data Driven Estimates		-	±20%	±11%	±15%
Total		±16%	±37%	±21%	±25%

Table 5.8: Sources and effects of systematic uncertainties on background and signal events. Effects are combined based on relative contributions of SM processes after selection criteria corresponding to a 300 GeV LQ signal.

5.5 Results

Selection criteria have been defined and optimized in order to minimize the possible excluded cross section for LQ pair production. The number of SM background events passing the full selection criteria has been estimated with a combination of MC and data driven techniques, and uncertainties have been estimated for all contributions. Systematic uncertainties have been evaluated for both the data and the MC predictions. Table 5.9 lists the number of data and estimated MC events passing the full selection criteria for various LQ mass hypothesis, along with the estimated number of signal events from MC. No significant deviation from SM predictions are found in the data.

M_{LQ}	Events in	Selection	Events in MC samples				Events
(GeV)	MC Signal	Efficiency	$t\bar{t}$ + jets	Z/γ + jets	Other Bkgs	All Bkgs	in Data
300	18.1±0.09	0.430±0.002	0.46±0.04	0.77±0.07	0.10±0.02	1.3 ±0.1	1
320	12.9±0.06	0.451±0.002	0.38±0.04	0.67±0.07	0.09±0.02	1.1 ±0.1	1
340	9.28±0.04	0.469±0.002	0.28±0.03	0.57±0.07	0.08±0.02	0.94±0.08	1
370	5.80±0.03	0.496±0.002	0.23±0.03	0.48±0.06	0.07±0.02	0.79±0.07	1
400	3.71±0.02	0.522±0.002	0.17±0.03	0.42±0.06	0.06±0.02	0.65±0.07	1

Table 5.9: Number of events for 34.7 pb^{-1} MC LQ signal, MC background and data samples after the full analysis selection. "Other Bkgs" includes QCD multi-jet, W + jets and di-boson MC samples. Uncertainties are statistical.

5.6 LQ Cross Section and Mass Exclusion

Given the results from Sec. 5.5, one would like to establish the probability that a number of signal events was produced as a function of the number of observed events and the number of background events expected. This translates to establishing the probability that the production cross section, σ, falls within a certain range, given a number of observed events, n_{obs}, within a given integrated luminosity, L_{int}, with a given number of expected background events, n_{Bkgd}. In Bayesian statistics this is expressed as the integral of the cross section probability density function over the range σ_{low} to σ_{high}, as shown in Eq. 5.7.

$$\int_{\sigma_{low}}^{\sigma_{high}} p(\sigma|n_{obs}, L_{int}, n_{Bkgd})\ d\sigma \tag{5.7}$$

Bayesian statistical methods have been employed, as opposed to frequentist methods, in order to take into account the prior knowledge of the cross section, namely that it can not take on values less than 0.

In Bayesian statistics one assigns a probability density function, a "prior", that is a reflection of the belief in the true value of the parameter under investigation, here σ. The prior used here, $\pi(\sigma)$ is defined in Eq. 5.8.

$$\pi(\sigma) = \begin{cases} 1 & : \sigma > 0 \\ 0 & : \sigma < 0 \end{cases} \tag{5.8}$$

One must also consider how likely the measured result is given a certain value of the parameter, $L(n_{obs}|\sigma, A, L_{int}, n_{Bkgd})$. The Poisson distribution, shown in Eq. 5.9, describes the probability of a fixed number of independent events, k, occurring given

an expected number of occurrences, λ.

$$f(k,\lambda) = \frac{\lambda^k e^{-\lambda}}{k!} \tag{5.9}$$

Here it is assumed that the likelihood probability density function of the data is a Poisson distribution with the expected number of events equal to the predicted number of signal and background events, as shown in Eq. 5.10.

$$L(n_{obs}|n_{signal}, n_{Bkgd}) = \frac{(n_{signal} + n_{Bkgd})^{n_{obs}}}{n_{obs}!} e^{-(n_{signal}+n_{Bkgd})} \tag{5.10}$$

The number of observed events is given by the signal cross section, σ, the probability of a signal event to pass the full analysis criteria, A (efficiency $\times$ acceptance), and the integrated luminosity, L_{int}. Inserting this into Eq. 5.10 results in Eq. 5.11.

$$L(n_{obs}|\sigma, A, L_{int}, n_{Bkgd}) = \frac{(\sigma A L_{int} + n_{Bkgd})^{n_{obs}}}{n_{obs}!} e^{-(\sigma A L_{int}+n_{Bkgd})} \tag{5.11}$$

Bayes' theorem for continuous probability density functions states that the conditional probability density function of the parameter (the "posterior"), given the measured conditions, is the normalized product of the likelihood of the measured result and the prior of the parameter, as shown in Eq. 5.12.

$$p(\sigma|n_{obs}, L_{int}, n_{Bkgd}) = \frac{L(n_{obs}|\sigma, A, L_{int}, n_{Bkgd})\pi(\sigma)}{\int_{-\infty}^{+\infty} p(\sigma|n_{obs}, L_{int}, n_{Bkgd})d\sigma} \tag{5.12}$$

To determine an upper limit on the cross section, σ_{up}, with a 95% confidence level the integral from 0 to σ_{up} of the posterior is required to be 0.95, as shown in Eq. 5.13.

$$\int_0^{\sigma_{up}} p(\sigma|n_{obs}, L_{int}, n_{Bkgd})d\sigma = 0.95 \tag{5.13}$$

Uncertainty on the parameters in the likelihood function, $L(n_{obs}|\sigma, A, L_{int}, n_{Bkgd})$, can be taken into account by using a modified Poisson distribution, L′, defined in Eq. 5.14, where the functions $f(A')$, $g(\mathcal{L}')$, and $h(n'_{Bkgd})$ are probability density functions of the parameters using the uncertainty on the parameters. In this analysis the distributions are assumed to be Gaussian centered at A, L_{int} and n_{Bkgd}, with a standard deviation set by the uncertainty on the respective parameter.

$$L'(n_{obs}|\sigma, A, L_{int}, n_{Bkgd}) = \int_0^{+\infty}\int_0^{+\infty}\int_0^{+\infty} L(n_{obs}|\sigma, A', L'_{int}, n'_{Bkgd}) \\ f(A')g(L'_{int})h(b')\ dA'dL'_{int}dn'_{Bkgd} \qquad (5.14)$$

An upper limit on the leptoquark cross section is calculated using this approach for each leptoquark mass hypothesis, using the uncertainties discussed in Section 5.4. Figure 5.13 shows the observed 95% confidence level upper limit, the expected 95% confidence level upper limit, and the theoretical cross section as a function of leptoquark mass. The uncertainty band on the theoretical cross section corresponds to the uncertainty due to renormalization and factorization scale, and the choice of PDF. The magnitude of these uncertainties are shown in Tab. 5.1. The observed cross section limit is calculated using the number of observed data events passing the full selection criteria. The expected limit is calculated by taking a weighted average over n possible observed events, where the weight is the likelihood that n events will be observed, as described in Sec. 5.6. The intersection of the smooth curve connecting observed cross section limits and the theoretical cross section at 388 GeV is used as a lower limit on the LQ mass.

The observed upper limit cross section corresponds to the cross section for

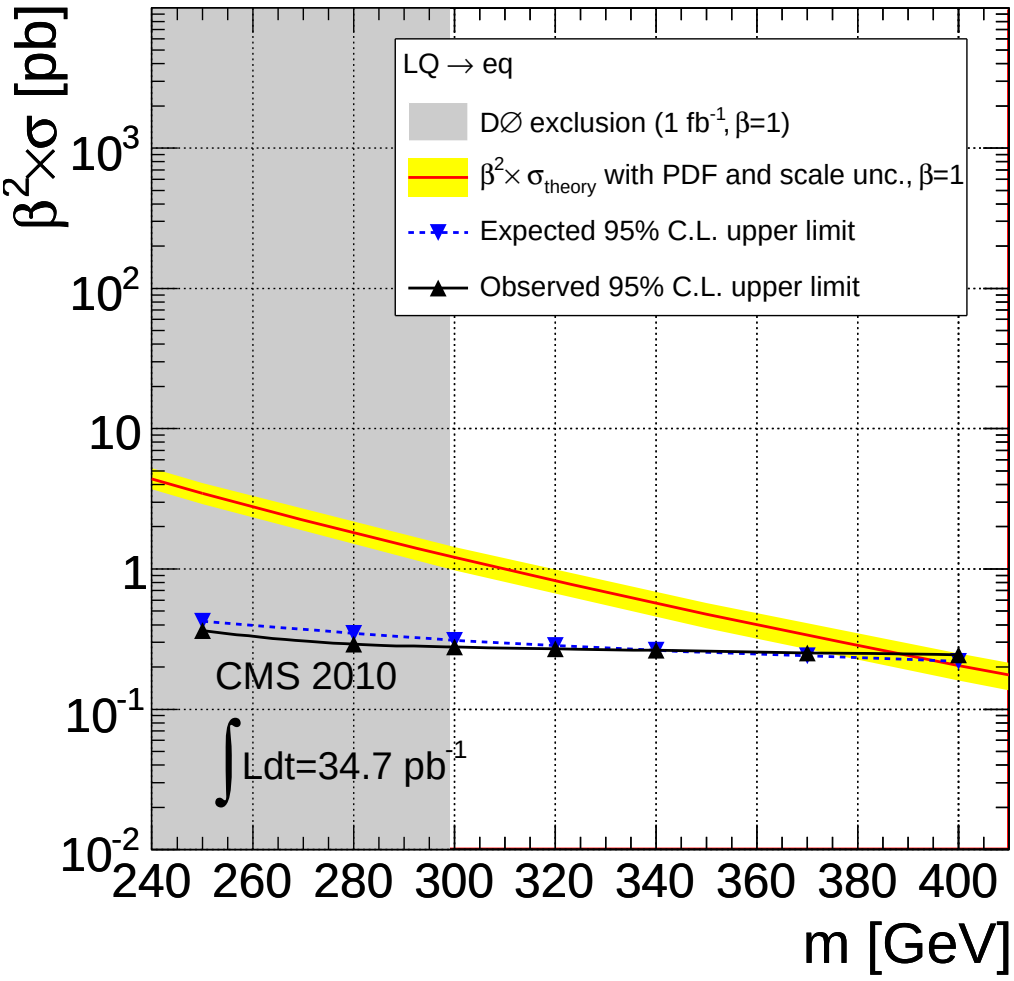

Figure 5.13: 95% confidence level upper limit on the leptoquark production cross section as a function of hypothesized leptoquark mass.

leptoquark pair production and the decay of *both* leptoquarks to an electron and a quark. If the branching fraction is less than one this measurment corresponds only to the fraction of the cross section that describes the two electron and two jet channel. To calculate the minimum β excluded at each leptoquark mass point the observed 95% confidence level upper limit cross section for β=1 (σ_{obs}) is compared to the theoretical cross section (σ_{theory}), as shown in Eq. 5.15. This ratio is equal to β^2, one application of the branching fraction for each of the two leptoquarks produced.

$$\beta^2 = \frac{\sigma_{obs}}{\sigma_{theory}} \tag{5.15}$$

The excluded mass region is calculated as a function of β and shown in Fig. 5.14, along with the region previously excluded by the DØ Collaboration. At low values of β the DØ Collaboration is able to exclude larger values of leptoquark mass due to the combination of searches specific to the low β channels (see Fig. 1.6). At values of β close to one the exclusion from the DØ Collaboration covers smaller values of leptoquark mass due to the smaller theoretical cross section at lower center of mass energy.

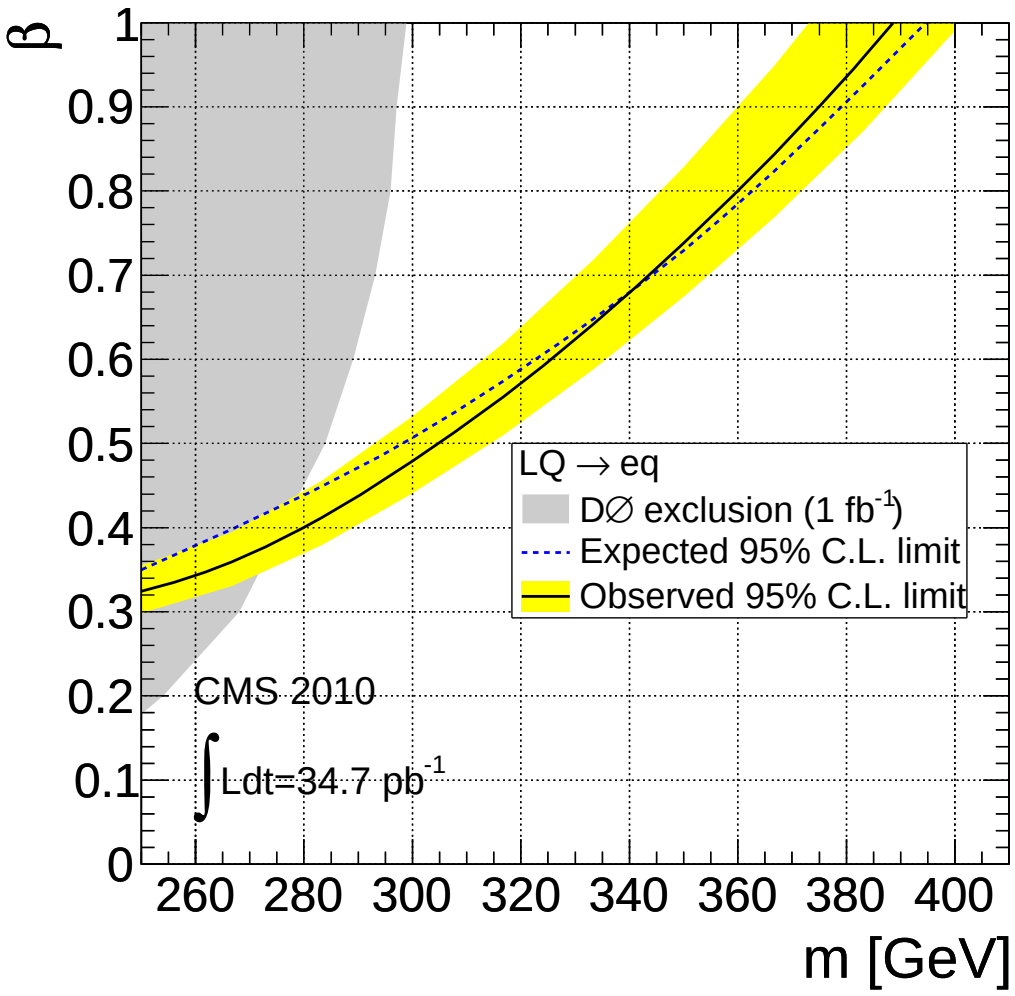

Figure 5.14: Minimum branching ratio, β of leptoquark into charged lepton as a function of leptoquark mass hypothesis based on the measurement of the two charged lepton and jet channel.

Chapter 6

Conclusion and Future Prospects

6.1 Cross section and leptoquark mass limit

A search for first generation scalar leptoquarks with a branching fraction into charged leptons $\beta = 1$ has been presented here. The analysis has been completed with 34.6 pb^{-1} of data collected during LHC operation during 2010 at a center-of-mass energy of 7 TeV. The single data event passing the full selection criteria is consistent with the expected number of SM background events for all considered LQ masses. A 95% confidence level upper limit on the cross section is established at each leptoquark mass hypothesis using the Bayesian methods described in Sec. 5.6. Comparison with theoretical cross section values allows a 95% confidence level exclusion of first generation scalar leptoquarks up to a mass of 388 GeV, an improvement of 89 GeV on the most recent limit from the DØ Collaboration [82].

This analysis does not address limits on the model parameter λ, the Yukawa coupling at the lepton-quark-leptoquark vertex, as this vertex is not included in the dominant production mechanism at the LHC.

6.2 Future prospects

MC studies have shown that the exclusion potential at CMS for first generation scalar LQ with an integrated luminosity of 100 pb^{-1} at a center of mass energy of $\sqrt{s} = 7$ TeV is approximately a LQ mass of 480 GeV. At a center of mass energy of $\sqrt{s} = 10$ TeV the potentially excluded LQ mass increases to approximately 590 GeV with an integrated luminosity of 100 pb^{-1}.

If $\beta < 1$ each leptoquark would have a non-zero probability to decay to a neutrino and quark, a search that warrants a slightly different analysis approach, as the neutrino is not directly reconstructed but appears as missing transverse energy ($\not\!\!E_T$). This analysis is currently being pursued by another group within the CMS collaboration. In the absence of a signal, results from both analysis can be combined to improve the excluded mass region shown in Fig. 5.14.

A similar analysis strategy as the one employed here has been applied to a search for second generation scalar leptoquarks at CMS [84]. Searches for third generation leptoquarks requires significantly more data than needed for first or second generation searches due to the difficult reconstruction of the tau. Such a search is foreseen in CMS once adequate data are available.

Searches for vector leptoquarks have been conducted at previous experiments [85]. The analysis strategy employed by the DØ Collaboration for vector LQ was identical to that for scalar LQ. Signal samples were produced with a modified version of PYTHIA to include vector LQ decays. Similar results may be derived at CMS in the future to complete the search for the variety of theorized leptoquark models.

Appendix A

Additional standard model mathematical formalism

A.1 γ Matricies

The γ matrices are 4x4 matrices that satisfy the following conditions:

- $(\gamma^0)^2 = 1$,
- $(\gamma^i)^2 = -1$ for i=1,2,3,
- $\gamma^\mu\gamma^\nu + \gamma^\nu\gamma^\mu = 0$ for $\mu \neq \nu$

There are several equivalent sets of γ matrices that satisfy these conditions. The following are the "Bjorken and Drell" convention:

$$\gamma^0 = \begin{pmatrix} 1 & 0 \\ 0 & -1 \end{pmatrix}$$

$$\gamma^i = \begin{pmatrix} 0 & \sigma^i \\ \sigma^i & 0 \end{pmatrix}$$

where 0,1 and -1 are the 2x2 zero and unity matrices, and σ^i are the 2x2 Pauli matrices, defined as:

$$\sigma^1 = \begin{pmatrix} 0 & 1 \\ 1 & 0 \end{pmatrix}$$

$$\sigma^2 = \begin{pmatrix} 0 & -i \\ i & 0 \end{pmatrix}$$

$$\sigma^3 = \begin{pmatrix} 1 & 0 \\ 0 & -1 \end{pmatrix}$$

A.2 Massless A_μ Field

The Dirac Lagrangian for a spin 1/2 field, as shown in Equation A.1 is not locally gauge invariant.

$$\mathbf{L} = i(\hbar c)\bar{\psi}\gamma^\mu\partial_\mu\psi - (mc^2)\bar{\psi}\psi \tag{A.1}$$

It can be made invariant by the addition of a vector field, A_μ, and the substitution of the covariant derivative, Equation A.2, for the standard derivative.

$$\partial_\mu \rightarrow D_\mu = \partial_\mu + i\frac{q}{\hbar c}A_\mu \tag{A.2}$$

The additional A_μ field warrants the addition of a free term to the full Lagrangian. The standard Proca Lagrangian for a free vector field is shown in Equation A.3, where $F^{\mu\nu} = \partial^\mu A^\nu - \partial^\nu A^\mu$.

$$\mathbf{L} = \frac{-1}{16}F^{\mu\nu}F_{\mu\nu} + \frac{1}{8\pi}(\frac{m_A c}{\hbar})^2 A^\nu A_\nu \tag{A.3}$$

This addition to the full Lagrangian must also be invariant under local gauge

transformations. Consider the transformation of $F^{\mu\nu}$. The vector field A_μ transforms as shown in Equation A.4.

$$A_\mu \rightarrow A_\mu - \frac{\hbar c}{q}\partial_\mu \theta \tag{A.4}$$

Thus, $F^{\mu\nu}$ transforms as shown in Equation A.5.

$$\begin{aligned} \partial^\mu(A^\nu - \frac{\hbar c}{q}\partial^\nu\theta) &- \partial^\nu(A^\mu - \frac{\hbar c}{q}\partial^\mu\theta) \\ = \partial^\mu A^\nu - \frac{\hbar c}{q}\partial^\mu\partial^\nu\theta &- \partial^\nu A^\mu + \frac{\hbar c}{q}\partial^\nu\partial^\mu\theta \\ = (\partial^\mu A^\nu - \partial^\nu A^\mu) &- (\frac{\hbar c}{q}\partial^\mu\partial^\nu\theta - \frac{\hbar c}{q}\partial^\nu\partial^\mu\theta) \\ = F^{\mu\nu} &- \frac{\hbar c}{q}(\partial^\mu\partial^\nu\theta - \partial^\nu\partial^\mu\theta) \\ = F^{\mu\nu} & \end{aligned} \tag{A.5}$$

Therefore the first term in the Proca Lagrangian (Eq. A.3) is invariant. The second term, however, is not invariant. In order to retain the invariance of the full Lagrangian the mass of the vector field, m_A, must be set to zero.

Appendix B

CMS data set names

Data Sample	Run range	Luminosity (pb^{-1})
/EG/Run2010A-Sep17ReReco-v2/RECO	132440–144114	3.07
/Electron/Run2010B-PromptReco-v2/RECO	146428–149294	31.67
Total integrated luminosity		34.7 pb^{-1}

Table B.1: The dataset name, the run range considered, and the integrated luminsosity of the sample.

Appendix C

Selection Efficiencies

Selection efficiencies for MC signal samples and dominant MC background scaled to 34.7 pb^{-1}.

Criteria	N_{events} Pass LQ (M=300 GeV)	Relative Efficiency	Total Efficiency
Electron criteria	27.14 ± 0.09	0.65 ± 0.00	0.65 ± 0.00
Jet criteria	25.88 ± 0.09	0.95 ± 0.00	0.62 ± 0.00
$\Delta R(ele - jet) > 0.7$	24.56 ± 0.09	0.95 ± 0.00	0.59 ± 0.00
$M_{ee} > 125$ GeV	21.12 ± 0.09	0.86 ± 0.00	0.50 ± 0.00
$S_T > 470$ GeV	18.06 ± 0.09	0.86 ± 0.00	0.43 ± 0.00

Table C.1: Sequence of selection criteria and the number of 300 GeV LQ MC events passing each, scaled to 34.7 pb^{-1}. Efficiency is quoted with respect to the original MC sample process listed in Sec. 5.1.

Criteria	N_{events} Pass LQ (M=400 GeV)	Relative Efficiency	Total Efficiency
Electron criteria	4.78 ± 0.02	0.67 ± 0.00	0.67 ± 0.00
Jet criteria	4.63 ± 0.02	0.97 ± 0.00	0.65 ± 0.00
$\Delta R(ele - jet) > 0.7$	4.41 ± 0.02	0.95 ± 0.00	0.62 ± 0.00
$M_{ee} > 125$ GeV	4.06 ± 0.02	0.92 ± 0.00	0.57 ± 0.00
$S_T > 470$ GeV	3.96 ± 0.02	0.98 ± 0.01	0.56 ± 0.00

Table C.2: Sequence of selection criteria and the number of 400 GeV LQ MC events passing each, scaled to 34.7 pb^{-1}. Efficiency is quoted with respect to the original MC sample process listed in Sec. 5.1.

Criteria	N_{events} Pass $t\bar{t}$	Relative Efficiency	Total Efficiency
Electron criteria	23.32 ± 0.30	$(4.07 \pm 0.05) \times 10^{-3}$	$(4.07 \pm 0.05) \times 10^{-3}$
Jet criteria	17.70 ± 0.26	$(7.6 \pm 0.02) \times 10^{-1}$	$(3.09 \pm 0.05) \times 10^{-3}$
$\Delta R(ele - jet) > 0.7$	16.30 ± 0.25	$(9.20 \pm 0.20) \times 10^{-1}$	$(2.85 \pm 0.04) \times 10^{-3}$
$M_{ee} > 125$ GeV	6.61 ± 0.16	$(4.06 \pm 0.01) \times 10^{-1}$	$(1.15 \pm 0.03) \times 10^{-3}$
$S_T > 470$ GeV	0.46 ± 0.04	$(6.95 \pm 0.66) \times 10^{-2}$	$(8.02 \pm 0.74) \times 10^{-5}$

Table C.3: Sequence of selection criteria and the number of $t\bar{t}$ MC events passing each, scaled to 34.7 pb^{-1}. Efficiency is quoted with respect to the original MC sample process listed in Sec. 5.1.

Criteria	N_{events} Pass $Z/\gamma*$+jets	Relative Efficiency	Total Efficiency
Electron criteria	$(1.05 \pm 0.00) \times 10^4$	$(8.19 \pm 0.02) \times 10^{-2}$	$(8.19 \pm 0.02) \times 10^{-2}$
Jet criteria	$(2.67 \pm 0.03) \times 10^2$	$(2.54 \pm 0.03) \times 10^{-2}$	$(2.08 \pm 0.02) \times 10^{-3}$
$\Delta R(ele - jet) > 0.7$	$(2.53 \pm 0.03) \times 10^2$	$(9.48 \pm 0.15) \times 10^{-1}$	$(1.97 \pm 0.02) \times 10^{-3}$
$M_{ee} > 125$ GeV	5.61 ± 0.38	$(2.22 \pm 0.15) \times 10^{-2}$	$(4.37 \pm 0.30) \times 10^{-5}$
$S_T > 470$ GeV	0.77 ± 0.07	$(1.37 \pm 0.16) \times 10^{-1}$	$(5.97 \pm 0.55) \times 10^{-6}$

Table C.4: Sequence of selection criteria and the number of $Z/\gamma*$+jets MC events passing each, scaled to 34.7 pb^{-1}. Efficiency is quoted with respect to the original MC sample process listed in Sec. 5.1.

Appendix D

Trigger Tables for Primary Datasets

D.1 Electron PD Trigger Tables

Table D.1: Trigger menu for 2E32 Electron primary dataset, deployed Oct. 23rd, 2010.

Trigger Name	L1 condition
HLT_Ele17_SW_TighterEleIdIsol_L1R	L1_SingleEG8
HLT_Ele22_SW_TighterEleId_L1R	L1_SingleEG8
HLT_Ele17_SW_TightCaloEleId_Ele8HE_L1R	L1_SingleEG8
HLT_DoubleEle17_SW_L1R	L1_SingleEG8
HLT_Ele32_SW_TighterEleId_L1R	L1_SingleEG8
HLT_Ele13_HT70	L1 EG8
HLT_Ele8_HT100	L1 HTxx

Table D.2: Trigger menu for 6E31 Electron primary dataset, deployed Oct. 4th, 2010.

Trigger Name	L1 condition
HLT_Ele12_SW_TighterEleIdIsol_L1R	L1_SingleEG8
HLT_Ele17_SW_TightEleId_L1R	L1_SingleEG8
HLT_Ele27_SW_TightCaloEleIdTrack_L1R	L1_SingleEG8
HLT_Ele17_SW_TightCaloEleId_SC8HE_L1R	L1_SingleEG8
HLT_DoubleEle15_SW_L1R	L1_DoubleEG5
HLT_Ele17_SW_TightEleIdIsol_L1R	L1_SingleEG8
HLT_Ele17_SW_TighterEleId_L1R	L1_SingleEG8
HLT_Ele17_SW_TighterEleIdIsol_L1R	L1_SingleEG8
HLT_Ele32_SW_TightCaloEleIdTrack_L1R	L1_SingleEG8

Table D.3: Trigger menu for 2E31 Electron primary dataset, deployed Sept. 22nd, 2010.

Trigger Name	L1 condition
HLT_Ele12_SW_EleIdIsol_L1R	L1_SingleEG5
HLT_Ele17_SW_LooseEleId_L1R	L1_SingleEG5
HLT_Ele17_SW_CaloEleId_L1R	L1_SingleEG5
HLT_Ele22_SW_CaloEleId_L1R	L1_SingleEG8
HLT_DoubleEle10_SW_L1R	L1_DoubleEG5
HLT_Ele12_SW_EleIdIsolNoDEtaInEE_L1R	L1_SingleEG5
HLT_Ele17_SW_EleId_L1R	L1_SingleEG5

D.2 EGamma PD Trigger Tables

Table D.4: Trigger menu for 3.5E30 EGamma primary dataset, deployed Aug. 3rd, 2010.

Trigger Name	L1 condition
HLT_Photon15_Cleaned_L1R	L1_SingleEG5
HLT_Photon20_Cleaned_L1R	L1_SingleEG8
HLT_DoublePhoton4_Jpsi_L1R	L1_DoubleEG2
HLT_DoublePhoton4_Upsilon_L1R	L1_DoubleEG2
HLT_DoublePhoton4_eeRes_L1R	L1_DoubleEG2
HLT_DoublePhoton5_Jpsi_L1R	L1_SingleEG8 OR L1_DoubleEG5
HLT_DoublePhoton5_Upsilon_L1R	L1_SingleEG8 OR L1_DoubleEG5
OpenHLT_DoublePhoton15_L1R	L1_DoubleEG5
OpenHLT_Ele10_SW_EleId_L1R	SingleEG5
OpenHLT_Ele15_SW_L1R	SingleEG5
OpenHLT_Ele15_SW_EleId_L1R	SingleEG5
HLT_Ele15_SC10_LW_L1R	SingleEG5
OpenHLT_Ele20_SW_L1R	L1_SingleEG8
OpenHLT_DoubleEle10_LW_L1R	L1_DoubleEG5

Table D.5: Trigger menu for 1.6E30 EGamma primary dataset, deployed July 13th, 2010.

Trigger Name	L1 condition
HLT_DoubleEle5_SW_L1R	L1_DoubleEG5
HLT_DoublePhoton10_L1R	L1_DoubleEG5
HLT_DoublePhoton4_Jpsi_L1R	L1_DoubleEG2
HLT_DoublePhoton4_Upsilon_L1R	L1_DoubleEG2
HLT_DoublePhoton4_eeRes_L1R	L1_DoubleEG2
HLT_DoublePhoton5_Jpsi_L1R	L1_SingleEG8 OR L1_DoubleEG5
HLT_DoublePhoton5_L1R	L1_DoubleEG5
HLT_DoublePhoton5_Upsilon_L1R	L1_SingleEG8 OR L1_DoubleEG5
HLT_Ele10_LW_EleId_L1R	L1_SingleEG5
HLT_Ele10_LW_L1R	L1_SingleEG5
OpenHLT_Ele10_LW_L1R	L1_SingleEG5
OpenHLT_Ele10_SW_L1R	L1_SingleEG5
HLT_Ele15_LW_L1R	L1_SingleEG5
HLT_Ele15_SC10_LW_L1R	L1_SingleEG5
HLT_Ele15_SiStrip_L1R	L1_SingleEG5
HLT_Ele20_LW_L1R	L1_SingleEG8
HLT_Photon10_Cleaned_L1R	L1_SingleEG5
HLT_Photon15_Cleaned_L1R	L1_SingleEG5
HLT_Photon15_LooseEcalIso_L1R	L1_SingleEG5
HLT_Photon15_TrackIso_L1R	L1_SingleEG5
HLT_Photon20_Cleaned_L1R	L1_SingleEG8
HLT_Photon30_L1R_8E29	L1_SingleEG5

Appendix E

CMS Author List as of November, 2010

Yerevan Physics Institute, Yerevan, Armenia

V. Khachatryan, A.M. Sirunyan, A. Tumasyan

Institut für Hochenergiephysik der OeAW, Wien, Austria

W. Adam, T. Bergauer, M. Dragicevic, J. Erö, C. Fabjan, M. Friedl, R. Frühwirth, V.M. Ghete, J. Hammer[1], S. Hänsel, C. Hartl, M. Hoch, N. Hörmann, J. Hrubec, M. Jeitler, G. Kasieczka, W. Kiesenhofer, M. Krammer, D. Liko, I. Mikulec, M. Pernicka, H. Rohringer, R. Schöfbeck, J. Strauss, A. Taurok, F. Teischinger, W. Waltenberger, G. Walzel, E. Widl, C.-E. Wulz

National Centre for Particle and High Energy Physics, Minsk, Belarus

V. Mossolov, N. Shumeiko, J. Suarez Gonzalez

Universiteit Antwerpen, Antwerpen, Belgium

L. Benucci, L. Ceard, K. Cerny, E.A. De Wolf, X. Janssen, T. Maes, L. Mucibello, S. Ochesanu, B. Roland, R. Rougny, M. Selvaggi, H. Van Haevermaet, P. Van Mechelen, N. Van Remortel

Vrije Universiteit Brussel, Brussel, Belgium

V. Adler, S. Beauceron, F. Blekman, S. Blyweert, J. D'Hondt, O. Devroede, R. Gonzalez Suarez, A. Kalogeropoulos, J. Maes, M. Maes, S. Tavernier, W. Van Doninck, P. Van Mulders, G.P. Van Onsem, I. Villella

Université Libre de Bruxelles, Bruxelles, Belgium

O. Charaf, B. Clerbaux, G. De Lentdecker, V. Dero, A.P.R. Gay, G.H. Hammad, T. Hreus, P.E. Marage, L. Thomas, C. Vander Velde, P. Vanlaer, J. Wickens

Ghent University, Ghent, Belgium

S. Costantini, M. Grunewald, B. Klein, A. Marinov, J. Mccartin, D. Ryckbosch, F. Thyssen, M. Tytgat, L. Vanelderen, P. Verwilligen, S. Walsh, N. Zaganidis

Université Catholique de Louvain, Louvain-la-Neuve, Belgium

S. Basegmez, G. Bruno, J. Caudron, J. De Favereau De Jeneret, C. Delaere, P. Demin, D. Favart, A. Giammanco, G. Grégoire, J. Hollar, V. Lemaitre, J. Liao, O. Militaru, S. Ovyn, D. Pagano, A. Pin, K. Piotrzkowski, L. Quertenmont, N. Schul

Université de Mons, Mons, Belgium

N. Beliy, T. Caebergs, E. Daubie

Centro Brasileiro de Pesquisas Fisicas, Rio de Janeiro, Brazil

G.A. Alves, D. De Jesus Damiao, M.E. Pol, M.H.G. Souza

Universidade do Estado do Rio de Janeiro, Rio de Janeiro, Brazil

W. Carvalho, E.M. Da Costa, C. De Oliveira Martins, S. Fonseca De Souza, L. Mundim, H. Nogima, V. Oguri, W.L. Prado Da Silva, A. Santoro, S.M. Silva Do Amaral, A. Sznajder, F. Torres Da Silva De Araujo

Instituto de Fisica Teorica, Universidade Estadual Paulista, Sao Paulo, Brazil

F.A. Dias, M.A.F. Dias, T.R. Fernandez Perez Tomei, E. M. Gregores[2] F. Marinho, S.F. Novaes, Sandra S. Padula

Institute for Nuclear Research and Nuclear Energy, Sofia, Bulgaria

N. Darmenov[1], L. Dimitrov, V. Genchev[1], P. Iaydjiev[1], S. Piperov, M. Rodozov, S. Stoykova, G. Sultanov, V. Tcholakov, R. Trayanov, I. Vankov

University of Sofia, Sofia, Bulgaria

M. Dyulendarova, R. Hadjiiska, V. Kozhuharov, L. Litov, E. Marinova, M. Mateev, B. Pavlov, P. Petkov

Institute of High Energy Physics, Beijing, China

J.G. Bian, G.M. Chen, H.S. Chen, C.H. Jiang, D. Liang, S. Liang, J. Wang, J. Wang, X. Wang, Z. Wang, M. Xu, M. Yang, J. Zang, Z. Zhang

State Key Lab. of Nucl. Phys. and Tech., Peking University, Beijing, China

Y. Ban, S. Guo, W. Li, Y. Mao, S.J. Qian, H. Teng, B. Zhu

Universidad de Los Andes, Bogota, Colombia

A. Cabrera, B. Gomez Moreno, A.A. Ocampo Rios, A.F. Osorio Oliveros, J.C. Sanabria

Technical University of Split, Split, Croatia

N. Godinovic, D. Lelas, K. Lelas, R. Plestina[3] D. Polic, I. Puljak

University of Split, Split, Croatia

Z. Antunovic, M. Dzelalija

Institute Rudjer Boskovic, Zagreb, Croatia

V. Brigljevic, S. Duric, K. Kadija, S. Morovic

University of Cyprus, Nicosia, Cyprus

A. Attikis, M. Galanti, J. Mousa, C. Nicolaou, F. Ptochos, P.A. Razis, H. Rykaczewski

Academy of Scientific Research and Technology of the Arab Republic of

Egypt, Egyptian Network of High Energy Physics, Cairo, Egypt

Y. Assran[4] M.A. Mahmoud[5]

National Institute of Chemical Physics and Biophysics, Tallinn, Estonia

A. Hektor, M. Kadastik, K. Kannike, M. Müntel, M. Raidal, L. Rebane

Department of Physics, University of Helsinki, Helsinki, Finland

V. Azzolini, P. Eerola

Helsinki Institute of Physics, Helsinki, Finland

S. Czellar, J. Härkönen, A. Heikkinen, V. Karimäki, R. Kinnunen, J. Klem, M.J. Kortelainen, T. Lampén, K. Lassila-Perini, S. Lehti, T. Lindén, P. Luukka, T. Mäenpää, E. Tuominen, J. Tuominiemi, E. Tuovinen, D. Ungaro, L. Wendland

Lappeenranta University of Technology, Lappeenranta, Finland

K. Banzuzi, A. Korpela, T. Tuuva

Laboratoire d'Annecy-le-Vieux de Physique des Particules, IN2P3-CNRS, Annecy-le-Vieux, France

D. Sillou

DSM/IRFU, CEA/Saclay, Gif-sur-Yvette, France

M. Besancon, M. Dejardin, D. Denegri, B. Fabbro, J.L. Faure, F. Ferri, S. Ganjour, F.X. Gentit, A. Givernaud, P. Gras, G. Hamel de Monchenault, P. Jarry, E. Locci, J. Malcles, M. Marionneau, L. Millischer, J. Rander, A. Rosowsky, I. Shreyber, M. Titov, P. Verrecchia

Laboratoire Leprince-Ringuet, Ecole Polytechnique, IN2P3-CNRS, Palaiseau, France

S. Baffioni, F. Beaudette, L. Bianchini, M. Bluj[6], C. Broutin, P. Busson, C. Char-

lot, T. Dahms, L. Dobrzynski, R. Granier de Cassagnac, M. Haguenauer, P. Miné, C. Mironov, C. Ochando, P. Paganini, D. Sabes, R. Salerno, Y. Sirois, C. Thiebaux, B. Wyslouch[7], A. Zabi

Institut Pluridisciplinaire Hubert Curien, Université de Strasbourg, Université de Haute Alsace Mulhouse, CNRS/IN2P3, Strasbourg, France

J.-L. Agram[8], J. Andrea, A. Besson, D. Bloch, D. Bodin, J.-M. Brom, M. Cardaci, E.C. Chabert, C. Collard, E. Conte[8], F. Drouhin[8], C. Ferro, J.-C. Fontaine[8], D. Gelé, U. Goerlach, S. Greder, P. Juillot, M. Karim[8], A.-C. Le Bihan, Y. Mikami, P. Van Hove

Centre de Calcul de l'Institut National de Physique Nucleaire et de Physique des Particules (IN2P3), Villeurbanne, France

F. Fassi, D. Mercier

Université de Lyon, Université Claude Bernard Lyon 1, CNRS-IN2P3, Institut de Physique Nucléaire de Lyon, Villeurbanne, France

C. Baty, N. Beaupere, M. Bedjidian, O. Bondu, G. Boudoul, D. Boumediene, H. Brun, N. Chanon, R. Chierici, D. Contardo, P. Depasse, H. El Mamouni, A. Falkiewicz, J. Fay, S. Gascon, B. Ille, T. Kurca, T. Le Grand, M. Lethuillier, L. Mirabito, S. Perries, V. Sordini, S. Tosi, Y. Tschudi, P. Verdier, H. Xiao

E. Andronikashvili Institute of Physics, Academy of Science, Tbilisi, Georgia

V. Roinishvili

RWTH Aachen University, I. Physikalisches Institut, Aachen, Germany

G. Anagnostou, M. Edelhoff, L. Feld, N. Heracleous, O. Hindrichs, R. Jussen,

K. Klein, J. Merz, N. Mohr, A. Ostapchuk, A. Perieanu, F. Raupach, J. Sammet, S. Schael, D. Sprenger, H. Weber, M. Weber, B. Wittmer

RWTH Aachen University, III. Physikalisches Institut A, Aachen, Germany

M. Ata, W. Bender, M. Erdmann, J. Frangenheim, T. Hebbeker, A. Hinzmann, K. Hoepfner, C. Hof, T. Klimkovich, D. Klingebiel, P. Kreuzer, D. Lanske[†], C. Magass, G. Masetti, M. Merschmeyer, A. Meyer, P. Papacz, H. Pieta, H. Reithler, S.A. Schmitz, L. Sonnenschein, J. Steggemann, D. Teyssier

RWTH Aachen University, III. Physikalisches Institut B, Aachen, Germany

M. Bontenackels, M. Davids, M. Duda, G. Flügge, H. Geenen, M. Giffels, W. Haj Ahmad, D. Heydhausen, T. Kress, Y. Kuessel, A. Linn, A. Nowack, L. Perchalla, O. Pooth, J. Rennefeld, P. Sauerland, A. Stahl, M. Thomas, D. Tornier, M.H. Zoeller

Deutsches Elektronen-Synchrotron, Hamburg, Germany

M. Aldaya Martin, W. Behrenhoff, U. Behrens, M. Bergholz[9], K. Borras, A. Cakir, A. Campbell, E. Castro, D. Dammann, G. Eckerlin, D. Eckstein, A. Flossdorf, G. Flucke, A. Geiser, I. Glushkov, J. Hauk, H. Jung, M. Kasemann, I. Katkov, P. Katsas, C. Kleinwort, H. Kluge, A. Knutsson, D. Krücker, E. Kuznetsova, W. Lange, W. Lohmann[9] R. Mankel, M. Marienfeld, I.-A. Melzer-Pellmann, A.B. Meyer, J. Mnich, A. Mussgiller, J. Olzem, A. Parenti, A. Raspereza, A. Raval, R. Schmidt[9], T. Schoerner-Sadenius, N. Sen, M. Stein, J. Tomaszewska, D. Volyanskyy, R. Walsh, C. Wissing

University of Hamburg, Hamburg, Germany

C. Autermann, S. Bobrovskyi, J. Draeger, H. Enderle, U. Gebbert, K. Kaschube, G. Kaussen, R. Klanner, J. Lange, B. Mura, S. Naumann-Emme, F. Nowak, N. Pietsch, C. Sander, H. Schettler, P. Schleper, M. Schröder, T. Schum, J. Schwandt, A.K. Srivastava, H. Stadie, G. Steinbrück, J. Thomsen, R. Wolf

Institut für Experimentelle Kernphysik, Karlsruhe, Germany

J. Bauer, V. Buege, T. Chwalek, W. De Boer, A. Dierlamm, G. Dirkes, M. Feindt, J. Gruschke, C. Hackstein, F. Hartmann, S.M. Heindl, M. Heinrich, H. Held, K.H. Hoffmann, S. Honc, T. Kuhr, D. Martschei, S. Mueller, Th. Müller, M. Niegel, O. Oberst, A. Oehler, J. Ott, T. Peiffer, D. Piparo, G. Quast, K. Rabbertz, F. Ratnikov, M. Renz, C. Saout, A. Scheurer, P. Schieferdecker, F.-P. Schilling, G. Schott, H.J. Simonis, F.M. Stober, D. Troendle, J. Wagner-Kuhr, M. Zeise, V. Zhukov[10], E.B. Ziebarth

Institute of Nuclear Physics "Demokritos", Aghia Paraskevi, Greece

G. Daskalakis, T. Geralis, S. Kesisoglou, A. Kyriakis, D. Loukas, I. Manolakos, A. Markou, C. Markou, C. Mavrommatis, E. Petrakou

University of Athens, Athens, Greece

L. Gouskos, T.J. Mertzimekis, A. Panagiotou[1]

University of Ioánnina, Ioánnina, Greece

I. Evangelou, C. Foudas, P. Kokkas, N. Manthos, I. Papadopoulos, V. Patras, F.A. Triantis

KFKI Research Institute for Particle and Nuclear Physics, Budapest, Hungary

A. Aranyi, G. Bencze, L. Boldizsar, G. Debreczeni, C. Hajdu[1], D. Horvath[11],

A. Kapusi, K. Krajczar[12], A. Laszlo, F. Sikler, G. Vesztergombi[12]

Institute of Nuclear Research ATOMKI, Debrecen, Hungary

N. Beni, J. Molnar, J. Palinkas, Z. Szillasi, V. Veszpremi

University of Debrecen, Debrecen, Hungary

P. Raics, Z.L. Trocsanyi, B. Ujvari

Panjab University, Chandigarh, India

S. Bansal, S.B. Beri, V. Bhatnagar, N. Dhingra, M. Jindal, M. Kaur, J.M. Kohli, M.Z. Mehta, N. Nishu, L.K. Saini, A. Sharma, A.P. Singh, J.B. Singh, S.P. Singh

University of Delhi, Delhi, India

S. Ahuja, S. Bhattacharya, B.C. Choudhary, P. Gupta, S. Jain, S. Jain, A. Kumar, R.K. Shivpuri

Bhabha Atomic Research Centre, Mumbai, India

R.K. Choudhury, D. Dutta, S. Kailas, S.K. Kataria, A.K. Mohanty[1], L.M. Pant, P. Shukla, P. Suggisetti

Tata Institute of Fundamental Research - EHEP, Mumbai, India

T. Aziz, M. Guchait[13], A. Gurtu, M. Maity[14], D. Majumder, G. Majumder, K. Mazumdar, G.B. Mohanty, A. Saha, K. Sudhakar, N. Wickramage

Tata Institute of Fundamental Research - HECR, Mumbai, India

S. Banerjee, S. Dugad, N.K. Mondal

Institute for Studies in Theoretical Physics & Mathematics (IPM), Tehran, Iran

H. Arfaei, H. Bakhshiansohi, S.M. Etesami, A. Fahim, M. Hashemi, A. Jafari, M. Khakzad, A. Mohammadi, M. Mohammadi Najafabadi, S. Paktinat Mehdia-

badi, B. Safarzadeh, M. Zeinali

INFN Sezione di Bari [a], Università di Bari [b], Politecnico di Bari [c], Bari, Italy

M. Abbrescia[a,b], L. Barbone[a,b], C. Calabria[a,b], A. Colaleo[a], D. Creanza[a,c], N. De Filippis[a,c], M. De Palma[a,b], A. Dimitrov[a], L. Fiore[a], G. Iaselli[a,c], L. Lusito[a,b,[1]], G. Maggi[a,c], M. Maggi[a], N. Manna[a,b], B. Marangelli[a,b], S. My[a,c], S. Nuzzo[a,b], N. Pacifico[a,b], G.A. Pierro[a], A. Pompili[a,b], G. Pugliese[a,c], F. Romano[a,c], G. Roselli[a,b], G. Selvaggi[a,b], L. Silvestris[a], R. Trentadue[a], S. Tupputi[a,b], G. Zito[a]

INFN Sezione di Bologna [a], Università di Bologna [b], Bologna, Italy

G. Abbiendi[a], A.C. Benvenuti[a], D. Bonacorsi[a], S. Braibant-Giacomelli[a,b], P. Capiluppi[a,b], A. Castro[a,b], F.R. Cavallo[a], M. Cuffiani[a,b], G.M. Dallavalle[a], F. Fabbri[a], A. Fanfani[a,b], D. Fasanella[a], P. Giacomelli[a], M. Giunta[a], S. Marcellini[a], M. Meneghelli[a,b], A. Montanari[a], F.L. Navarria[a,b], F. Odorici[a], A. Perrotta[a], F. Primavera[a], A.M. Rossi[a,b], T. Rovelli[a,b], G. Siroli[a,b], R. Travaglini[a,b]

INFN Sezione di Catania [a], Università di Catania [b], Catania, Italy

S. Albergo[a,b], G. Cappello[a,b], M. Chiorboli[a,b,[1]], S. Costa[a,b], A. Tricomi[a,b], C. Tuve[a]

INFN Sezione di Firenze [a], Università di Firenze [b], Firenze, Italy

G. Barbagli[a], V. Ciulli[a,b], C. Civinini[a], R. D'Alessandro[a,b], E. Focardi[a,b], S. Frosali[a,b], E. Gallo[a], C. Genta[a], P. Lenzi[a,b], M. Meschini[a], S. Paoletti[a], G. Sguazzoni[a], A. Tropiano[a,[1]]

INFN Laboratori Nazionali di Frascati, Frascati, Italy

L. Benussi, S. Bianco, S. Colafranceschi[15], F. Fabbri, D. Piccolo

INFN Sezione di Genova, Genova, Italy

P. Fabbricatore, R. Musenich

INFN Sezione di Milano-Biccoca [a], Università di Milano-Bicocca [b], Milano, Italy

A. Benaglia[a,b], G.B. Cerati[a,b], F. De Guio[a,b,[1]], L. Di Matteo[a,b], A. Ghezzi[a,b,[1]], M. Malberti[a,b], S. Malvezzi[a], A. Martelli[a,b], A. Massironi[a,b], D. Menasce[a], L. Moroni[a], M. Paganoni[a,b], D. Pedrini[a], S. Ragazzi[a,b], N. Redaelli[a], S. Sala[a], T. Tabarelli de Fatis[a,b], V. Tancini[a,b]

INFN Sezione di Napoli [a], Università di Napoli "Federico II" [b], Napoli, Italy

S. Buontempo[a], C.A. Carrillo Montoya[a], A. Cimmino[a,b], A. De Cosa[a,b], M. De Gruttola[a,b], F. Fabozzi[a,[16]], A.O.M. Iorio[a], L. Lista[a], M. Merola[a,b], P. Noli[a,b], P. Paolucci[a]

INFN Sezione di Padova [a], Università di Padova [b], Università di Trento (Trento) [c], Padova, Italy

P. Azzi[a], N. Bacchetta[a], P. Bellan[a,b], D. Bisello[a,b], A. Branca[a], R. Carlin[a,b], P. Checchia[a], M. De Mattia[a,b], T. Dorigo[a], U. Dosselli[a], F. Fanzago[a], F. Gasparini[a,b], U. Gasparini[a,b], P. Giubilato[a,b], A. Gresele[a,c], S. Lacaprara[a,[17]], I. Lazzizzera[a,c], M. Margoni[a,b], M. Mazzucato[a], A.T. Meneguzzo[a,b], M. Nespolo[a], L. Perrozzi[a,[1]], N. Pozzobon[a,b], P. Ronchese[a,b], F. Simonetto[a,b], E. Torassa[a], M. Tosi[a,b], S. Vanini[a,b], P. Zotto[a,b], G. Zumerle[a,b]

INFN Sezione di Pavia [a], Università di Pavia [b], Pavia, Italy

P. Baesso[a,b], U. Berzano[a], C. Riccardi[a,b], P. Torre[a,b], P. Vitulo[a,b], C. Viviani[a,b]

INFN Sezione di Perugia [a], Università di Perugia [b], Perugia, Italy

M. Biasini[a,b], G.M. Bilei[a], B. Caponeri[a,b], L. Fanò[a,b], P. Lariccia[a,b], A. Lucaroni[a,b,[1]],

G. Mantovani[a,b], M. Menichelli[a], A. Nappi[a,b], A. Santocchia[a,b], L. Servoli[a], S. Taroni[a,b], M. Valdata[a,b], R. Volpe[a,b,[1]]

INFN Sezione di Pisa [a], Università di Pisa [b], Scuola Normale Superiore di Pisa [c], Pisa, Italy

P. Azzurri[a,c], G. Bagliesi[a], J. Bernardini[a,b], T. Boccali[a,[1]], G. Broccolo[a,c], R. Castaldi[a], R.T. D'Agnolo[a,c], R. Dell'Orso[a], F. Fiori[a,b], L. Foà[a,c], A. Giassi[a], A. Kraan[a], F. Ligabue[a,c], T. Lomtadze[a], L. Martini[a], A. Messineo[a,b], F. Palla[a], F. Palmonari[a], S. Sarkar[a,c], G. Segneri[a], A.T. Serban[a], P. Spagnolo[a], R. Tenchini[a], G. Tonelli[a,b,[1]], A. Venturi[a,[1]], P.G. Verdini[a]

INFN Sezione di Roma [a], Università di Roma "La Sapienza" [b], Roma, Italy

L. Barone[a,b], F. Cavallari[a], D. Del Re[a,b], E. Di Marco[a,b], M. Diemoz[a], D. Franci[a,b], M. Grassi[a], E. Longo[a,b], G. Organtini[a,b], A. Palma[a,b], F. Pandolfi[a,b,[1]], R. Paramatti[a], S. Rahatlou[a,b]

INFN Sezione di Torino [a], Università di Torino [b], Università del Piemonte Orientale (Novara) [c], Torino, Italy

N. Amapane[a,b], R. Arcidiacono[a,c], S. Argiro[a,b], M. Arneodo[a,c], C. Biino[a], C. Botta[a,b,[1]], N. Cartiglia[a], R. Castello[a,b], M. Costa[a,b], N. Demaria[a], A. Graziano[a,b,[1]], C. Mariotti[a], M. Marone[a,b], S. Maselli[a], E. Migliore[a,b], G. Mila[a,b], V. Monaco[a,b], M. Musich[a,b], M.M. Obertino[a,c], N. Pastrone[a], M. Pelliccioni[a,b,[1]], A. Romero[a,b], M. Ruspa[a,c], R. Sacchi[a,b], V. Sola[a,b], A. Solano[a,b], A. Staiano[a], D. Trocino[a,b], A. Vilela Pereira[a,b,[1]]

INFN Sezione di Trieste [a], Università di Trieste [b], Trieste, Italy

F. Ambroglini[a,b], S. Belforte[a], F. Cossutti[a], G. Della Ricca[a,b], B. Gobbo[a], D. Montanino[a,b],

A. Penzo[a]

Kangwon National University, Chunchon, Korea

S.G. Heo

Kyungpook National University, Daegu, Korea

S. Chang, J. Chung, D.H. Kim, G.N. Kim, J.E. Kim, D.J. Kong, H. Park, D. Son, D.C. Son

Chonnam National University, Institute for Universe and Elementary Particles, Kwangju, Korea

Zero Kim, J.Y. Kim, S. Song

Korea University, Seoul, Korea

S. Choi, B. Hong, M. Jo, H. Kim, J.H. Kim, T.J. Kim, K.S. Lee, D.H. Moon, S.K. Park, H.B. Rhee, E. Seo, S. Shin, K.S. Sim

University of Seoul, Seoul, Korea

M. Choi, S. Kang, H. Kim, C. Park, I.C. Park, S. Park, G. Ryu

Sungkyunkwan University, Suwon, Korea

Y. Choi, Y.K. Choi, J. Goh, J. Lee, S. Lee, H. Seo, I. Yu

Vilnius University, Vilnius, Lithuania

M.J. Bilinskas, I. Grigelionis, M. Janulis, D. Martisiute, P. Petrov, T. Sabonis

Centro de Investigacion y de Estudios Avanzados del IPN, Mexico City, Mexico

H. Castilla Valdez, E. De La Cruz Burelo, R. Lopez-Fernandez, A. Sánchez Hernández, L.M. Villasenor-Cendejas

Universidad Iberoamericana, Mexico City, Mexico

S. Carrillo Moreno, F. Vazquez Valencia

Benemerita Universidad Autonoma de Puebla, Puebla, Mexico

H.A. Salazar Ibarguen

Universidad Autónoma de San Luis Potosí, San Luis Potosí, Mexico

E. Casimiro Linares, A. Morelos Pineda, M.A. Reyes-Santos

University of Auckland, Auckland, New Zealand

P. Allfrey, D. Krofcheck

University of Canterbury, Christchurch, New Zealand

P.H. Butler, R. Doesburg, H. Silverwood

National Centre for Physics, Quaid-I-Azam University, Islamabad, Pakistan

M. Ahmad, I. Ahmed, M.I. Asghar, H.R. Hoorani, W.A. Khan, T. Khurshid, S. Qazi

Institute of Experimental Physics, Faculty of Physics, University of Warsaw, Warsaw, Poland

M. Cwiok, W. Dominik, K. Doroba, A. Kalinowski, M. Konecki, J. Krolikowski

Soltan Institute for Nuclear Studies, Warsaw, Poland

T. Frueboes, R. Gokieli, M. Górski, M. Kazana, K. Nawrocki, K. Romanowska-Rybinska, M. Szleper, G. Wrochna, P. Zalewski

Laboratório de Instrumentação e Física Experimental de Partículas, Lisboa, Portugal

N. Almeida, A. David, P. Faccioli, P.G. Ferreira Parracho, M. Gallinaro, P. Martins, P. Musella, A. Nayak, P.Q. Ribeiro, J. Seixas, P. Silva, J. Varela[1], H.K. Wöhri

Joint Institute for Nuclear Research, Dubna, Russia

I. Belotelov, P. Bunin, M. Finger, M. Finger Jr., I. Golutvin, A. Kamenev, V. Karjavin, G. Kozlov, A. Lanev, P. Moisenz, V. Palichik, V. Perelygin, S. Shmatov, V. Smirnov, A. Volodko, A. Zarubin

Petersburg Nuclear Physics Institute, Gatchina (St Petersburg), Russia

N. Bondar, V. Golovtsov, Y. Ivanov, V. Kim, P. Levchenko, V. Murzin, V. Oreshkin, I. Smirnov, V. Sulimov, L. Uvarov, S. Vavilov, A. Vorobyev

Institute for Nuclear Research, Moscow, Russia

Yu. Andreev, S. Gninenko, N. Golubev, M. Kirsanov, N. Krasnikov, V. Matveev, A. Pashenkov, A. Toropin, S. Troitsky

Institute for Theoretical and Experimental Physics, Moscow, Russia

V. Epshteyn, V. Gavrilov, V. Kaftanov†, M. Kossov[1], A. Krokhotin, N. Lychkovskaya, G. Safronov, S. Semenov, V. Stolin, E. Vlasov, A. Zhokin

Moscow State University, Moscow, Russia

E. Boos, M. Dubinin[18], L. Dudko, A. Ershov, A. Gribushin, O. Kodolova, I. Lokhtin, S. Obraztsov, S. Petrushanko, L. Sarycheva, V. Savrin, A. Snigirev

P.N. Lebedev Physical Institute, Moscow, Russia

V. Andreev, M. Azarkin, I. Dremin, M. Kirakosyan, S.V. Rusakov, A. Vinogradov

State Research Center of Russian Federation, Institute for High Energy Physics, Protvino, Russia

I. Azhgirey, S. Bitioukov, V. Grishin[1], V. Kachanov, D. Konstantinov, A. Korablev, V. Krychkine, V. Petrov, R. Ryutin, S. Slabospitsky, A. Sobol, L. Tourtchanovitch, S. Troshin, N. Tyurin, A. Uzunian, A. Volkov

University of Belgrade, Faculty of Physics and Vinca Institute of Nuclear Sciences, Belgrade, Serbia

P. Adzic[19], M. Djordjevic, D. Krpic[19], J. Milosevic

Centro de Investigaciones Energéticas Medioambientales y Tecnológicas (CIEMAT), Madrid, Spain

M. Aguilar-Benitez, J. Alcaraz Maestre, P. Arce, C. Battilana, E. Calvo, M. Cepeda, M. Cerrada, N. Colino, B. De La Cruz, C. Diez Pardos, C. Fernandez Bedoya, J.P. Fernández Ramos, A. Ferrando, J. Flix, M.C. Fouz, P. Garcia-Abia, O. Gonzalez Lopez, S. Goy Lopez, J.M. Hernandez, M.I. Josa, G. Merino, J. Puerta Pelayo, I. Redondo, L. Romero, J. Santaolalla, M.S. Soares, C. Willmott

Universidad Autónoma de Madrid, Madrid, Spain

C. Albajar, G. Codispoti, J.F. de Trocóniz

Universidad de Oviedo, Oviedo, Spain

J. Cuevas, J. Fernandez Menendez, S. Folgueras, I. Gonzalez Caballero, L. Lloret Iglesias, J.M. Vizan Garcia

Instituto de Física de Cantabria (IFCA), CSIC-Universidad de Cantabria, Santander, Spain

J.A. Brochero Cifuentes, I.J. Cabrillo, A. Calderon, M. Chamizo Llatas, S.H. Chuang, J. Duarte Campderros, M. Felcini[20], M. Fernandez, G. Gomez, J. Gonzalez Sanchez, C. Jorda, P. Lobelle Pardo, A. Lopez Virto, J. Marco, R. Marco, C. Martinez Rivero, F. Matorras, F.J. Munoz Sanchez, J. Piedra Gomez[21], T. Rodrigo, A. Ruiz Jimeno, L. Scodellaro, M. Sobron Sanudo, I. Vila, R. Vilar Cortabitarte

CERN, European Organization for Nuclear Research, Geneva, Switzer-

land

D. Abbaneo, E. Auffray, G. Auzinger, P. Baillon, A.H. Ball, D. Barney, A.J. Bell[22], D. Benedetti, C. Bernet[3], W. Bialas, P. Bloch, A. Bocci, S. Bolognesi, H. Breuker, G. Brona, K. Bunkowski, T. Camporesi, E. Cano, G. Cerminara, T. Christiansen, J.A. Coarasa Perez, B. Curé, D. D'Enterria, A. De Roeck, F. Duarte Ramos, A. Elliott-Peisert, B. Frisch, W. Funk, A. Gaddi, S. Gennai, G. Georgiou, H. Gerwig, D. Gigi, K. Gill, D. Giordano, F. Glege, R. Gomez-Reino Garrido, M. Gouzevitch, P. Govoni, S. Gowdy, L. Guiducci, M. Hansen, J. Harvey, J. Hegeman, B. Hegner, C. Henderson, G. Hesketh, H.F. Hoffmann, A. Honma, V. Innocente, P. Janot, E. Karavakis, P. Lecoq, C. Leonidopoulos, C. Lourenço, A. Macpherson, T. Mäki, L. Malgeri, M. Mannelli, L. Masetti, F. Meijers, S. Mersi, E. Meschi, R. Moser, M.U. Mozer, M. Mulders, E. Nesvold[1], M. Nguyen, T. Orimoto, L. Orsini, E. Perez, A. Petrilli, A. Pfeiffer, M. Pierini, M. Pimiä, G. Polese, A. Racz, G. Rolandi[23], T. Rommerskirchen, C. Rovelli[24], M. Rovere, H. Sakulin, C. Schäfer, C. Schwick, I. Segoni, A. Sharma, P. Siegrist, M. Simon, P. Sphicas[25], D. Spiga, M. Spiropulu[18], F. Stöckli, M. Stoye, P. Tropea, A. Tsirou, A. Tsyganov, G.I. Veres[12], P. Vichoudis, M. Voutilainen, W.D. Zeuner

Paul Scherrer Institut, Villigen, Switzerland

W. Bertl, K. Deiters, W. Erdmann, K. Gabathuler, R. Horisberger, Q. Ingram, H.C. Kaestli, S. König, D. Kotlinski, U. Langenegger, F. Meier, D. Renker, T. Rohe, J. Sibille[26], A. Starodumov[27]

Institute for Particle Physics, ETH Zurich, Zurich, Switzerland

P. Bortignon, L. Caminada[28], Z. Chen, S. Cittolin, G. Dissertori, M. Dittmar, J. Eu-

gster, K. Freudenreich, C. Grab, A. Hervé, W. Hintz, P. Lecomte, W. Lustermann, C. Marchica[28], P. Martinez Ruiz del Arbol, P. Meridiani, P. Milenovic[29], F. Moortgat, P. Nef, F. Nessi-Tedaldi, L. Pape, F. Pauss, T. Punz, A. Rizzi, F.J. Ronga, M. Rossini, L. Sala, A.K. Sanchez, M.-C. Sawley, B. Stieger, L. Tauscher†, A. Thea, K. Theofilatos, D. Treille, C. Urscheler, R. Wallny[20], M. Weber, L. Wehrli, J. Weng

Universität Zürich, Zurich, Switzerland

E. Aguiló, C. Amsler, V. Chiochia, S. De Visscher, C. Favaro, M. Ivova Rikova, B. Millan Mejias, C. Regenfus, P. Robmann, A. Schmidt, H. Snoek, L. Wilke

National Central University, Chung-Li, Taiwan

Y.H. Chang, K.H. Chen, W.T. Chen, S. Dutta, A. Go, C.M. Kuo, S.W. Li, W. Lin, M.H. Liu, Z.K. Liu, Y.J. Lu, J.H. Wu, S.S. Yu

National Taiwan University (NTU), Taipei, Taiwan

P. Bartalini, P. Chang, Y.H. Chang, Y.W. Chang, Y. Chao, K.F. Chen, W.-S. Hou, Y. Hsiung, K.Y. Kao, Y.J. Lei, R.-S. Lu, J.G. Shiu, Y.M. Tzeng, M. Wang

Cukurova University, Adana, Turkey

A. Adiguzel, M.N. Bakirci, S. Cerci[30], C. Dozen, I. Dumanoglu, E. Eskut, S. Girgis, G. Gokbulut, Y. Guler, E. Gurpinar, I. Hos, E.E. Kangal, T. Karaman, A. Kayis Topaksu, A. Nart, G. Onengut, K. Ozdemir, S. Ozturk, A. Polatoz, K. Sogut[31], B. Tali, H. Topakli, D. Uzun, L.N. Vergili, M. Vergili, C. Zorbilmez

Middle East Technical University, Physics Department, Ankara, Turkey

I.V. Akin, T. Aliev, S. Bilmis, M. Deniz, H. Gamsizkan, A.M. Guler, K. Ocalan, A. Ozpineci, M. Serin, R. Sever, U.E. Surat, E. Yildirim, M. Zeyrek

Bogazici University, Istanbul, Turkey

M. Deliomeroglu, D. Demir[32], E. Gülmez, A. Halu, B. Isildak, M. Kaya[33], O. Kaya[33], S. Ozkorucuklu[34], N. Sonmez[35]

National Scientific Center, Kharkov Institute of Physics and Technology, Kharkov, Ukraine

L. Levchuk

University of Bristol, Bristol, United Kingdom

P. Bell, F. Bostock, J.J. Brooke, T.L. Cheng, E. Clement, D. Cussans, R. Frazier, J. Goldstein, M. Grimes, M. Hansen, D. Hartley, G.P. Heath, H.F. Heath, B. Huckvale, J. Jackson, L. Kreczko, S. Metson, D.M. Newbold[36], K. Nirunpong, A. Poll, S. Senkin, V.J. Smith, S. Ward

Rutherford Appleton Laboratory, Didcot, United Kingdom

L. Basso, K.W. Bell, A. Belyaev, C. Brew, R.M. Brown, B. Camanzi, D.J.A. Cockerill, J.A. Coughlan, K. Harder, S. Harper, B.W. Kennedy, E. Olaiya, D. Petyt, B.C. Radburn-Smith, C.H. Shepherd-Themistocleous, I.R. Tomalin, W.J. Womersley, S.D. Worm

Imperial College, London, United Kingdom

R. Bainbridge, G. Ball, J. Ballin, R. Beuselinck, O. Buchmuller, D. Colling, N. Cripps, M. Cutajar, G. Davies, M. Della Negra, J. Fulcher, D. Futyan, A. Guneratne Bryer, G. Hall, Z. Hatherell, J. Hays, G. Iles, G. Karapostoli, L. Lyons, A.-M. Magnan, J. Marrouche, R. Nandi, J. Nash, A. Nikitenko[27], A. Papageorgiou, M. Pesaresi, K. Petridis, M. Pioppi[37], D.M. Raymond, N. Rompotis, A. Rose, M.J. Ryan, C. Seez, P. Sharp, A. Sparrow, A. Tapper, S. Tourneur, M. Vazquez Acosta, T. Virdee,

S. Wakefield, D. Wardrope, T. Whyntie

Brunel University, Uxbridge, United Kingdom

M. Barrett, M. Chadwick, J.E. Cole, P.R. Hobson, A. Khan, P. Kyberd, D. Leslie, W. Martin, I.D. Reid, L. Teodorescu

Baylor University, Waco, USA

K. Hatakeyama

Boston University, Boston, USA

T. Bose, E. Carrera Jarrin, A. Clough, C. Fantasia, A. Heister, J. St. John, P. Lawson, D. Lazic, J. Rohlf, D. Sperka, L. Sulak

Brown University, Providence, USA

A. Avetisyan, S. Bhattacharya, J.P. Chou, D. Cutts, A. Ferapontov, U. Heintz, S. Jabeen, G. Kukartsev, G. Landsberg, M. Narain, D. Nguyen, M. Segala, T. Speer, K.V. Tsang

University of California, Davis, Davis, USA

M.A. Borgia, R. Breedon, M. Calderon De La Barca Sanchez, D. Cebra, S. Chauhan, M. Chertok, J. Conway, P.T. Cox, J. Dolen, R. Erbacher, E. Friis, W. Ko, A. Kopecky, R. Lander, H. Liu, S. Maruyama, T. Miceli, M. Nikolic, D. Pellett, J. Robles, T. Schwarz, M. Searle, J. Smith, M. Squires, M. Tripathi, R. Vasquez Sierra, C. Veelken

University of California, Los Angeles, Los Angeles, USA

V. Andreev, K. Arisaka, D. Cline, R. Cousins, A. Deisher, J. Duris, S. Erhan[1], C. Farrell, J. Hauser, M. Ignatenko, C. Jarvis, C. Plager, G. Rakness, P. Schlein†, J. Tucker, V. Valuev

University of California, Riverside, Riverside, USA

J. Babb, R. Clare, J. Ellison, J.W. Gary, F. Giordano, G. Hanson, G.Y. Jeng, S.C. Kao, F. Liu, H. Liu, A. Luthra, H. Nguyen, G. Pasztor[38], A. Satpathy, B.C. Shen†, R. Stringer, J. Sturdy, S. Sumowidagdo, R. Wilken, S. Wimpenny

University of California, San Diego, La Jolla, USA

W. Andrews, J.G. Branson, E. Dusinberre, D. Evans, F. Golf, A. Holzner, R. Kelley, M. Lebourgeois, J. Letts, B. Mangano, J. Muelmenstaedt, S. Padhi, C. Palmer, G. Petrucciani, H. Pi, M. Pieri, R. Ranieri, M. Sani, V. Sharma[1], S. Simon, Y. Tu, A. Vartak, F. Würthwein, A. Yagil

University of California, Santa Barbara, Santa Barbara, USA

D. Barge, R. Bellan, C. Campagnari, M. D'Alfonso, T. Danielson, K. Flowers, P. Geffert, J. Incandela, C. Justus, P. Kalavase, S.A. Koay, D. Kovalskyi, V. Krutelyov, S. Lowette, N. Mccoll, V. Pavlunin, F. Rebassoo, J. Ribnik, J. Richman, R. Rossin, D. Stuart, W. To, J.R. Vlimant

California Institute of Technology, Pasadena, USA

A. Bornheim, J. Bunn, Y. Chen, M. Gataullin, D. Kcira, V. Litvine, Y. Ma, A. Mott, H.B. Newman, C. Rogan, V. Timciuc, P. Traczyk, J. Veverka, R. Wilkinson, Y. Yang, R.Y. Zhu

Carnegie Mellon University, Pittsburgh, USA

B. Akgun, R. Carroll, T. Ferguson, Y. Iiyama, D.W. Jang, S.Y. Jun, Y.F. Liu, M. Paulini, J. Russ, N. Terentyev, H. Vogel, I. Vorobiev

University of Colorado at Boulder, Boulder, USA

J.P. Cumalat, M.E. Dinardo, B.R. Drell, C.J. Edelmaier, W.T. Ford, B. Heyburn,

E. Luiggi Lopez, U. Nauenberg, J.G. Smith, K. Stenson, K.A. Ulmer, S.R. Wagner, S.L. Zang

Cornell University, Ithaca, USA

L. Agostino, J. Alexander, A. Chatterjee, S. Das, N. Eggert, L.J. Fields, L.K. Gibbons, B. Heltsley, W. Hopkins, A. Khukhunaishvili, B. Kreis, V. Kuznetsov, G. Nicolas Kaufman, J.R. Patterson, D. Puigh, D. Riley, A. Ryd, X. Shi, W. Sun, W.D. Teo, J. Thom, J. Thompson, J. Vaughan, Y. Weng, L. Winstrom, P. Wittich

Fairfield University, Fairfield, USA

A. Biselli, G. Cirino, D. Winn

Fermi National Accelerator Laboratory, Batavia, USA

S. Abdullin, M. Albrow, J. Anderson, G. Apollinari, M. Atac, J.A. Bakken, S. Banerjee, L.A.T. Bauerdick, A. Beretvas, J. Berryhill, P.C. Bhat, I. Bloch, F. Borcherding, K. Burkett, J.N. Butler, V. Chetluru, H.W.K. Cheung, F. Chlebana, S. Cihangir, M. Demarteau, D.P. Eartly, V.D. Elvira, S. Esen, I. Fisk, J. Freeman, Y. Gao, E. Gottschalk, D. Green, K. Gunthoti, O. Gutsche, A. Hahn, J. Hanlon, R.M. Harris, J. Hirschauer, B. Hooberman, E. James, H. Jensen, M. Johnson, U. Joshi, R. Khatiwada, B. Kilminster, B. Klima, K. Kousouris, S. Kunori, S. Kwan, P. Limon, R. Lipton, J. Lykken, K. Maeshima, J.M. Marraffino, D. Mason, P. McBride, T. McCauley, T. Miao, K. Mishra, S. Mrenna, Y. Musienko[39], C. Newman-Holmes, V. O'Dell, S. Popescu[40], R. Pordes, O. Prokofyev, N. Saoulidou, E. Sexton-Kennedy, S. Sharma, A. Soha, W.J. Spalding, L. Spiegel, P. Tan, L. Taylor, S. Tkaczyk, L. Uplegger, E.W. Vaandering, R. Vidal, J. Whitmore, W. Wu, F. Yang, F. Yumiceva, J.C. Yun

University of Florida, Gainesville, USA

D. Acosta, P. Avery, D. Bourilkov, M. Chen, G.P. Di Giovanni, D. Dobur, A. Drozdetskiy, R.D. Field, M. Fisher, Y. Fu, I.K. Furic, J. Gartner, S. Goldberg, B. Kim, S. Klimenko, J. Konigsberg, A. Korytov, A. Kropivnitskaya, T. Kypreos, K. Matchev, G. Mitselmakher, L. Muniz, Y. Pakhotin, C. Prescott, R. Remington, M. Schmitt, B. Scurlock, P. Sellers, N. Skhirtladze, D. Wang, J. Yelton, M. Zakaria

Florida International University, Miami, USA

C. Ceron, V. Gaultney, L. Kramer, L.M. Lebolo, S. Linn, P. Markowitz, G. Martinez, J.L. Rodriguez

Florida State University, Tallahassee, USA

T. Adams, A. Askew, D. Bandurin, J. Bochenek, J. Chen, B. Diamond, S.V. Gleyzer, J. Haas, S. Hagopian, V. Hagopian, M. Jenkins, K.F. Johnson, H. Prosper, S. Sekmen, V. Veeraraghavan

Florida Institute of Technology, Melbourne, USA

M.M. Baarmand, B. Dorney, S. Guragain, M. Hohlmann, H. Kalakhety, R. Ralich, I. Vodopiyanov

University of Illinois at Chicago (UIC), Chicago, USA

M.R. Adams, I.M. Anghel, L. Apanasevich, Y. Bai, V.E. Bazterra, R.R. Betts, J. Callner, R. Cavanaugh, C. Dragoiu, E.J. Garcia-Solis, C.E. Gerber, D.J. Hofman, S. Khalatyan, F. Lacroix, C. O'Brien, C. Silvestre, A. Smoron, D. Strom, N. Varelas

The University of Iowa, Iowa City, USA

U. Akgun, E.A. Albayrak, B. Bilki, K. Cankocak[41], W. Clarida, F. Duru, C.K. Lae,

E. McCliment, J.-P. Merlo, H. Mermerkaya, A. Mestvirishvili, A. Moeller, J. Nachtman, C.R. Newsom, E. Norbeck, J. Olson, Y. Onel, F. Ozok, S. Sen, J. Wetzel, T. Yetkin, K. Yi

Johns Hopkins University, Baltimore, USA

B.A. Barnett, B. Blumenfeld, A. Bonato, C. Eskew, D. Fehling, G. Giurgiu, A.V. Gritsan, Z.J. Guo, G. Hu, P. Maksimovic, S. Rappoccio, M. Swartz, N.V. Tran, A. Whitbeck

The University of Kansas, Lawrence, USA

P. Baringer, A. Bean, G. Benelli, O. Grachov, M. Murray, D. Noonan, V. Radicci, S. Sanders, J.S. Wood, V. Zhukova

Kansas State University, Manhattan, USA

T. Bolton, I. Chakaberia, A. Ivanov, M. Makouski, Y. Maravin, S. Shrestha, I. Svintradze, Z. Wan

Lawrence Livermore National Laboratory, Livermore, USA

J. Gronberg, D. Lange, D. Wright

University of Maryland, College Park, USA

A. Baden, M. Boutemeur, S.C. Eno, D. Ferencek, J.A. Gomez, N.J. Hadley, R.G. Kellogg, M. Kirn, Y. Lu, A.C. Mignerey, K. Rossato, P. Rumerio, F. Santanastasio, A. Skuja, J. Temple, M.B. Tonjes, S.C. Tonwar, E. Twedt

Massachusetts Institute of Technology, Cambridge, USA

B. Alver, G. Bauer, J. Bendavid, W. Busza, E. Butz, I.A. Cali, M. Chan, V. Dutta, P. Everaerts, G. Gomez Ceballos, M. Goncharov, K.A. Hahn, P. Harris, Y. Kim, M. Klute, Y.-J. Lee, W. Li, C. Loizides, P.D. Luckey, T. Ma, S. Nahn, C. Paus,

D. Ralph, C. Roland, G. Roland, M. Rudolph, G.S.F. Stephans, K. Sumorok, K. Sung, E.A. Wenger, S. Xie, M. Yang, Y. Yilmaz, A.S. Yoon, M. Zanetti

University of Minnesota, Minneapolis, USA

P. Cole, S.I. Cooper, P. Cushman, B. Dahmes, A. De Benedetti, P.R. Dudero, G. Franzoni, J. Haupt, K. Klapoetke, Y. Kubota, J. Mans, V. Rekovic, R. Rusack, M. Sasseville, A. Singovsky

University of Mississippi, University, USA

L.M. Cremaldi, R. Godang, R. Kroeger, L. Perera, R. Rahmat, D.A. Sanders, D. Summers

University of Nebraska-Lincoln, Lincoln, USA

K. Bloom, S. Bose, J. Butt, D.R. Claes, A. Dominguez, M. Eads, J. Keller, T. Kelly, I. Kravchenko, J. Lazo-Flores, C. Lundstedt, H. Malbouisson, S. Malik, G.R. Snow

State University of New York at Buffalo, Buffalo, USA

U. Baur, A. Godshalk, I. Iashvili, A. Kharchilava, A. Kumar, S.P. Shipkowski, K. Smith

Northeastern University, Boston, USA

G. Alverson, E. Barberis, D. Baumgartel, O. Boeriu, M. Chasco, K. Kaadze, S. Reucroft, J. Swain, D. Wood, J. Zhang

Northwestern University, Evanston, USA

A. Anastassov, A. Kubik, N. Odell, R.A. Ofierzynski, B. Pollack, A. Pozdnyakov, M. Schmitt, S. Stoynev, M. Velasco, S. Won

University of Notre Dame, Notre Dame, USA

L. Antonelli, D. Berry, M. Hildreth, C. Jessop, D.J. Karmgard, J. Kolb, T. Kolberg,

K. Lannon, W. Luo, S. Lynch, N. Marinelli, D.M. Morse, T. Pearson, R. Ruchti, J. Slaunwhite, N. Valls, J. Warchol, M. Wayne, J. Ziegler

The Ohio State University, Columbus, USA

B. Bylsma, L.S. Durkin, J. Gu, C. Hill, P. Killewald, K. Kotov, T.Y. Ling, M. Rodenburg, G. Williams

Princeton University, Princeton, USA

N. Adam, E. Berry, P. Elmer, D. Gerbaudo, V. Halyo, P. Hebda, A. Hunt, J. Jones, E. Laird, D. Lopes Pegna, D. Marlow, T. Medvedeva, M. Mooney, J. Olsen, P. Piroué, X. Quan, H. Saka, D. Stickland, C. Tully, J.S. Werner, A. Zuranski

University of Puerto Rico, Mayaguez, USA

J.G. Acosta, X.T. Huang, A. Lopez, H. Mendez, S. Oliveros, J.E. Ramirez Vargas, A. Zatserklyaniy

Purdue University, West Lafayette, USA

E. Alagoz, V.E. Barnes, G. Bolla, L. Borrello, D. Bortoletto, A. Everett, A.F. Garfinkel, Z. Gecse, L. Gutay, Z. Hu, M. Jones, O. Koybasi, A.T. Laasanen, N. Leonardo, C. Liu, V. Maroussov, P. Merkel, D.H. Miller, N. Neumeister, K. Potamianos, I. Shipsey, D. Silvers, A. Svyatkovskiy, H.D. Yoo, J. Zablocki, Y. Zheng

Purdue University Calumet, Hammond, USA

P. Jindal, N. Parashar

Rice University, Houston, USA

C. Boulahouache, V. Cuplov, K.M. Ecklund, F.J.M. Geurts, J.H. Liu, J. Morales, B.P. Padley, R. Redjimi, J. Roberts, J. Zabel

University of Rochester, Rochester, USA

B. Betchart, A. Bodek, Y.S. Chung, R. Covarelli, P. de Barbaro, R. Demina, Y. Eshaq, H. Flacher, A. Garcia-Bellido, P. Goldenzweig, Y. Gotra, J. Han, A. Harel, D.C. Miner, D. Orbaker, G. Petrillo, D. Vishnevskiy, M. Zielinski

The Rockefeller University, New York, USA

A. Bhatti, L. Demortier, K. Goulianos, G. Lungu, C. Mesropian, M. Yan

Rutgers, the State University of New Jersey, Piscataway, USA

O. Atramentov, A. Barker, D. Duggan, Y. Gershtein, R. Gray, E. Halkiadakis, D. Hidas, D. Hits, A. Lath, S. Panwalkar, R. Patel, A. Richards, K. Rose, S. Schnetzer, S. Somalwar, R. Stone, S. Thomas

University of Tennessee, Knoxville, USA

G. Cerizza, M. Hollingsworth, S. Spanier, Z.C. Yang, A. York

Texas A&M University, College Station, USA

J. Asaadi, R. Eusebi, J. Gilmore, A. Gurrola, T. Kamon, V. Khotilovich, R. Montalvo, C.N. Nguyen, J. Pivarski, A. Safonov, S. Sengupta, A. Tatarinov, D. Toback, M. Weinberger

Texas Tech University, Lubbock, USA

N. Akchurin, C. Bardak, J. Damgov, C. Jeong, K. Kovitanggoon, S.W. Lee, P. Mane, Y. Roh, A. Sill, I. Volobouev, R. Wigmans, E. Yazgan

Vanderbilt University, Nashville, USA

E. Appelt, E. Brownson, D. Engh, C. Florez, W. Gabella, W. Johns, P. Kurt, C. Maguire, A. Melo, P. Sheldon, J. Velkovska

University of Virginia, Charlottesville, USA

M.W. Arenton, M. Balazs, S. Boutle, M. Buehler, S. Conetti, B. Cox, B. Francis, R. Hirosky, A. Ledovskoy, C. Lin, C. Neu, R. Yohay

Wayne State University, Detroit, USA

S. Gollapinni, R. Harr, P.E. Karchin, P. Lamichhane, M. Mattson, C. Milstène, A. Sakharov

University of Wisconsin, Madison, USA

M. Anderson, M. Bachtis, J.N. Bellinger, D. Carlsmith, S. Dasu, J. Efron, L. Gray, K.S. Grogg, M. Grothe, R. Hall-Wilton[1], M. Herndon, P. Klabbers, J. Klukas, A. Lanaro, C. Lazaridis, J. Leonard, D. Lomidze, R. Loveless, A. Mohapatra, D. Reeder, I. Ross, A. Savin, W.H. Smith, J. Swanson, M. Weinberg

†: Deceased

1: Also at CERN, European Organization for Nuclear Research, Geneva, Switzerland

2: Also at Universidade Federal do ABC, Santo Andre, Brazil

3: Also at Laboratoire Leprince-Ringuet, Ecole Polytechnique, IN2P3-CNRS, Palaiseau, France

4: Also at Suez Canal University, Suez, Egypt

5: Also at Fayoum University, El-Fayoum, Egypt

6: Also at Soltan Institute for Nuclear Studies, Warsaw, Poland

7: Also at Massachusetts Institute of Technology, Cambridge, USA

8: Also at Université de Haute-Alsace, Mulhouse, France

9: Also at Brandenburg University of Technology, Cottbus, Germany

10: Also at Moscow State University, Moscow, Russia

11: Also at Institute of Nuclear Research ATOMKI, Debrecen, Hungary

12: Also at Eötvös Loránd University, Budapest, Hungary

13: Also at Tata Institute of Fundamental Research - HECR, Mumbai, India

14: Also at University of Visva-Bharati, Santiniketan, India

15: Also at Facoltà Ingegneria Università di Roma "La Sapienza", Roma, Italy

16: Also at Università della Basilicata, Potenza, Italy

17: Also at Laboratori Nazionali di Legnaro dell' INFN, Legnaro, Italy

18: Also at California Institute of Technology, Pasadena, USA

19: Also at Faculty of Physics of University of Belgrade, Belgrade, Serbia

20: Also at University of California, Los Angeles, Los Angeles, USA

21: Also at University of Florida, Gainesville, USA

22: Also at Université de Genève, Geneva, Switzerland

23: Also at Scuola Normale e Sezione dell' INFN, Pisa, Italy

24: Also at INFN Sezione di Roma; Università di Roma "La Sapienza", Roma, Italy

25: Also at University of Athens, Athens, Greece

26: Also at The University of Kansas, Lawrence, USA

27: Also at Institute for Theoretical and Experimental Physics, Moscow, Russia

28: Also at Paul Scherrer Institut, Villigen, Switzerland

29: Also at University of Belgrade, Faculty of Physics and Vinca Institute of Nuclear Sciences, Belgrade, Serbia

30: Also at Adiyaman University, Adiyaman, Turkey

31: Also at Mersin University, Mersin, Turkey

32: Also at Izmir Institute of Technology, Izmir, Turkey

33: Also at Kafkas University, Kars, Turkey

34: Also at Suleyman Demirel University, Isparta, Turkey

35: Also at Ege University, Izmir, Turkey

36: Also at Rutherford Appleton Laboratory, Didcot, United Kingdom

37: Also at INFN Sezione di Perugia; Università di Perugia, Perugia, Italy

38: Also at KFKI Research Institute for Particle and Nuclear Physics, Budapest, Hungary

39: Also at Institute for Nuclear Research, Moscow, Russia

40: Also at Horia Hulubei National Institute of Physics and Nuclear Engineering (IFIN-HH), Bucharest, Romania

41: Also at Istanbul Technical University, Istanbul, Turkey

Bibliography

[1] D. Griffiths, *Introduction to Elementary Particles* (WILEY-VCH, Weinheim, Germany, 2004) Section 1.4.

[2] W. E. Burcham and M. Jobes, *Nuclear and Particle Physics* (Addison Wesley Longman Limited, Essex, GB, 1995) p. 637.

[3] E.D. Commins and P.H. Bucksbaum, *Weak interactions of leptons and quarks* (Cambridge University Press, NY, 1983).

[4] E.D. Commins and P.H. Bucksbaum, *Weak interactions of leptons and quarks* (Cambridge University Press, NY, 1983) Section 2.1.

[5] D. Griffiths, *Introduction to Elementary Particles* (WILEY-VCH, Weinheim, Germany, 2004) Section 1.8.

[6] T. Hansl-Kozanecka, *Experimental Tests of QCD: Deep inelastic scattering, e^+e^- annihilation and hard hadron-hadron scattering* (Lectures given at the SLAC Summer Institute, August 5-16, 1991, Standford, CA).

[7] M. Dardo, *Nobel Laureates and Twentieth-Century Physics* (Cambridge University Press, Cambridge, UK, 2004) p. 404.

[8] F. Wilczek, *Fantastic realities : 49 mind journeys and a trip to Stockholm* (World Scientific, Hackensack, N.J., 2006).

[9] R.N. Mohapatra, et al. , *Theory of Neutrinos: A White Paper* (arXiv:hep-ph/0510213).

[10] E.D. Commins and P.H. Bucksbaum, *Weak interactions of leptons and quarks* (Cambridge University Press, NY, 1983).

[11] W. E. Burcham and M. Jobes, *Nuclear and Particle Physics* (Addison Wesley Longman Limited, Essex, GB, 1995).

[12] W. E. Burcham and M. Jobes, *Nuclear and Particle Physics* (Addison Wesley Longman Limited, Essex, GB, 1995) p. 495.

[13] D. Griffiths, *Introduction to Elementary Particles* (WILEY-VCH, Weinheim, Germany, 2004) p. 321.

[14] S. L. Glashow, J. Iliopoulos, L. Maiani, *Weak Interactions with Lepton-Hadron Symmetry* (Physical Review D 2, 1970) p. 1285-1292

[15] B. Abbott et al. (DØ Collaboration), *Search for First-Generation Leptoquarks in the dielectron channel with the DØ Detector in $p\bar{p}$ Collisions at $\sqrt{s} = 1.96$ TeV* (arXiv:hep-ex/0907.1048v2, 2009).

[16] J. Pati and A. Salam, *Lepton Number as the Fourth Color* (Physical Review D 10, 1974) p. 275-289.

[17] A. Belyaev, et. al., *Leptoquark Single and Pair production at LHC with CalcHEP/CompHEP in the complete model* (Journal of High Energy Physics, JHEP09 005, 2005) p.11, Fig. 4.

[18] D. Acosta and S. Blessing, *Leptoquark searches at HERA and the Tevatron* (Annual Review of Nuclear and Paricle Science, 49, 1999) p. 399, Fig. 4.

[19] D. Acosta and S. Blessing, *Leptoquark searches at HERA and the Tevatron* (Annual Review of Nuclear and Paricle Science, 1999).

[20] M. Doncheski and S. Godfrey, *Leptoquark mass limits from single leptoquark production at LEP and LEP200* (Physics Letters B, Volume 393, Issues 3-4, 1997) p. 355-359.

[21] D. Acosta and S. Blessing, *Leptoquark searches at HERA and the Tevatron* (Annual Review of Nuclear and Paricle Science, 49, 1999) p. 405.

[22] B. Abbott et al. (DØ Collaboration), *Search for First-Generation Leptoquarks in the dielectron channel with the DØ Detector in $p\bar{p}$ Collisions at $\sqrt{s} = 1.96$ TeV* (arXiv:hep-ex/0907.1048v2, 2009) p. 3, Fig. 2.

[23] D. Acosta and S. Blessing, *Leptoquark searches at HERA and the Tevatron* (Annual Review of Nuclear and Paricle Science, 49, 1999) p. 418-419.

[24] R. Ley, A. DelRosso, B. Desforges, D. Manglonki, *CERN Accelerators* (CERN, May 2004).

[25] L. Evans and P. Bryant, *LHC Machine* (Journal of Instrumentation 3 S08001, 2008) Chapter 12.

[26] L. Evans and P. Bryant, *LHC Machine* (Journal of Instrumentation 3 S08001, 2008) Chapter 4.

[27] D. Barney and S. Cittolin, *CMS Detector* (CMS-doc-2716-v3, July 2010).

[28] The CMS Collaboration, *The CMS experiment at the CERN LHC* (Journal of Instrumentation 3 S08004, 2008) Chapter 3.

[29] The CMS Collaboration, *The CMS experiment at the CERN LHC* (Journal of Instrumentation 3 S08004, 2008) p. 30, Fig. 3.1.

[30] The CMS Collaboration, *The CMS experiment at the CERN LHC* (Journal of Instrumentation 3 S08004, 2008) Chapter 4.

[31] The CMS Collaboration, *The CMS experiment at the CERN LHC* (Journal of Instrumentation 3 S08004, 2008) p. 95, Fig. 4.5.

[32] The CMS Collaboration, *The CMS experiment at the CERN LHC* (Journal of Instrumentation 3 S08004, 2008) Chapter 5.

[33] The CMS Collaboration, *The CMS experiment at the CERN LHC* (Journal of Instrumentation 3 S08004, 2008) p. 127.

[34] The CMS Collaboration, *The CMS experiment at the CERN LHC* (Journal of Instrumentation 3 S08004, 2008) p.123, Fig. 5..

[35] The CMS Collaboration, *The CMS experiment at the CERN LHC* (Journal of Instrumentation 3 S08004, 2008) Chapter 7.

[36] The CMS Collaboration, *The CMS experiment at the CERN LHC* (Journal of Instrumentation 3 S08004, 2008) p. 169, Fig. 7.5.

[37] The CMS Collaboration, *The CMS experiment at the CERN LHC* (Journal of Instrumentation 3 S08004, 2008) p. 166, Fig. 7.3.

[38] The CMS Collaboration, *The CMS experiment at the CERN LHC* (Journal of Instrumentation 3 S08004, 2008) p. 198, Fig.. 7.47.

[39] The CMS Collaboration, *The CMS experiment at the CERN LHC* (Journal of Instrumentation 3 S08004, 2008) p. 200, Fig.. 7.51.

[40] The CMS Collaboration, *The CMS experiment at the CERN LHC* (Journal of Instrumentation 3 S08004, 2008) p. 218, Fig. 7.67.

[41] The CMS Collaboration, *The CMS experiment at the CERN LHC* (Journal of Instrumentation 3 S08004, 2008) Chapter 6.

[42] The CMS Collaboration, *The CMS experiment at the CERN LHC* (Journal of Instrumentation 3 S08004, 2008) p. 159, Fig. 6.4.

[43] The CMS Collaboration, *The CMS experiment at the CERN LHC* (Journal of Instrumentation 3 S08004, 2008) p. 158, Fig. 6.3.

[44] V. Kopenkin, Y. Fujimoto, and T. Sinzi, *Solution to the Centauro puzzle* (Physical Review D 68 052007, 2003)

[45] The CMS Collaboration, *The CMS experiment at the CERN LHC* (Journal of Instrumentation 3 S08004, 2008) Chapter 8.

[46] The CMS Collaboration, *The CMS experiment at the CERN LHC* (Journal of Instrumentation 3 S08004, 2008) p. 248, Fig. 8.1.

[47] T. Sjostrand, S. Mrenna, P. Skands, *Pythia 6.4 Physics and Manual* (hep-ph/0603175, March 2006).

[48] M. Mangano, et al., *ALPGEN, a generator for hard multiparton processes in hadronic collisions* (CERN-TH/2002-129, December 2006).

[49] F. Caravaglios, M. Moretti, *An algorithm to compute Born scattering amplitudes without Feynman graphs* (Phys. Lett. B358,1995) p. 332-338.

[50] F. Maltoni and T. Stelzer, *MadEvent: automatic event generation with MadGraph* (JHEP02 027, February 2003).

[51] J. Alwall, et al., *MadGraph/MadEvent v4: The new web generation* (JHEP 0709:028, 2007).

[52] S. Agostinelli et al., *GEAnt4 - a simulation toolki* (Niclear Instrument and Methods in Physics Research A 506, 250-303, March 2003).

[53] A. Naumann, et. al., *ROOT A C++ framework for petabyte data storage, statistical analysis and visualization* (Computer Physics Communications, Volume 180, Issue 12, December 2009, Pages 2499-2512).

[54] The CMS Collaboration, *Electron Reconstruction and Identification with first CMS 7 TeV data* (CMS PAS EGM-10/004, July, 2010).

[55] The CMS Collaboration, *Electron Reconstruction in CMS* (CMS NOTE 2006/40, February 2006) Section 3.

[56] The CMS Collaboration, *Electron Reconstruction in the CMS Electromagnetic Calorimeter* (CMS Note 2001/034, June 2001).

[57] The CMS Collaboration, *Electron Reconstruction in the CMS Electromagnetic Calorimeter* (CMS Note 2001/034, June 2001) p. 7, Fig.6.

[58] The CMS Collaboration, *Electron Reconstruction in the CMS Electromagnetic Calorimeter* (CMS Note 2001/034, June 2001) p. 3, Fig.1.

[59] The CMS Collaboration, *Electron Reconstruction in CMS* (CMS NOTE 2006/40, February 2006) Section 4.

[60] A. Goshtasby and W. O'Neili, *Curve Fitting y a Sum of Gaussians* (CVGIP: Graphical Models and Image Processing, Vol. 56, No. 4, July, 1994, pp. 281-288).

[61] The CMS Collaboration, *Electron Reconstruction in CMS* (CMS NOTE 2006/40, February 2006) Section 6.

[62] CMS Collaboration, *Electron reconstruction and identication at* $\sqrt{s}$*= 7 TeV* (CMS Detector Performence Summary DPS-2010-032, 2010).

[63] The CMS Collaboration, *Electromagnetic Calorimeter Commssioning and First Results with 7 TeV Data* (CMS PAS EGM-10-002, July, 2010) Section 4.2.

[64] M. Malberti, *APD Simulation vs Data* (ASC TF Meeting, June 2010) p. 12.

[65] The CMS Collaboration, *Performance of Jet Algorithms in CMS* (CMS PAS JME-07-003, March 2008) p. 2.

[66] M Cacchiari, G. Salam, and G. Soyez, *The anti-kt jet clustering algorithm* (Journal of High Energy Physics, Volume 2008, JHEP04(2008)063).

[67] The CMS Collaboration, *Plans for Jet Energy Corrections at CMS* (CMS PAS JME-07-002, July 2008).

[68] CMS Collaboration, *Jet Performance in pp Collisions at* $\sqrt{s}$*=7TeV* (CMS PAS JME-10-003, July 2010) Sec. 6.

[69] The CMS Collaboration, *Plans for Jet Energy Corrections at CMS* (CMS PAS JME-07-002, July 2008) p. 3, 5.

[70] The CMS Collaboration, *Identification and filtering of uncharacteristic noise in the CMS hadron calorimeter* (JINST 5 T03014, 2010).

[71] Cross section calculations from M. Kramer, private communications.

[72] The CMS Collaboration, *Tracking and Primary Vertex Results in First 7TeV Collisions* (CMS PAS TRK-10-005, July 2010) Sec. 2.

[73] The CMS Collaboration, *Search for High-Mass Resonances Decaying to Electron Pairs in the CMS Experiment* (CMS AN 2010-318, Nov. 2010).

[74] The CMS Collaboration, *Calorimeter Jet Quality Criteria for the First CMS Collision Data, and preparations for calibrating their efciencies* (CMS AN 2009/087, June 2009).

[75] CMS Collaboration, *Search for Pair Production of First Generation Scalar Leptoquarks at the CMS Experiment* (CMS AN 2008-070, Aug. 2009) Sec. 7.1.

[76] B. Abbott et al. (DØ Collaboration), *Limits on WWZ and WWγ Couplings from pp$\rightarrow$e+jj+X Events at $\sqrt{s}$ = 1.8 TeV* (Phys. Rev. Lett. 79, 1997) p. 14411446.

[77] B. Abbott et al. (DØ Collaboration), *Limits on WWγ and WWZ couplings from W boson pair production* (Phys. Rev. D 58, 051101(R), 1998)

[78] V. Brigljevic, et. al., *Study of di-boson production with the CMS detector at LHC* (Journal of Physics G: Nuclear and Particle Physics, 34, 2007) N269N295.

[79] The CMS Collaboration, *Measurement of CMS Luminosity* (CMS PAS EWK-10-004, June 2010).

[80] CMS Collaboration Collaboration, *Measurement of Inclusive W and Z Cross Sections in pp Collisions at $\sqrt(s)$ = 7 TeV* (CMS PAPER EWK-10-002, 2010) Sec. 5.1.

[81] The CMS Collaboration, *Search for High-Mass Resonances Decaying to Electron Pairs in the CMS Experiment* (CMS PAS EXO-10-012, Nov. 2010) Sec. 3.3.

[82] B. Abbott et al. (DØ Collaboration), *Search for First-Generation Leptoquarks in the dielectron channel with the DØ Detector in $p\bar{p}$ Collisions at $\sqrt{s}$ = 1.96 TeV* (arXiv:hep-ex/0907.1048v2, 2009) p. 8.

[83] Particle Data Group Collaboration, C. Amsler et al., *Review of particle physics, Section 32.3.1: The Bayesian approach* (Physics Letters, B667, 2008).

[84] The CMS Collaboration, *Search for Pair Production of Second Generation Scalar Leptoquarks in pp Collisions at* $\sqrt{s}$*=7TeV* (CMS PAS EXO-10-007, Oct. 2010).

[85] D. Acosta and S. Blessing, *Leptoquark searches at HERA and the Tevatron* (Annual Review of Nuclear and Paricle Science, 49:389-434, 1999) Section 5.1.5.